

UNIVERSITY OF SOUTHAMPTON

Faculty of Engineering, Science and Mathematics

School of Physics and Astronomy

**Surface effects and Director Profiles in Liquid
Crystal-Polymer structures with spatially
varying surface conditions**

By

Graham Gilchrist

Thesis for the degree of Doctor of Philosophy

School of Physics and Astronomy

July 2007

UNIVERSITY OF SOUTHAMPTON

ABSTRACT

FACULTY OF ENGINEERING, SCIENCE AND MATHEMATICS
SCHOOL OF PHYSICS AND ASTRONOMY

DOCTOR OF PHILOSOPHY

SURFACE EFFECTS AND DIRECTOR PROFILES IN LIQUID CRYSTAL-
POLYMER STRUCTURES WITH SPATIALLY VARYING SURFACE
CONDITIONS

By Graham Gilchrist

This thesis presents a study of the role of surface effects in the reorientation mechanism in a photorefractive-like liquid crystal-polymer hybrid structure. The photorefractive properties of liquid crystals were first discovered in 1994. Liquid crystals are very attractive as photorefractive materials due to their high nonlinear optical response caused by collective molecular reorientation, which can be induced by light and applied electric field. They are also low cost compared with photorefractive crystals. Liquid crystals are also excellent adaptive materials, ideal for writing dynamic re-writable gratings.

Photorefractive effects have been observed in both pure liquid crystals and polymers such as PVK, but also in certain hybrid structures of both liquid crystal and polymer layers. Recent experiments have shown that these effects are only apparent for certain combinations of liquid crystals and polymer surface layer, suggesting the cause to be surface-mediated at the interface between the two, and not due to bulk effects in the liquid crystal or the polymer. In this thesis I present characterisation and analysis of such hybrid structures and discuss a hypothesis for the underlying mechanism, supported by experimental and theoretical investigation.

When investigating surface effects, I also developed a system for characterisation of the molecular alignment in samples. This has been shown to be valid for molecular angles $0-16.3^\circ$ and $48.8-90^\circ$ from the surfaces. I also present an analysis of 'pretilt' measurement methods in which I have found the Crystal Rotation Method (CRM) to be most suited to our needs. I used this experimental method and the characterisation program to inspect cells that had been 'damaged' and exhibited long-term memory effects. I found that for some polymer-liquid crystal combinations, such as LC1294-PVK, the surface "damage" is due to applying electric field and light illumination.

A mathematical model for liquid crystal reorientation under a spatially varying field is presented. This model is based on the Landau De-Gennes theory and is used to simulate photorefractive gratings in liquid crystal cells with varying thickness and grating size. It has been found that the grating spacing to cell thickness ratio governs the penetration of electric field into the liquid crystal bulk. These simulations are useful for predicting the conditions for highest diffraction efficiency. Finally, the birefringence measurements I carried out were used to validate the theoretical simulations and to obtain simulation parameters for the experimental cells investigated

“One does not, by knowing all the physical laws as we know them today, immediately obtain an understanding of anything much.”

Richard Feynman (1918-1988)

List of Contents

Chapter 1 – Introduction	11
1.1 Motivations for this work.....	12
1.2 Overview of the work.....	13
Chapter 2 – Review of LC Optics	15
2.1 Introduction.....	15
2.2 History	16
2.3 Types of Liquid Crystal.....	18
2.4 Liquid Crystal Phases.....	19
2.5 Order Parameter and the Director	20
2.6 Orientation and Alignment	21
2.7 Deformations	24
2.8 Optical Properties of Liquid Crystals.....	25
2.9 Other Optical Effects.....	28
2.10 Liquid Crystals in Electric Fields.....	29
2.11 Liquid Crystal Applications.....	32
2.12 Sample Construction	33
Chapter 3 – Photorefractivity in Liquid Crystals	37
3.1 Mechanisms in Inorganic Photorefractive Materials	38
3.2 Beam Coupling	41
3.3 Photorefractivity in Liquid Crystals.....	43
3.4 Surface Induced Photorefractive-like Effect	45
3.5 Proposed Mechanism for the SIPRE.....	47
3.6 Summary.....	51
Chapter 4 – Uniform Director Measurements.....	53
4.1 Why Pretilt Angle?.....	54
4.2 Determining Uniform Director Orientation.....	55
4.3 Experimental Setup	56
4.4 Calculating the Angle of the Optic Axis	59
4.5 Differentiation Method.....	60
4.6 Analytical Representation	62

4.7 Multiple-Peak Method.....	68
4.8 Evaluating the Multiple Peak Method.....	70
4.9 Discussion and Analysis of Each Method.....	73
4.10 Experimental Results.....	75
4.11 Magnetic Null Experiments.....	80
4.12 Ageing and Damage Effects.....	83
4.13 Summary.....	86
Chapter 5 – Periodic Modulation of Director Profiles.....	87
5.1 Periodic Modulation of Director Profiles.....	87
5.2 Experimental transmission profiles.....	93
5.3 Other experimental approaches to mapping periodic director profiles.....	99
5.4 Director Profile Modelling.....	101
5.5 Simulating the Model.....	104
5.6 Input Parameters for the simulation.....	107
5.7 Simulation Results - Electric Field.....	111
5.8 Simulation Results – Director Fields and Refractive Index.....	112
5.9 Refining the simulation via birefringence experiments.....	120
5.10 Summary.....	125
Chapter 6 – Conclusions and Further Work.....	127
6.1 Future for the Project.....	128
Appendix A – IGOR Programs to Determine Pretilt Angle from CRM Data.....	130
Appendix B – Landau De-Gennes Model.....	140
B.1 Mathematical Model.....	140
B.1.1 The Tensor Order Parameter Model.....	140
B.1.2 Representation on the Basis of the Traceless 3×3 Symmetric Tensors ...	144
B.1.3 The Electrostatic Field Equation.....	146
B.1.4 The Scalar Limit.....	146
B.2 MATLAB Electric Field and Potential Calculations.....	148
References.....	150
List Of Publications.....	153
List of Presentations.....	153

List of Tables and Figures

Figure 2.1 – A common calamitic molecule.....	19
Figure 2.2 – How liquid crystal phases change with temperature.....	20
Figure 2.3 – The common components of a LC cell	22
Figure 2.4 – Creating alignment on the LC-glass interface.....	23
Figure 2.5 – Example cell configurations	24
Figure 2.6 – Deformations in liquid crystals.....	25
Figure 2.7 – Polarising microscope setup	27
Figure 2.8 – Off and On states of a twisted nematic display	33
Table 2.1 - Transition temperatures and physical properties of LCs in this study.....	34
Figure 2.9 – Mechanical rubbing machine used to induce surface alignment direction	35
Figure 2.10 - Vacuum chamber setup.....	36
Figure 3.1 – Phase shift between intensity pattern and index grating	40
Figure 3.2 - Image of two beams undergoing the two-beam coupling process in a liquid crystal cell. The beam on the left is being amplified at the expense of the other.	42
Figure 3.3 – Diagram of how the spatially varying intensity is formed in the cell with typical size parameters	43
Figure 3.4 – Charge recombination at the interface.....	49
Figure 3.5 – Tailored wavelength response.....	50
Figure 3.6 – Graph from reference [48]. Dependence of the phase shift on cell orientation.....	51
Figure 4.1 – Diagram of experiment to determine optical axis and pretilt.....	57
Figure 4.2 – Screenshot of pretilt experiment control software.....	58
Figure 4.3 - The relationship between ψ_x and α	60
Figure 4.4 - Dependence of pretilt angle α on angle of incidence ψ_x in the case of wavevector close to parallel to the optical axis	66
Figure 4.5 - Dependence of pretilt angle α on angle of incidence ψ_x in the case of wavevector close to perpendicular to the optical axis.....	67
Figure 4.6 - Dependence of the transmittance and retardation upon angle of incidence; ψ_x for high tilt angles where a symmetry point is not seen. [64].....	68

Figure 4.7 – Sample graph to evaluate the multiple peak method using data from reference [64]. The red line indicates the function in eq. 4.43, blue is the $y = 1$ line.	70
Figure 4.8 – Second sample graph to evaluate the multiple peak method using data from reference [64]. The red line indicates the function in equation 4.44.....	71
Figure 4.9 – Calculated transmission using equation 4.43 for $\alpha = 33.4^\circ$ (red line) from the paper and $\alpha = 37.6^\circ$ which is a much better fit to the experimental results (green line) in the paper. The transmission curves look very different.	72
Figure 4.10 – Experiment to remove pretilt measurement limit due to refraction.....	74
Figure 4.11 - Simulated Transmission curves for different thicknesses of cell.....	76
Figure 4.12 – Measured transmission function for the E7-PVK structure.....	77
Figure 4.13 - Measured transmission function for the E7-PI structure.....	77
Figure 4.14 - Measured transmission function for the LC1294-PVK structure.....	78
Figure 4.15 - Measured transmission function for the LC1294-PI structure.....	78
Figure 4.16 - Measured transmission function for the E7-homeotropic structure.....	79
Figure 4.17 - Measured transmission function for the E7- hybrid structure.....	79
Figure 4.18 – Experimental setup for magnetic null experiments.....	81
Figure 4.19 – Example magnetic null data sets showing the change in transmission variance with angle.....	83
Figure 4.20 – Polarising microscope image of a damage spot caused by a 5mW beam and 20V applied DC.....	84
Figure 4.21 – Transmission patterns from damaged areas. From this data it seems unlikely that there is a uniformly oriented structure in the damaged region.....	85
Table 5.1 – Refractive index and birefringence of LC1294.....	88
Table 5.2 – Refractive index and birefringence of E7 at 20°C . [65].....	89
Figure 5.1 – Experimental apparatus for gain vs. voltage experiments.....	89
Figure 5.2 - Gain ratio; G versus applied DC electric field for an E7-PVK: C_{60} cell.	90
Figure 5.3 - Gain ratio; G versus applied DC electric field for a LC1294-PVK: C_{60} cell.	91
Figure 5.4 – Experimental setup for observing grating formation.	93
Figure 5.5 – Reorientation grating viewed through a polarising microscope.....	94
Figure 5.6 - Polarising microscope image of a grating back-illuminated by a green LED and under applied voltage of 25V.....	95
Figure 5.7 – Polarising microscope images of steady state grating at different applied voltages.....	96

Figure 5.8 - Polarising microscope images of a grating under applied voltages.....	98
Figure 5.9 – Diagram of the axes used in modelling	102
Figure 5.10 – Screenshot of the main DMAP program interface showing the input parameters.....	105
Table 5.3 - Input Parameters for 5CB taken from [10, 13, 16]	107
Table 5.4 - Default Input Parameters.....	108
Figure 5.11 – Electric Field simulations as a function of grating period for 30 μ m thickness cells	111
Figure 5.12a – Electric field and director orientation for 30 μ m thick cells.....	114
Figure 5.12b – Electric field and director orientation for 30 μ m thick cells.....	115
Figure 5.13a – Refractive index surface plots of the cells in figure 5.3a for a 543.5nm probe beam with wavevector normal to the glass substrates.....	116
Figure 5.13b – Refractive index surface plots of the cells in figure 5.3b for a 543.5nm probe beam with wavevector normal to the glass substrates.....	117
Figure 5.14a – Cross sectional refractive index plots from figure 5.4a averaged through the thickness of the cell.	118
Figure 5.14b – Cross sectional refractive index plots from figure 5.4b averaged through the thickness of the cell.	119
Table 5.5 – Sample configurations for birefringence experiments	121
Figure 5.15 – Optical transmission data for three similar cells and equivalent calculated retardation.....	123

List of Accompanying Papers

- [1]. Andriy Dyadyusha, Malgosia Kaczmarek, **Graham Gilchrist**, *Surface screening layers and dynamics of energy transfer in photosensitive polymer-liquid crystal structures*, *Mol. Cryst. Liq. Cryst.*, **446** (2006), 261-272
- [2]. Dyadyusha, M. Kaczmarek, **G. Gilchrist**, G. D'Alessandro, *Proceedings of SPIE, Optics & Photonics*, 31 July - 4 August 2005, San Diego, California USA
- [3]. Dyadyusha, M. Kaczmarek, **G. Gilchrist**, G. D'Alessandro, J. Parka, R. Dabrowski, *Proceedings of SPIE*, **133** (2004), 5621

Declaration

I, Graham Gilchrist, declare that this thesis is the result of work done by myself, and generated by me as the result of my own research. I confirm that:

- this work was done wholly or mainly while in candidature for a research degree at this University;
- where any part of this thesis has previously been submitted for a degree or any other qualification at this University or any other institution, this has been clearly stated;
- where I have consulted the published work of others, this is always clearly attributed;
- where I have quoted from the work of others, the source is always given. With the exception of such quotations, this thesis is entirely my own work;
- I have acknowledged all main sources of help;
- where the thesis is based on work done by myself jointly with others, I have made clear exactly what was done by others and what I have contributed myself;
- parts of this work have been published as:
 - Andriy Dyadyusha, Malgosia Kaczmarek, Graham Gilchrist, *Surface screening layers and dynamics of energy transfer in photosensitive polymer-liquid crystal structures*, Mol. Cryst. Liq. Cryst., 446, pp 261-272, (2006)

Graham Gilchrist

26/06/07

Acknowledgements

I would like to thank several people without whom the finishing of this thesis would not have been possible. I would like to thank my supervisor Malgosia Kaczmarek, for her guidance and continued belief and support throughout the last 3 years and the writing of this thesis.

Also, I would like to thank Andriy Dyadyusha, whose experimental expertise was invaluable and who taught me many things, and without whom, I would have been lost.

I would also like to thank Giampaolo D'Alessandro for advice and cooperation on the mathematical and simulation parts of this work.

Finally, thanks goes to my family, without whose support I would never have gotten here. Thank you all.

Chapter 1 – Introduction

Liquid Crystals (LCs) have fascinated us for over 150 years since they were first observed in 1886. Their fascinating optical properties enthralled those early investigators and provide unique technological applications in the modern day. They also provide some wonderful examples of order and patterning in nature, and can be beautiful to look at. These days, the most obvious use of liquid crystals is in display technologies for computers, televisions and mobile phones. In fact, it is difficult to find any contemporary electronic device without a liquid crystal display.

Another equally useful application is in the fields of telecommunications and optical signal processing. Optical signals now underpin the majority of the world's communication, be it voice or data, and demand for faster and cheaper optical processing devices is high. Unfortunately, while liquid crystals have proved very successful in display applications, their use in other photonic or optoelectronic devices has been limited. Liquid crystals are attractive candidates for such photonics applications due to their high optical nonlinearity resulting from a large dielectric anisotropy and their thin film format. They also exhibit good optical quality, high strength, flexibility, high sensitivity to external applied fields and have an intrinsic adaptive nature because of their liquid-like states. There is considerable demand for such specifications for spatial light modulators.

One non-linear response is the photorefractive effect, first discovered for electro-optic crystals in 1966. The photorefractive effect is a light-induced change in the refractive index of a material when under spatially nonuniform illumination. The high dielectric anisotropy of liquid crystal molecules allows them to be reoriented under the application of small electric or optical fields, altering their optical properties. The photorefractive effect can facilitate asymmetric energy transfer (known as two beam coupling or TBC) between two writing optical beams. This effect is extremely valuable in potential photonics applications such as optical amplifiers and switches. Although the photorefractive effect is evident in pure liquid crystals and in pure photorefractive

polymers such as poly-N-vinylcarbazole (PVK), the orientational effect is enhanced in certain combined structures of the two under applied electric field. Such hybrid structures consist of a pure liquid crystal layer sandwiched between two polymer (usually PVK) coated ITO-glass layers. Experimental evidence implies that surface effects at the liquid crystal-polymer layer boundaries are highly significant to the reorientation process and investigating these will be the basis of this work.

1.1 Motivations for this work

In this thesis I present the results of a study on electric field induced molecular reorientation in liquid crystals combined with photosensitive polymer layers. In particular, the focus of this study was to build, characterise and model cells with different combinations of liquid crystals and photosensitive alignment layers that display the ‘photorefractive-like’ effect. An important part of this work was also to explain and model the effects of a varying surface electric field and the molecular mechanisms leading to the formation of an index grating.

Our cell design is closely related to those used in more conventional devices such as light-valves and modulators, but uniquely makes use of a photoconductive layer. Such devices are commonly used in security and sensing applications. Light valves, for example, generally have a light-sensitive writing side made of an inorganic photoconducting layer and a birefringent, phase modulating reading side. Our "optically addressed" PVK surfaces, doped with sensitiser, offer an alternative with superior performance and cheaper cost. Hence, these results could potentially have a large impact on the improved design and performance of light-valves and modulators.

One of the main problems facing the widespread adoption of LC use in photonics components is the requirement for both high and well-controlled optical and electro-optical response. To this end, I aimed to investigate a novel experimental liquid crystal with very high birefringence (LC 1294) and evaluate its suitability for enhanced electro-optic and photorefractive response.

Finally, recent proposals have been made for all-optical cross-connections for photonics devices using waveguides created at the interface between liquid crystals and polymers.

The interface between liquid crystals and photosensitive polymer surfaces such as the PVK surfaces used in our research, can serve as a waveguide for laser beams propagating along this boundary. Indeed, the surface and memory effects that were also studied here and will be presented in this thesis, have the possibility of being used to create light induced "paths" at the interface that can guide and couple light.

1.2 Overview of the work

This thesis is structured as follows; Chapter 2 covers general liquid crystal history and background and provides a sound theoretical basis for the experiments in the following chapters. I will discuss liquid crystal types, phases and transitions, interactions at surfaces and electric field response as well as common cells and how they are typically constructed.

Chapter 3 explains the theory behind traditional photorefractivity and the mechanisms involved as well as the proposed mechanisms behind the reorientation in liquid crystal-polymer structures. I will start with the discovery of the photorefractive effect in non-organic materials and then move on to photorefractive and photorefractive-like effects in liquid crystals.

Chapter 4 presents experiments on the characterisation of several liquid crystal-polymer cells and the methods used to determine pretilt angles and equilibrium director configurations for these cells. Several optical investigation methods are used to determine the director structures of uniaxial equivalent cells and some techniques are presented which may be transferable to cells with varying surface conditions. I also use these methods to look at time decay and optical damage to these cells.

Chapter 5 presents experimental results and theoretical modelling of the director structures in cells with periodically varying surface conditions. I present simulations performed using a mathematical model based on a Q tensor approach and compare these to transmission profiles measured in experiment. I also present the calibration of simulation parameters using simulated birefringence vs. voltage curves with experimental data.

Chapter 6 presents a summary of the results and the conclusions of this research and suggests some further avenues of interest and extension from this project.

Chapter 2 – Review of LC Optics

2.1 Introduction

Liquid crystals (LCs) are a class of materials which exhibit extra phases of matter between the conventional condensed matter solid and liquid phases. These additional *mesophases* arise from anisotropy in the shape or physical properties of their constituent molecules. Atoms in a crystalline solid have the highest positional order as they are fixed to their lattice sites whilst in a liquid the molecules have no positional order and are free to slide around and over each other as they please.

Liquid crystalline phases are generally defined as having:

- a) positional order in one or two dimensions, but not all three. i.e. The molecules have a degree in freedom in at least one axis

and/or

- b) orientational degrees of freedom due to anisotropy in molecular shape or properties.

A phase with zero positional order and no orientational order (for example by having isotropic molecules) is an isotropic liquid, and likewise a phase with fixed molecular positions and anisotropic molecules is an anisotropic crystalline solid. Liquid crystalline phases occur when there is a combination of a) and b) and there can be several distinct phases between the solid and isotropic liquid phases corresponding to different magnitudes of positional and orientational order. Liquid crystalline phases generally have less positional order than crystalline phases but retain more orientational order than liquids.

In this chapter I will review the basics of liquid crystals, including the types of liquid crystal materials, liquid crystal phases and alignment. I will also cover electrical and optical field interactions which are critical to the operation of modern LC devices. I will

also show typical LC cell construction techniques and types of cells which will be used in this project.

2.2 History

The history of liquid crystal science dates back further than a century, yet most of the knowledge critical for modern devices has only been discovered in the last 40 years. I present here a short summary of the most influential discoveries and papers of liquid crystal history, leading up to display and other optical applications.

In the period of 1850 to 1888 several scientists [1][2][3] reported observing strange colour effects near the melting temperatures of certain biological materials such as stearin or cholesterol. In 1888 Friedrich Reinitzer, a biologist, was studying cholesterol benzoate and cholesterol-acetate when he observed the same features [4]. More significantly, he also observed that these materials would melt from solid to a cloudy liquid with increasing temperature, before then turning to a clear liquid. Reinitzer consulted Otto Lehmann, the inventor of the heating stage polarising microscope, with the hopes of identifying exactly what was going on. Together, they proposed a new type of flowing crystal which they dubbed the ‘Liquid Crystal’ phase [5]. Initially this idea was dismissed by many scientists, most of whom thought the materials were mixtures of some sort, and that the multiple melting points were due to separate transitions for each component. These were eventually silenced in the light of meticulous experiments with pure chemicals. The first synthesised liquid crystal; p-azoxyanisole, was produced in 1890 by Gatterman and Ritschke [6] who also observed the second cloudy phase in their material.

In 1922 Georges Friedel introduced the LC classification scheme which we use today [7]. His extensive review on the subject collected all observations and knowledge up until that point and remained a seminal reference work until the fifties. He identified the separate molecular orderings and named the nematic, smectic and cholesteric phases. It was Friedel who first proposed a completely new phase of matter and coined the *mesomorphic* term. Shortly afterwards in the soviet union, Vsevolod Konstantinovich Fredericksz discovered the *Fredericksz transition*, the threshold electric field required

to induce reorientation of liquid crystal molecules, and the principle which underpins all modern LCDs.

Three important theoretical descriptions of liquid crystals arose after 1930. Firstly, the continuum theory developed by F.C. Frank [8] based upon elastic property work by Carl Oseen in Sweden [9] in which he proposed the ‘Frank’ elastic constants. Secondly the Maier-Saupe theory developed by Alfred Saupe and Wilhelm Maier [10] on the molecular theory of liquid crystals without dipoles. Thirdly, and only completed much later in 1971, was the intermediate theory proposed by Pierre Gilles De-Gennes [11], building on earlier work by Lev Landau in 1937 on phase transitions. The ‘Landau De-Gennes’ theory as it came to be known was pretty revolutionary, and was able to describe optical properties such as birefringence as well as phase transitions.

During the second world war era very little research was carried out, due to both the restricted communications and resources, and that most in the field believed everything useful about LCs had already been discovered. In 1957, an article by Glenn Brown [12] [11] created a resurgence of interest in the field. In 1963, with the development of transparent Indium Tin Oxide for electrodes, the first instance of an LCD was born out of the experiments of Richard Williams at the Radio Corporation of America (RCA) [13].

This would be the forerunner to a modern resurgence in liquid crystal optical applications and led to the development of dynamic scattering and guest-host displays. A significant development was the synthesis of MBBA; a liquid crystal which was in the nematic phase at room temperature [14]. The final development in basic LCDs was the construction of the twisted nematic (TN) display, still used today [15]. Since that first display, technological advancement has come on leaps and bounds, especially with the mass adoption of LCDs for laptops and computer monitors in the early 2000’s. Many advances in power consumption, driving voltage and viewing angle have all developed, yet the basic principles of TN displays remain the same.

Today we are all using low cost, large size liquid crystal displays and development continues on faster switching and better viewing angles. Much of the optical research

done for displays can be utilised in other applications such as light processing for holography or telecoms. Liquid crystals have a lot of life in them yet.

2.3 Types of Liquid Crystal

As I have already stated liquid crystals exhibit additional mesophases of matter between the traditional crystalline and liquid states. These states arise from anisotropy in the molecular structure or properties, which means that the liquid crystal phases have varying degrees of positional and orientational order. Liquid crystals can be broadly classified into two types:

- i. *Thermotropic* liquid crystals were the first to be recognised as such, and are so named because their phase transitions (and therefore molecular ordering) are a function of temperature. The anisotropy in thermotropic LCs arises from the molecular shape.
- ii. *Lyotropic* liquid crystals have phase transitions which are dependant on both temperature and solution concentration. Although discovered much earlier than thermotropics, their recognition as liquid crystals did not come until much later. Anisotropy in lyotropics arises from molecules with hydrophobic head groups and hydrophilic tails, both which interact differently with the solvent.

In this study I will be concentrating on thermotropic liquid crystal-polymer cells. In a thermotropic system, above the crystalline melting temperature T_m , the system becomes more disordered. This means the molecules become more loosely packed and fluctuate further from the average molecular direction. Above the clearing point temperature T_c , the liquid crystal phase turns to liquid and the material becomes an isotropic liquid.

There are two anisotropic shapes of molecule which can exhibit liquid crystalline phases. Thermotropic liquid crystals can be further sub-classified into types depending on these shapes.

- i. *Calamitic* liquid crystals. One of the most common shapes to form LC phases is the rod-shaped molecule. Here, one molecular axis is much longer than the other two which provides anisotropy. The rod shapes must generally be fairly rigid to

maintain the anisotropy and can form many phases including nematics and smectics. Some of the most common calamitic materials are composed of benzene rings connected by rigid bonds and with hydrocarbon chains on either end. The experiments in this work are all conducted on calamitic liquid crystals and it should be assumed any discussion refers to these unless otherwise noted.

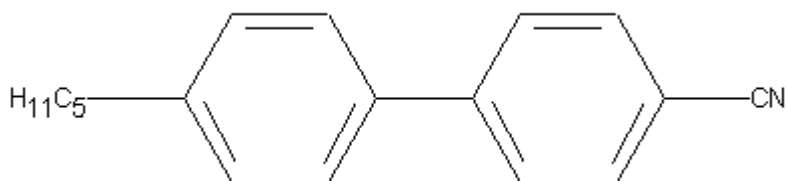


Figure 2.1 – A common calamitic molecule. The chemical known as 5CB (4-cyano-4'pentylbiphenyl)

- ii. *Discotic* liquid crystals have molecular structures resembling discs and are much shorter in one axis, providing the anisotropy. Discotic molecules can form discotic nematic phases, as well as unique columnar and hexagonal columnar phases where the molecules stack on top of each other.

2.4 Liquid Crystal Phases

A liquid crystal can have one or more liquid crystal phases differentiated by their degree of positional and orientational order. There are many possible phases of molecular arrangement which can be formed by thermotropic molecules, but they will not all be present in each material. The possible phases are determined by the molecular shape and properties. The two most important phases for calamitic LCs are the nematic and smectic phases.

The nematic phase is the one in which all experiments in this investigation will be conducted. It is the most basic of liquid crystal phases and in it, molecules have no positional order but maintain orientational order. As such, it is a level above an isotropic liquid in terms of order but less ordered than the smectic phases. In a nematic, the local ordering of the molecules is in the same general direction and (with appropriate boundary conditions) can be assumed to be homogeneous throughout the sample such

that the optical properties resemble a uniaxial crystal.

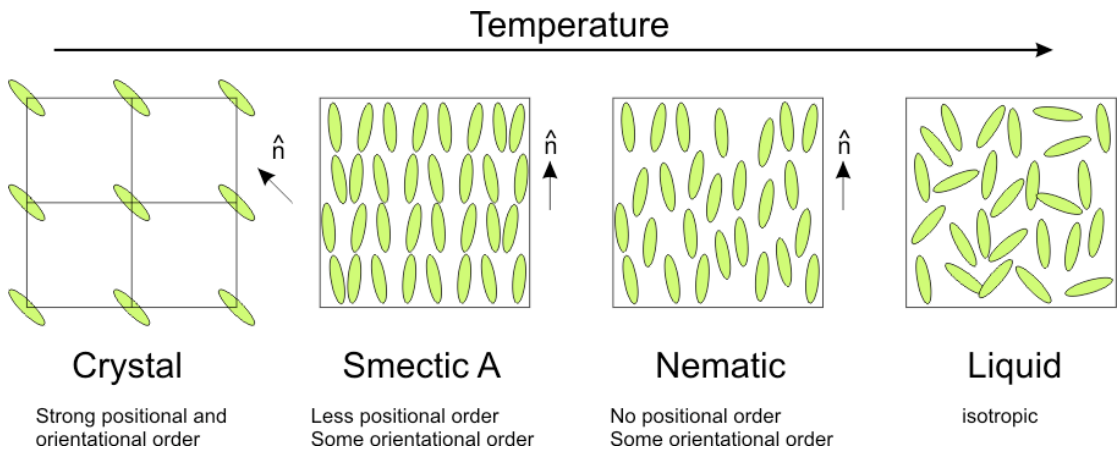


Figure 2.2 – How liquid crystal phases change with temperature

Smectic phases (from the Greek for soap - which is also a liquid crystal) are more ordered than nematics. Typically they have an orientational order as well as a one or two dimensional positional order. There are currently twelve types of smectic phase which can form in LCs, and these are labelled alphabetically in the order (generally) in which they were discovered.

Regular nematics tend to like to align mostly in the same direction as this minimises the energy interactions between them, but for a certain class of *chiral* materials, the minimum energy configuration is with each molecule slightly at an angle to its neighbours. The result is that the orientation of the molecules rotates like a helix throughout the LC forming a chiral nematic phase.

2.5 Order Parameter and the Director

Rather than talking vaguely about order, it is useful to define a quantitative mathematical value known as the *order parameter*. To do this I need to introduce the concept of the *director*. The director describes the positional orientation of molecules in a liquid crystal cell and is usually denoted by the unit vector \hat{n} . On a microscopic level it corresponds to the direction of the long axis of a calamitic molecule, but on a macroscopic scale it is used to describe the average molecular direction of a sample.

In a nematic, the molecules generally point along the director, but due to thermal effects, fluctuate about this direction. As a nematic phase is heated and becomes more disordered, the molecules gain more energy and tend to fluctuate in orientation more. Thus whilst the average direction will remain the same, the individual molecules will fluctuate further from the director with increasing temperature. In other types of phases such as chiral nematics, the director rotates as it moves through the sample, following the average molecular orientation of the chiral molecules.

There are multiple theoretical descriptions for order parameters, but one of the most common and useful starting points is the nematic order parameter S . This is expressed as the average deviation from the director using the second Legendre polynomial [16]:

$$S = \langle P_2 \cos \theta \rangle = \frac{1}{2} \langle 3 \cos^2 \theta - 1 \rangle \quad (2.1)$$

where θ is the angle between a single molecular axis direction and \hat{n} . Equation 2.1 thus describes an average deviation of many molecules from the director and is useful as a measure of order in the system. For $\theta = 0$ there is no deviation and $S = 1$ as in a crystal. For a completely unordered (isotropic) system $S = 0$. In a typical thermotropic liquid crystal phase, S varies from approximately 0.3-0.8, decreasing with temperature. The order parameter can be measured experimentally using birefringence, nuclear magnetic resonance or Raman scattering experiments.

2.6 Orientation and Alignment

Given the fact that they are able to flow, LCs must be confined within some restricted space to be useful. Experimentally and in devices such as displays, liquid crystals are commonly confined between two glass plates to form a liquid crystal cell, an example of which is shown in figure 2.3. Usually the glass plates are coated with transparent electrodes such as Indium Tin Oxide (ITO) as this enables the electrical manipulation of the cell without altering its optical properties.

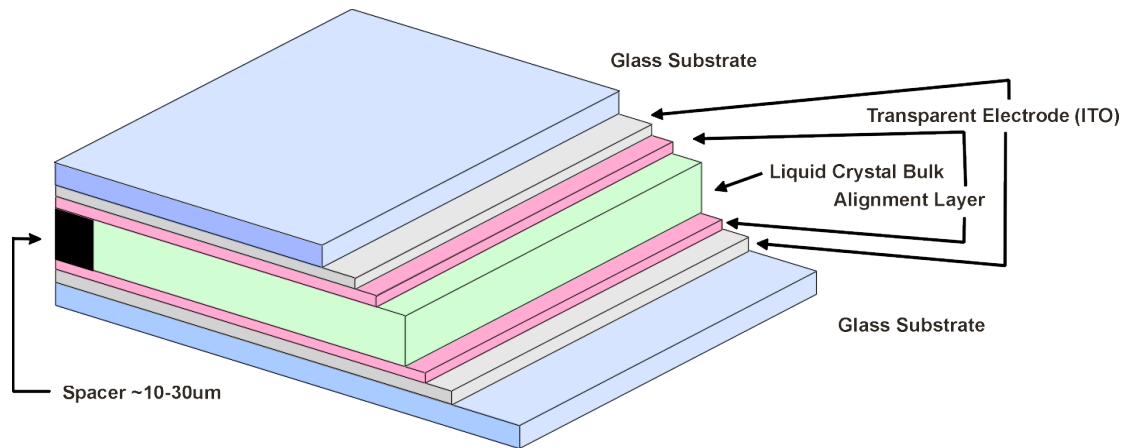


Figure 2.3 – The common components of a LC cell

It has already been mentioned that LC molecules will try to align to minimise the energy interactions between them, but what has not been considered is what happens when boundary conditions are imposed on the system. Placing the LC material between glass plates imposes boundary conditions on the molecules touching the plates and depending on the alignment of these molecules, the others in the LC will align according to the minimum energy configuration.

For this reason, adding an alignment layer on top of the ITO is usually necessary to avoid random surface alignment and a resulting cell with many small domains in which the molecules point in different directions. Common alignment layers are either polymers, treated by mechanical rubbing to induce a certain orientation on the surface LC molecules, or metallic films deposited at an oblique angle to create a surface topology which encourages a certain alignment.

Prior treatment of the glass surfaces with surfactants and/or rubbing the substrate polymers in a specific direction causes the liquid crystal molecules at the surface to take on a preferred minimum energy orientation known as the easy axis. The surface *anchoring* is said to be strong if it is sufficient to overcome the elastic forces within the liquid crystal and induce long range ordering across the entire liquid crystal bulk. In this case it can be assumed the boundary molecules are fixed in their orientation. Weak anchoring occurs when the surface treatment induces shorter range ordering which may vary far from the surfaces. In this case, the orientation of the boundary molecules may

be modified by bulk elastic deformations or applied electric fields. Mechanical rubbing does not always provide strong anchoring at the surfaces.



Figure 2.4 – Creating alignment on the LC-glass interface. a) Treatment with amphiphilic molecules b) Oblique evaporation of metal film c) Rubbed grooves in polymer

The resulting director distribution through the cell is found by minimising the free energy of the system and is a balance between the boundary conditions imposed by the anchoring energy at the substrates and the elastic forces intrinsic to the liquid crystal. With a suitable choice of surface treatments desired arrangements of molecules can be created.

Examples of typical cell configurations are shown in figure 2.5. The simplest case is to consider a nematic cell in which the average molecular direction is given by the director. A substrate covered with a film of amphiphilic molecules will align neighbouring liquid crystal molecules perpendicular to the substrate. Treating both surfaces this way creates a homeotropic cell with the director perpendicular to the substrates (fig 2.5b). Coating with a thin layer of polymer such as poly-N-vinylcarbazole (PVK) and mechanically rubbing in a particular direction induces an easy axis parallel to the substrate plane. When both substrates are treated this way there is a planar (or homogeneous) cell with director parallel to the substrates (fig 2.5a).

The most common configuration however is that of the tilted cell. This is a homeotropic or planar cell where elastic forces or surface interactions cause the molecules at the surface to be tilted at some angle α from perfect parallel or perpendicular configurations. Mechanically rubbing the alignment polymer polyimide (PI) for instance, creates a molecular tilt at $\approx 3^\circ$ from the planar configuration. Two anti-parallel

rubbed substrates create a tilted cell with director at some pretilt angle α from the substrates (fig 2.5d).

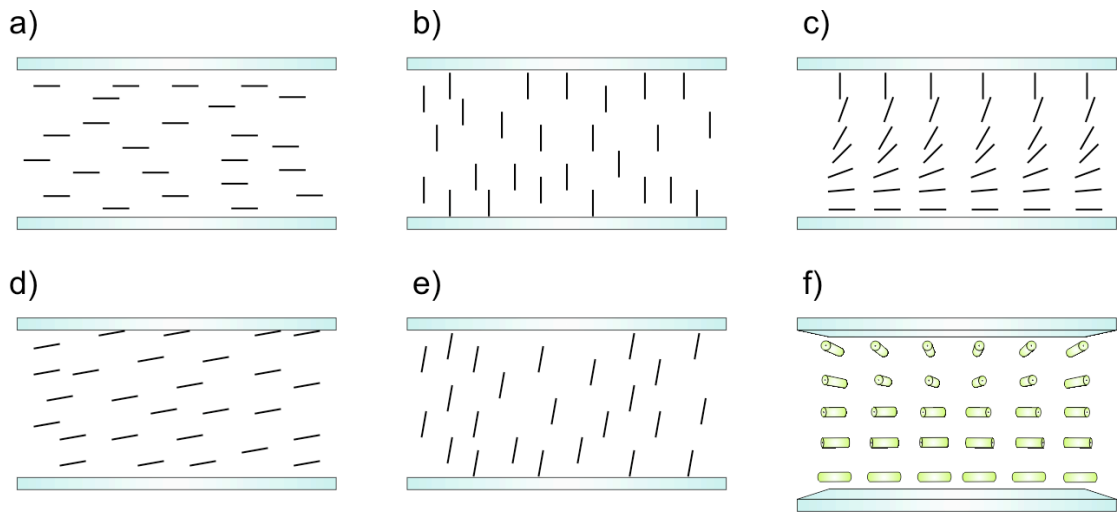


Figure 2.5 – Example cell configurations. a) Planar b) Homeotropic c) Pi (hybrid) cell d) Tilted planar e) Tilted homeotropic f) Twisted nematic

Other cell configurations can be created by combining different treatments on each substrate. A twisted nematic (TN) cell is given planar alignment on each substrate but the rubbing directions are oriented perpendicularly to each other, creating a twist in director through the cell (fig 2.5f). Similarly, one substrate may be given planar alignment and the other homeotropic, resulting in a Pi (also known as a bend or hybrid) cell where the tilt angle from the substrate varies from $0-90^\circ$ from one substrate to the other (fig 2.5c).

2.7 Deformations

It has been seen that the director can be made to vary in a cell due to surface treatment. In fact there are three types of distortions which a LC can undergo. These are known as splay, twist and bend after what happens to the shape of the director.

Frank’s continuum theory expression for the free energy of a LC system, provides a good mathematical description for these effects. Frank’s ‘free energy per-unit volume’ for a nematic is written [17]:

$$F_v = \frac{1}{2}K_1[\nabla \cdot \hat{n}]^2 + \frac{1}{2}K_2[\hat{n} \cdot (\nabla \times \hat{n})]^2 + \frac{1}{2}K_3[\hat{n} \times (\nabla \times \hat{n})]^2 \quad (2.2)$$

where K_1 , K_2 and K_3 are the Frank elastic constants which describe how ‘stiff’ the liquid crystal is in response to Splay, Twist and Bend deformations respectively. Typical values for these constants are of the order of 10^{-11} N and K_3 is usually larger than K_1 and K_2 .

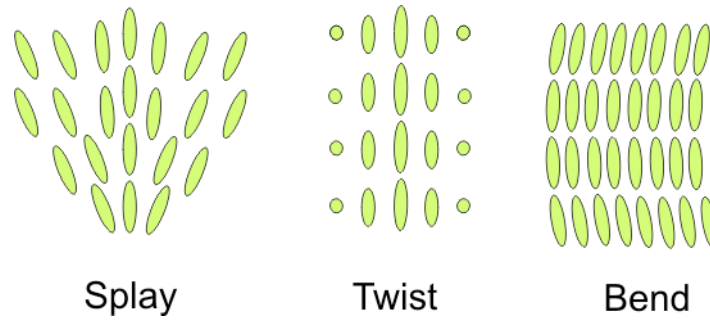


Figure 2.6 – Deformations in liquid crystals

2.8 Optical Properties of Liquid Crystals

Liquid crystals also have some very interesting optical responses which are responsible for their high demand for display applications. When a light wave encounters a boundary between two materials (of differing refractive index) some of it is reflected and some is refracted. The refractive index of a material is a measure of the speed of light propagation in said material. At optical frequencies, liquid crystals are non-magnetic, so that the refractive index is the square root of the dielectric constant (relative permittivity) of the material:

$$n = \sqrt{\varepsilon} = \sqrt{\frac{\bar{\varepsilon}}{\varepsilon_0}} \quad (2.3)$$

where n is the refractive index of the material, ε is the relative permittivity which is the permittivity $\bar{\varepsilon}$ expressed in units the permittivity of free space; ε_0 . In liquid crystals, the anisotropy of the system means that the relative permittivity varies depending on the

direction of the interacting electric field. In turn, this anisotropy in permittivity also results in anisotropy in the refractive indices. The material is said to be birefringent and in a nematic two different refractive indices are defined; n_{\parallel} (n_e) and n_{\perp} (n_o) which are encountered for light polarised parallel and perpendicular to the director (long molecular axes in this case) respectively. The difference in refractive indices:

$$\Delta n = n_{\parallel} - n_{\perp} \quad (2.4)$$

is known as the *birefringence* or optical anisotropy and generally decreases with increasing temperature as the order parameter decreases. These refractive index components are again the square root of the corresponding relative permittivity components.

A nematic with uniform director alignment can thus be considered a uniaxial crystal whose optic axis is parallel to the long axis of the molecules. In a uniaxial material, the refractive index for light along the one different axis is defined as being the extraordinary refractive index; n_e , and light along the other two axes defined as the ordinary refractive index; n_o (so $n_e \equiv n_{\parallel}$, $n_o \equiv n_{\perp}$ for rod-like molecules). Uniaxial crystals are also sub-categorized as positive-uniaxial or negative-uniaxial depending on the sign of the optical anisotropy $n_e - n_o$. These features are important for crystallography-like experiments as performed in chapter 4.

Birefringent materials can be either uniaxial or biaxial. A uniaxial crystal has two different refractive indices and discotic and calamitic nematic phases fall under this category. Biaxial materials have 3 separate refractive indices corresponding to each 3-dimensional axis. In the research presented here I will only be dealing with uniaxial nematic materials.

Birefringence gives rise to another important effect. If a wave with electric field components pointing along the different refractive indices enters a birefringent crystal, those components will travel at different speeds and become out of phase. This effect is known as *retardation*. One can choose the liquid crystal thickness such that the waves leave the crystal π or $\pi/2$ out of phase, thus creating half-wave or quarter-wave plates.

Retardation can be measured by placing the LC between crossed polarising plates oriented at 45 degrees to the director. This is how a polarising microscope works, taking advantage of optical retardation to identify different domains and defects in a particular sample as shown in figure 2.7.

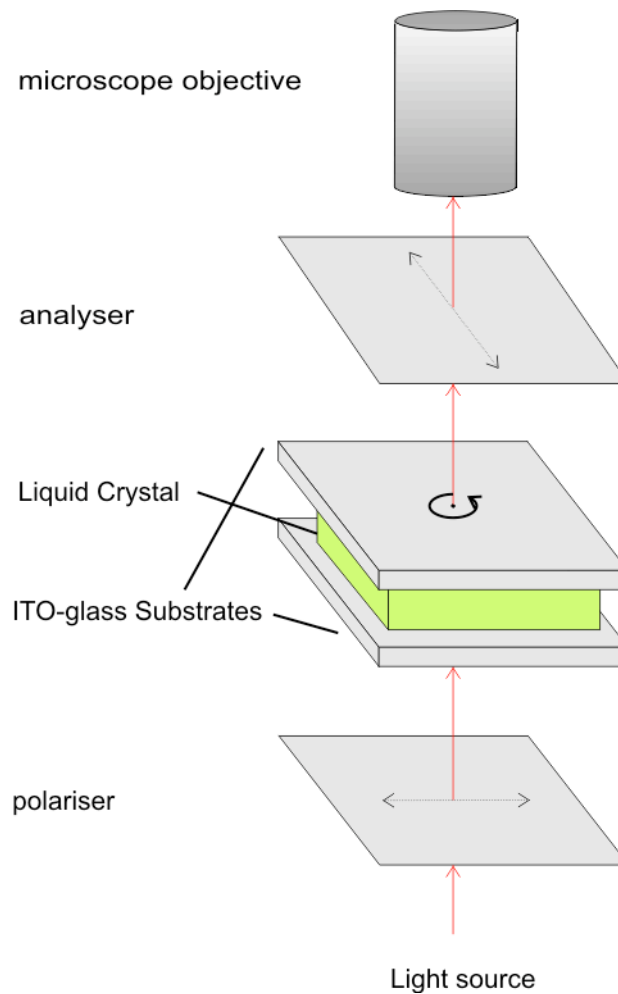


Figure 2.7 – Polarising microscope setup

Liquid crystals are also highly nonlinear. Several nonlinear optical effects have been observed in liquid crystals whereby the liquid crystal properties change under illumination. Some of these effects are wave mixing, harmonic generation, self-focussing and self phase modulation.

Of most interest however, are the variety of *photorefractive* effects in which a refractive index change occurs under illumination of light. Since liquid crystal molecules have degrees of freedom, the optical fields tend to act to move or reorient the molecules,

creating a refractive index change. Photorefractive effects in liquid crystals can occur via many processes depending on the substance but all exhibit an extremely high nonlinear response due to the collective reorientation of molecules within the LC. The photorefractive effect is explained in more detail in the next chapter and will be important for the work presented in chapter 5.

2.9 Other Optical Effects

Chiral liquid crystals also exhibit some interesting optical effects. In a chiral crystal, the director varies as the wave propagates through the medium, meaning that on average, both perpendicular components of an linearly polarised e-field will see the same phase delay. Such materials have no linear birefringence but do exhibit birefringence for circularly polarised light. In a chiral material, left-handed and right handed circularly polarised light travel at different velocities creating circularly polarised birefringence and an anisotropy given by $n_R - n_L$. At the output of the LC, the two waves are out of phase. If the left and right input polarisations are equal in magnitude (effectively linearly polarised light) then the output is also linearly polarised but rotated by some angle relative to the input polarisation. This phenomenon is known as optical activity.

A special case appears when the helical pitch of a chiral nematic is much longer than the wavelength of the interacting light. In this case, the director changes very little over many wavelengths and the wave can be thought of as seeing a series of nematic slices with successive small director rotations. At each 'interface' between slices the electric field will have new components parallel and perpendicular to the director which propagate at different velocities. This can be thought of as elliptically polarised light emerging from each slice with its semi-major axis along the director of the next slice. Thinking of the chiral nematic as a series of infinitesimally small slices, the phase delay from one slice is so small there is negligible birefringence and its output is effectively linearly polarised along the direction of the next slice's director. As the wave progresses through the slices the linear polarisation is rotated with the director in a process known as *waveguiding*.

On the other hand, if the wavelength of the incident light is of the same order as the helical pitch and incident at a specific angle, selective reflection can be seen. This is a

constructive interference effect whereby light incident at a specific angle is reflected from the repeating ‘layers’ of a chiral helix such that successive layers of reflections constructively combine at only one wavelength. This is one of the more beautiful features of observing a chiral liquid crystal, since the reflected colour changes as it is rotated.

2.10 Liquid Crystals in Electric Fields

The strong dielectric anisotropy of liquid crystals allows the director to be manipulated via the application of an electric field. The total permittivity in liquid crystals is a result of two different effects. The first is the induced temporary dipole moment produced by an applied field on the LC molecules. Under the application of electric field, there is a dipole moment per unit volume (denoted by the polarization \vec{P}) on the liquid crystal given by [16]:

$$\vec{P} = \epsilon_0 \bar{\chi}_e \vec{E} \quad (2.5)$$

where \vec{E} is the electric field, ϵ_0 is the permittivity of free space and χ_e is the electric susceptibility tensor such that:

$$\begin{pmatrix} P_x \\ P_y \\ P_z \end{pmatrix} = \begin{pmatrix} \chi_{e\perp} & 0 & 0 \\ 0 & \chi_{e\perp} & 0 \\ 0 & 0 & \chi_{e\parallel} \end{pmatrix} \begin{pmatrix} E_x \\ E_y \\ E_z \end{pmatrix} \quad (2.6)$$

The electric displacement is given by:

$$\vec{D} = \epsilon_0 \vec{E} + \vec{P} = \bar{\epsilon} \vec{E} \quad (2.7)$$

where $\bar{\epsilon} = \epsilon_0 (\bar{1} + \bar{\chi}_e)$ and $\bar{1}$ is the unit tensor:

$$\bar{\mathbf{1}} = \begin{pmatrix} 1 & 0 & 0 \\ 0 & 1 & 0 \\ 0 & 0 & 1 \end{pmatrix} \quad (2.8)$$

$\bar{\epsilon}/\epsilon_0$ is the dimensionless relative permittivity (dielectric constant). The second contribution to the permittivity arises from the orientation of permanent dipole moments on the molecules by the electric field. This effect can be very large for liquid crystals. Although they have permanent dipole moments, nematic molecules are generally not sensitive to the sign of the applied electric field as the orientation contribution from permanent dipoles is small compared to other contributions. The permittivity anisotropy is:

$$\Delta\epsilon = \epsilon_{\parallel} - \epsilon_{\perp} \quad (2.9)$$

where ϵ_{\parallel} and ϵ_{\perp} are the permittivity components parallel and perpendicular to the director respectively. If ϵ_{\parallel} is larger (positive liquid crystal) then the molecules tend to align along the electric field but if ϵ_{\perp} is larger they tend to align perpendicularly to the field. In liquid crystals this orientational contribution to the permittivity usually dominates and thus $\Delta\epsilon$ is linked to the order parameter and its dependence on temperature. As temperature is increased, $\Delta\epsilon$ usually decreases and becomes zero at the clearing point temperature. In other cases the induced polarisation can almost cancel the orientational polarisation and a much more complicated temperature dependence is seen. Clearly then, under the application of an electric field the free energy minimum of the director configuration must now take into account the electric field contribution and a new equilibrium reached. If the polarisation is expressed in terms of the susceptibility components parallel and perpendicular to the director, then:

$$E_{\parallel} = \bar{\mathbf{E}} \cdot \hat{\mathbf{n}} \quad (2.10)$$

$$E_{\perp} = \left| \bar{\mathbf{E}} - (\hat{\mathbf{n}} \cdot \bar{\mathbf{E}}) \hat{\mathbf{n}} \right| \quad (2.11)$$

The polarisation components then become:

$$P_{\parallel} = \varepsilon_0 \chi_{e\parallel} (\vec{E} \cdot \hat{n}) \quad (2.12)$$

$$P_{\perp} = \varepsilon_0 \chi_{e\perp} \left| \vec{E} - (\hat{n} \cdot \vec{E}) \hat{n} \right| \quad (2.13)$$

such that the total polarisation is:

$$\vec{P} = \varepsilon_0 \left[\chi_{e\perp} \vec{E} + \Delta\chi_e (\hat{n} \cdot \vec{E}) \hat{n} \right] \quad (2.14)$$

where $\Delta\chi_e = \chi_{e\parallel} - \chi_{e\perp}$. The change in free energy (electric energy) density per unit volume is then:

$$dU_e = -\varepsilon_0 \Delta\chi_e (\vec{E} \cdot \hat{n}) (\vec{E} \cdot d\hat{n}) \quad (2.15)$$

and the free energy becomes:

$$U_e = -\frac{1}{2} \varepsilon_0 \Delta\chi_e (\hat{n} \cdot \vec{E})^2 \quad (2.16)$$

$$= -\frac{1}{2} \varepsilon_0 \Delta\chi_e E^2 \sin^2 \theta \quad (2.17)$$

where θ is the angle between the director \hat{n} and the substrate plane. The director configuration will orient itself to minimize this equation. The electric field must however overcome the anchoring energy and elastic forces within the liquid crystal which act to maintain the configuration imposed by the boundary conditions. Reorientation of the director under applied field therefore only occurs when the field is above a certain threshold known as the *Freedericksz* threshold. The transition between director configurations is known as the Freedericksz transition and may also occur under an optical field in which case it is known as the optical Freedericksz transition. Above the transition field value the reorientation is nonlinear with field strength. The threshold electric field required for reorientation is related by the formula [16]:

$$E_t = \frac{\pi}{d} \sqrt{\frac{K}{\varepsilon_0 \Delta\chi_e}} \quad (2.18)$$

where d is the thickness of the liquid crystal layer, $\Delta\chi$ is the susceptibility anisotropy and K is average of the three Frank elastic constants for distortions. If the director is tilted at the boundaries then reorientation becomes slightly easier and for certain tilt angles there is gradual director reorientation with increasing electric field strength and a threshold effect is not seen. It is the features of this reorientation which make liquid crystals attractive for optics applications.

2.11 Liquid Crystal Applications

A number of display types based on liquid crystal technology have been developed so far. The most simple type of LCD is one in which a liquid crystal cell is placed between two crossed polarising plates. This is known as a *twisted nematic* display and is shown in figure 2.8. The cell is constructed as a twist cell such that the molecules are in planar alignment on each surface but twist through 90 degrees so that they are orthogonal at each surface. Each surface also has transparent electrodes allowing an electrical field to be applied. When there is no applied field, the cell appears transparent as the twist rotates the input polarisations to the same state as the output polariser allowing the wave to pass. Once a field (above the Freedericksz transition) is applied, the molecules reorient themselves along the field and no polarisation rotation is performed on waves travelling through the cell and it appears black due to the crossed polarisers. Other types of LCD include, the super twist nematic, the polymer-dispersed liquid crystal (PDLC) and the dynamic scattering display [18].

In a large computer display or television, many of these cells are arranged in an addressable matrix, with separate cells for the transmission of red, green and blue light, allowing the display to mix these into other colours.

Other applications are in telecommunications where electro-optic switches are used to block or allow optical fibre signals and are essential to modern communications processing. A common household use of lyotropic liquid crystals is in hand soap. Liquid crystals also see novelty and serious applications as temperature measurement devices, such as small colour changing thermometer strips and in elastic stress/strain monitors.

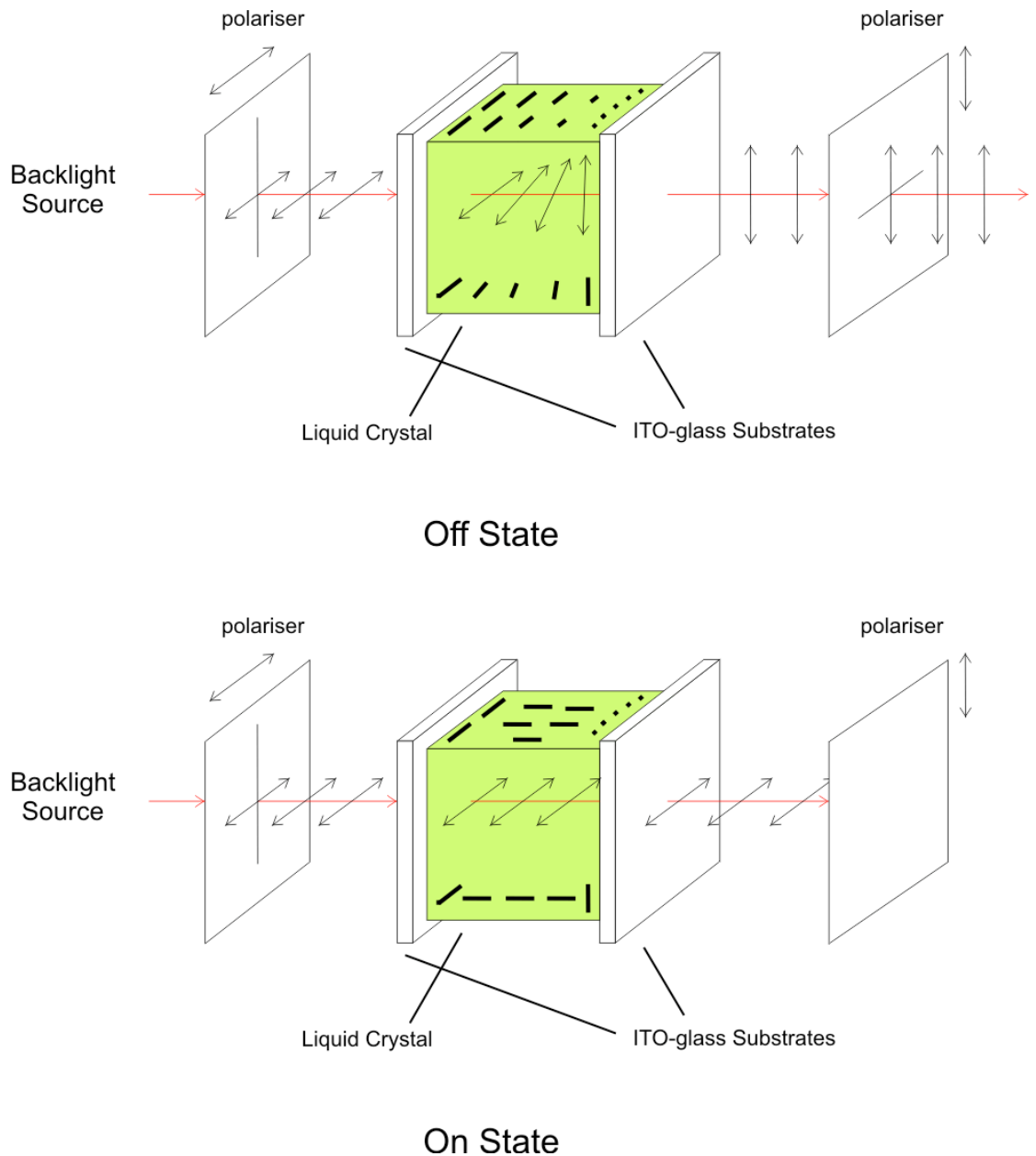


Figure 2.8 – Off and On states of a twisted nematic display

2.12 Sample Construction

All the experiments presented in this work are based on liquid crystals in the nematic phase. Cells with nematic LCs have been built and prepared at the School of Physics and Astronomy at Southampton University enabling us to rapidly build and examine cells in-house and at low cost. The entire process takes less than 2 days. The construction of the cell is achieved by first spincoating indium tin-oxide (ITO) glass

substrates with an alignment polymer. These polymers were first dissolved in chlorobenzene (CB) and typically mechanically rubbed once spincoated to induce the desired director configuration. Then the cell is constructed using 30um/10um Mylar spacers and finally filled with liquid crystal.

These samples are produced with commercially available liquid crystal mixtures E7 (provided by Merck) and LC1294-16[‡] of which some properties are presented in table 2.1. The alignment layers used in the study were *Poly-N-vinyl-carbazole* (PVK) and standard *Polyimide* (PI – from Aldrich), PVK doped with C₆₀ and the homeotropic surfactant PA ZLI-3334 (again from Merck). To prepare the mixtures, both the PVK and C₆₀ were dissolved separately in chlorobenzene, then a saturated concentration of the C₆₀ solution was added to the PVK solution. The calculated concentration of C₆₀ in the PVK layer once dry was measured to be 14.9% by weight. Optical and AFM measurements indicated the PVK layers to be around 100nm thick. The ‘thick’ polyimide layers used created were about 300nm thick.

	5CB [†]	E7*
Melting Temperature T _m (°C)	22.5 (295.5K)	-10 (263K)
Clearing Temperature T _c (°C)	35 (308K)	58 (331K)
n _e	1.71	1.748
n _o	1.53	1.522
Δn	0.18	0.224
k ₁₁	6.3x10 ⁻¹² N	11.7x10 ⁻¹² N
k ₂₂	3x10 ⁻¹² N	8.8x10 ⁻¹² N
k ₃₃	9x10 ⁻¹² N	19.5x10 ⁻¹² N

[†] for 589 nm at room temperature. Elastic constants from:

J. H. Erdmann, S. Zumer and J. W. Doane, *Phys. Rev. Lett.* **64**, 1907–1910 (1990)

* for 684 nm at 25°C. Elastic constants from:

E. P. Raynes, R. J. A. Tough, and K. A. Davies, *Mol. Cryst. Liq. Cryst. Lett.* **56**, 63 (1979)

Table 2.1 - Transition temperatures and physical properties of LCs in this study

[‡] A novel liquid crystal mixture, synthesised by our collaborators in Warsaw, Poland

The detailed steps of cell construction are as follows:

a) Spincoating

1. ITO glass is scribed and separated into $\sim 2\text{cm}^2$ slides
2. Slides are sonicated in an ultrasound bath of acetone for 10 minutes
3. The slides are cleaned with de-ionised water, isopropanol then more de-ionised water
4. Samples dried with air blower and in hot glass drying cupboard for 30 mins
5. Spincoat polymer alignment layer at 3000-4000 rpm for 30 seconds.
6. Move spincoated slides onto heating stage at 200° for 2hrs to bake polymer (polymer side up)
7. Allow heating stage to cool 30 minutes before removing slides.
8. Slides are mechanically rubbed using a custom built cloth rubbing machine (see figure 2.9).

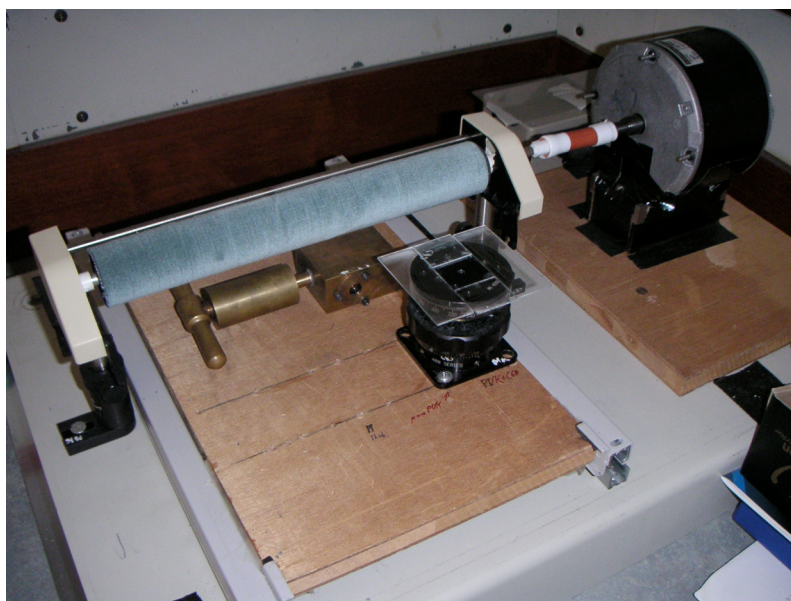


Figure 2.9 – Mechanical rubbing machine used to induce surface alignment direction

Once the surfaces are prepared, the cell must be filled with liquid crystal. This is generally achieved via capillary action, although in some cases such as for thin cells ($<10\mu\text{m}$), filling in a vacuum is required.

b) Cell Assembly and vacuum filling of liquid crystal

1. Substrates with Mylar spacers between are clamped together and glued with epoxy around the edges leaving a 5mm hole to introduce liquid crystal.
2. After 24 hours, cell is placed in vacuum chamber with liquid crystal mixture and pumped down to a pressure of 1-2 torr as shown in figure 2.10.
3. The liquid crystal mixture is gently agitated to remove air bubbles
4. A small amount of liquid crystal is then introduced at the cell opening and is drawn into the cell by capillary action. More droplets are added until the cell is completely filled
5. The cell is removed from vacuum and epoxy applied over the remaining hole to seal the cell.
6. The cells can be viewed under an optical polarising microscope to check homogeneity.



Figure 2.10 - Vacuum chamber setup

Chapter 3 – Photorefractivity in Liquid Crystals

Photorefractivity is a nonlinear optical effect whereby the refractive index of a material is changed under illumination [19][20]. It was first discovered for inorganic crystals but has since been observed in liquid crystals also. The photorefractive effect can, for example, be observed in dye-doped or fullerene doped liquid crystals [21][22][23]. There are a wide variety of photorefractive mechanisms in liquid crystals, and they often display much higher optical responses than their inorganic counterparts due to collective molecular reorientation.

The most common use of the photorefractive effect is in photorefractive holography where a non-uniform wavefront produced by two interfering coherent laser beams within the crystal is used to produce a non-uniform electric field distribution and a spatially varying index grating. The origin of this refractive index modulation in regular crystals relies on electro-optic effects, but in liquid crystals it can be related to collective reorientation of the liquid crystal molecules. The phenomenological explanation [24] of the mechanisms governing this process [22] includes the effects taking place in the bulk of liquid crystal, such as optical and dye-induced torque, a photorefractive space-charge field and the additional process of photoisomerisation [21]. Internal electric fields that can build-up inside a liquid crystal can be quite strong and via an electro-optic effect contribute significantly to refractive index modulation. Diffraction of laser beams by such gratings can reach efficiencies as high as 40% in dye-doped liquid crystals [25][21].

The photorefractive gratings can also be responsible for the transfer of energy from one beam to another (two beam coupling or TBC), as observed in conventional photorefractive materials, leading to coherent beam amplification. High two-beam coupling coefficients have been measured in dye-doped nematic liquid crystals [21], namely coefficients as high as 900cm^{-1} were observed.

The photorefractive effect thus has a considerable range of applications arising from both optical gain and the rewritable nature of the index grating. This opens up a whole slew of possible applications including spatial light modulators and optical image processing, optical switches, holographic data storage and many more.

However, doping liquid crystals with dyes is not the only method of achieving high two beam coupling gain. High diffraction efficiencies and gain have also been observed in liquid crystals with an additional photosensitive polymer layer [26][27][28].

The optical reorientation of liquid crystal molecules can also be strongly influenced by surface effects. For example, light absorption of a liquid crystal-dye mixture can lead to adsorption of photo-transformed dye molecules onto the polymer layer placed on a substrate surface. In such cases strong anchoring takes place and that can lead to permanent ordering of the liquid crystal molecules. Furthermore, as I will discuss later in this chapter, even for undoped liquid crystals, the presence of aligning, photosensitive layers, rather than bulk effects, can be critical for the build-up of photorefractive gratings.

In this chapter I will discuss the mechanisms and applications of photorefractive materials. I will start with a description of the first inorganic photorefractive materials and the main principles of how light interacts with materials to create refractive index gratings. In the second part of this chapter I will discuss the more recent developments in the area of photorefractive liquid crystal materials, how the photorefractive processes in such materials differ from their inorganic counterparts and the advantages of using photorefractive liquid crystals. Finally I will discuss the surface-induced photorefractive-like effect that has been the subject of my research and upon which my later experiments presented in chapter 5 are based. I will also explain how the build-up of the surface-induced photorefractive effect differs from the previously suggested explanations.

3.1 Mechanisms in Inorganic Photorefractive Materials

To exhibit the photorefractive effect, a material must be both photoconductive and

electro-optic. Many types of materials with these properties can be considered candidates. These include inorganic and ferroelectric crystals, semiconductors or polymers. Photorefractive materials now form an important and relevant underlying technology behind all-optical processing of information and phase conjugation. They are also important to emerging technologies in the fields of holographic data storage, solitons or bistability. One of the most attractive features of photorefractive materials is the high nonlinearity that can be induced with low power densities of light (in the range of microwatts to milliwatts per cm^2).

The photorefractive effect was first demonstrated in lithium niobate (LiNbO_3) [29] and has also since been observed in other oxides and semiconductors, notably barium titanate (BaTiO_3), potassium niobate (KNbO_3) and strontium niobate (SBN). It was discovered in 1966 by accident as an optical damage effect in electro-optic crystals that caused the breakdown of the spatial integrity of laser beams as they travelled through the crystal.

When two mutually coherent beams are incident on a photorefractive material, the interference pattern they create modifies the refractive index. The strength of this refractive index grating depends on factors such as the fringe visibility, the electro-optic coefficients that are accessed by the interaction geometry, and absorption. The formation of a strong grating may take some time (between tens of microseconds and several seconds) to develop, but once it is established, it may persist for a considerable time if no erasure mechanism is invoked.

Once illuminated by this spatially varying pattern, there are three main stages to the photorefractive process [19][20]. First is charge generation via photoionization and the drift/diffusion of these charge carriers. Second is the trapping of these carriers in the dark regions and lastly the change of refractive index as a result of the electro-optic effect. Let's examine this in more detail:

1. When two coherent laser beams with the same intensity are crossed so that they overlap within a photorefractive material, they interfere to form a sinusoidal intensity pattern. This is a spatially varying light intensity pattern which in turn generates a spatially varying pattern of photoionized charges in the sample, with

higher densities corresponding to the regions of high intensity.

2. The more mobile of these charges will tend to diffuse (or drift if there is an applied field) from the areas of high concentration (where the light intensity is high) into areas of lower concentration (dark fringes). The charges then become trapped in these dark regions via recombination. This process serves to create an electron distribution and a varying space-charge field. Because of the carrier mobility, the space-charge distribution is out of phase with the initial intensity pattern.
3. Since we are dealing with electro-optic crystals, this space charge field causes a refractive index change via the Pockels or Kerr electro-optic effects. The result is a spatially varying refractive index grating in phase with the space charge field and out of phase with the light intensity pattern.

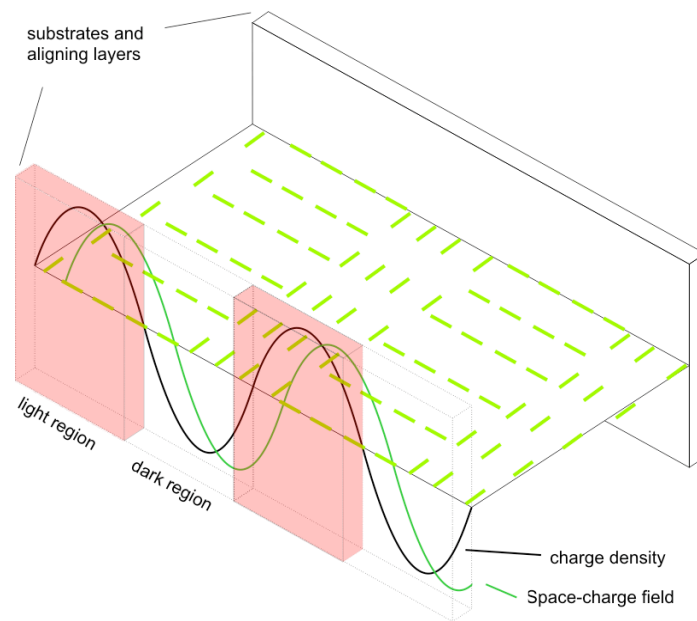


Figure 3.1 – Phase shift between intensity pattern and index grating

The grating can also remain for a time after the beams have been removed, depending on the lifetime of the trapped charge states.

There are a number of processes which can lead to refractive index change besides this one. These include optical torque and laser heating, but these other processes are local, that is; the index grating is in phase with the intensity pattern. The phase shift will be shown to be important in the next section.

3.2 Beam Coupling

Perhaps the most useful aspect of the photorefractive effect is the interaction between the incident waves and the photorefractive grating which can result in beam coupling and energy transfer between the two waves. Under certain conditions, the two writing beams can undergo self diffraction by the grating formed in the material.

If there is a non-local photorefractive mechanism such that the index grating is phase shifted from the light intensity pattern, it is possible to observe *wave mixing* effects and asymmetric energy transfer can take place between the two interfering beams as one diffracts into the other. This energy transfer manifests as a gain in one output beam intensity at the expense of the other. This process is called *two beam coupling* (TBC) and will be maximum when the two patterns are phase shifted by $\pi/2$. There is no energy transfer mechanism for local reorientation processes where the patterns are not phase shifted [19][20].

The strength of the grating can be characterised by its diffraction efficiency expressed as a percentage, and the beam coupling quantified by the gain observed in the probe beam. TBC is typically characterized by the gain ratio G ; defined as:

$$G = \frac{I_{probe+pump}}{I_{probe-pump}} \quad (3.1)$$

where $I_{probe+pump}$ is the intensity of the probe beam in the presence of the pump beam and $I_{probe-pump}$ is the intensity of the probe beam in the absence of the pump beam. First order diffraction efficiency is usually specified as:

$$\eta = \frac{I_{diff}}{I_0} = \sin^2 \left(\frac{\pi d \Delta n_{e,K}^{eff}}{\lambda} \right) \quad (3.2)$$

where I_0 is the intensity of an incident probe beam, I_{diff} is the intensity of the first order diffracted beam, d is the thickness of the liquid crystal layer and λ is the wavelength of the probe beam. $\Delta n_{e,K}^{eff}$ is the amplitude of the effective extraordinary refractive index

modulation averaged over the thickness and seen by light with wavevector K .

This energy transfer and gain is what makes photorefractive materials so useful for optical processing applications such as optical amplification and all-optical switching.

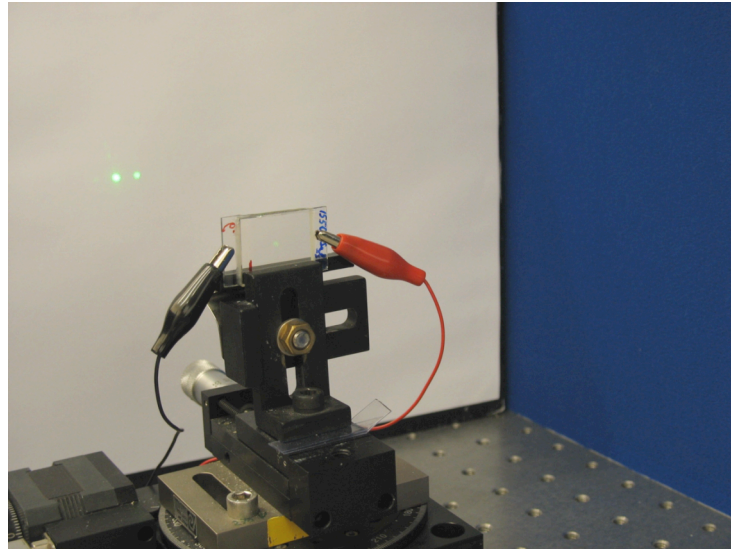


Figure 3.2 - Image of two beams undergoing the two-beam coupling process in a liquid crystal cell. The beam on the left is being amplified at the expense of the other.

Figure 3.3 shows an image of two beams undergoing the two-beam coupling process, with one beam amplified at the expense of the other beam being depleted. In this picture only the transmitted beams are imaged on a screen behind the cell. In most cases of beam-coupling in thin layers however, the diffraction includes several orders. This regime is called Raman-Nath and applies in cases of the grating spacing being comparable to the materials/cell thickness. It can be determined by a parameter known as the Quality Factor; Q [30], represented by:

$$Q = \frac{2\pi\lambda_0 L}{n\Lambda^2} \quad (3.3)$$

where λ_0 is the wavelength of the incident beams in vacuum, L is the distance the beam has travelled through the crystal, n is the refractive index of the crystal and Λ is the grating spacing. When Q is much less than one, the system is said to be in the Raman-

Nath regime and there will be several diffraction orders with intensities given by Bessel functions. When Q is larger than one, the diffraction is in the Bragg regime in which there is a specific angle at which only one diffraction order is produced and the others are destroyed via interference.

3.3 Photorefractivity in Liquid Crystals

The orientational photorefractive effect was observed in organic materials first in 1994 [31][32]. It has since been observed in many organic materials such as polymer composites, liquid crystals and combinations of the two. Photorefractivity has also been observed in dye-doped, polymer dispersed LCs, polymer stabilized LCs and fullerene-doped polymers such as PVK.[32]

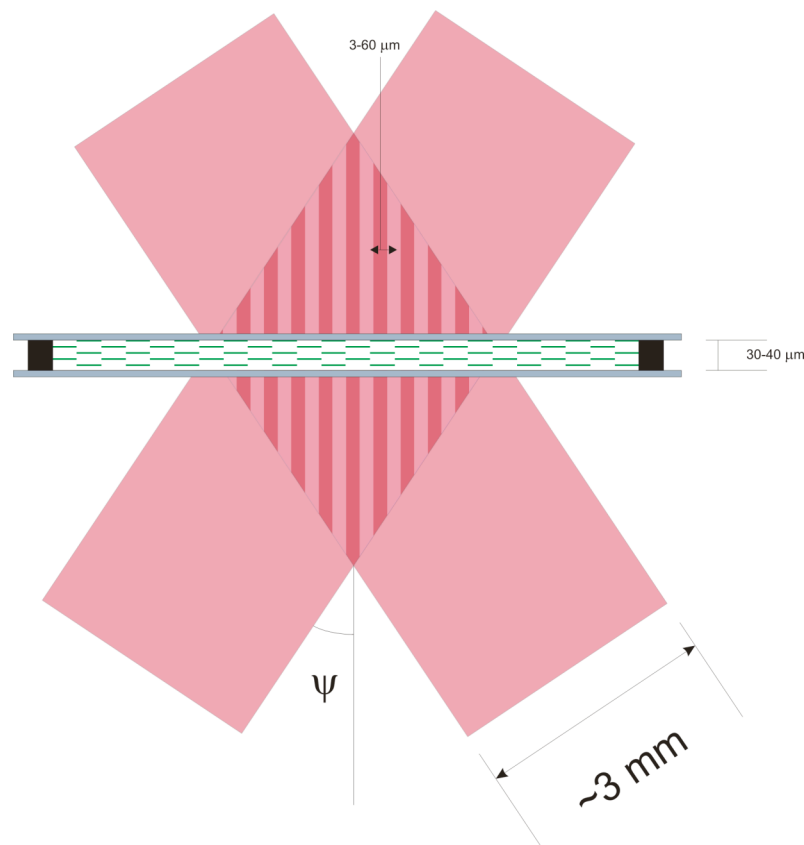


Figure 3.3 – Diagram of how the spatially varying intensity is formed in the cell with typical size parameters

Liquid crystals are very attractive candidates for such experiments as their high response compared to polymer materials exhibits significant refractive index change

even under weak applied fields (or optical intensities). Polymer materials generally need high applied fields (around $100\text{V}/\mu\text{m}$) whilst liquid crystals will respond to a field 1000 times smaller ($0.1\text{V}/\mu\text{m}$). Add to this the fact that they are much easier to fabricate than polymers and inorganic crystals, and they become an extremely attractive candidate for photorefractive applications.

A typical liquid crystal-based photorefractive system is usually composed of a photoconductive polymer or LC, doped with strongly nonlinear optical molecules to provide an enhanced reorientation contribution to the photorefractive effect. In these organic materials the photorefractive response is significantly higher than their inorganic counterparts. This is due in part to larger electro-optic coefficients but also to the additional orientational index change under applied field due to their high dielectric anisotropy. In fact the collective reorientation due to electric field is generally the significant factor in refractive index change for organic compounds. The orientational photorefractive effect can also be significantly enhanced by applying an external DC field with strength just below the threshold for the Freedericksz transition.

In 1997, I.C. Khoo et al. [21] observed record high gain in the liquid crystal 5CB doped with fullerenes, which in terms of exponential gain (also called gain coefficient or coupling coefficient) was of the order of 3000cm^{-1} . However, further experiments in similar systems by Zhang et al. [33] could achieve a maximum gain of 500cm^{-1} , while those carried out by Mun and his group [34] achieved a gain of only 90cm^{-1} .

Successful demonstration of beam coupling was also achieved by using dyes such as Rhodamine 6G or Methyl Red dissolved in liquid crystals such as 5CB. Dye doped systems demonstrate high diffraction efficiencies [22] and large intensity dependent refractive index changes [35], indicating high nonlinearity and strong electric space-charge fields. Wiederrecht et al. [36] studied nonlinear effects and beam coupling in such systems and reported exponential gains of the order of 600cm^{-1} . However, in subsequent investigations of dye-doped systems by other groups [27][37], no gain was observed. While the significant improvement of nonlinear optical response of liquid crystals by adding dyes is clear, the improvement and reliability of observing an efficient two-beam coupling gain was less obvious. Furthermore, dye degradation and

strong adsorption of dyes on the surfaces means a limited useful lifetime for dye-doped photorefractive liquid crystals.

For these reasons, I concentrated my studies on a different photorefractive structure. This study is based upon hybrid liquid crystal-polymer structures which consist of a pure undoped liquid crystal bulk sandwiched between photorefractive polymer alignment layers. This system is based upon using layers of the photorefractive polymer *Poly-N-vinyl-carbazole* (PVK) doped with fullerene such as C₆₀. High exponential gain of 3700 cm⁻¹ in similar structures, namely using PVK doped with TNF, was measured by Bartkiewicz and Kajzar [28][38]. A lower value of gain was reported by Mun et al. [34], suggesting that a better control and understanding of the underlying mechanisms is required.

Hence, in my research I focussed on exploring in more detail the nature of interactions, especially those associated with surface effects, involved in creating refractive index photorefractive gratings. This objective appeared more relevant rather than attempting to achieve even higher two-beam coupling gain.

3.4 Surface Induced Photorefractive-like Effect

There have been several reports on beam coupling observed in pure nematic liquid crystal cells combined with polymer alignment layers [31][32][39][40] that may have another mechanism. It has been demonstrated that strong photorefractive effects are present in cells with specific combinations of liquid crystal and photoconducting polymer alignment layers [39] such as *Poly-N-vinyl-carbazole* (PVK) and under an applied external field. Evidence of the photorefractive effect was also observed in other liquid crystal-polymer systems with photoelectric interface activation [41] as well as in pure liquid crystals as a result of the Helfrich-Carr effect [42]. Moreover, the effect seems highly dependant on experimental geometry. It is important to note these effects are seen in cells with pure liquid crystal materials and polymer alignment layers, and that they are not doped during manufacture (although ion production at the surface may play a role).

In my study I concentrated on PVK polymer-liquid crystal systems, as the gain observed using this combination was the highest and therefore exploring the underlying mechanisms for this particular configuration was most relevant and needed.

It is widely accepted that it is the reorientation of liquid crystal molecules that leads to the formation of a two-beam coupling grating. However, the underlying mechanism behind the build-up of the space-charge field and the resultant refractive index profile is not understood. Several groups investigating these effects have proposed differing explanations of the mechanisms involved in their observations.

Khoo [43], as well as Rudhenko and Sukhov [32] postulated explanations for their observations in nematics, but both rely upon bulk effects and do not consider the interactions at the liquid crystal-polymer interface. Other authors [44] presented accounts inferring the boundary conditions play an important role in the photorefractivity of these systems and suggesting photoactivation of the interface as the mechanism [40].

Work by Pagliusi and colleagues [39][45] investigated a number of combinations of liquid crystals and polymer layers. Their results clearly showed that certain polymer layers such as PVK produced high beam coupling gain with the LC E7 but not with other liquid crystals. Similarly E7 will not exhibit beam coupling with all alignment layers. Their experiments also suggested that these effects could be observed in non-photoconductive polymers. It rapidly became clear that the interface between the polymer aligning layers and the LC was likely playing a dominant role somehow. A mechanism of charge build-up at the interface surfaces was suggested, where the concentration was altered by light-induced ion-desorption [46].

Ono et al. [47] suggested that in their experiments the space charge field is created due to the photo-generation of charges in a PVK layer, and that these charges were becoming trapped in an adjacent insulating poly-vinylalcohol (PVA) layer. This model requires the presence of an extra PVA layer which is not present in many of the reported experimental results.

Building on this work, Mun et al. [34] investigated a variety of differently doped alignment layers and liquid crystals, including the configurations and conditions studied by Ono. They proposed a model in which the space charge field is generated in the LC bulk due to photogenerated charges, with these charges being trapped at the LC-polymer interface. They argued that PVA layers are not needed. The mechanisms for the formation of the space charge fields in these models [21][23][34] were quite different, but nevertheless relied upon the same photorefractive model of charge-generation, transport and trapping as used for solid-state materials. Additionally, they also assumed that an applied DC field causes reorientation without illumination.

My work on PVK-liquid crystal systems as well as the results obtained by the other members of our group [48][49][50] was to first confirm experimentally strong beam coupling and diffraction in such PVK-LC cells when illuminated by an interference pattern. Secondly, I measured and captured images of single beam light transmission through the cells to inspect in more detail the response to light and applied electric field. In particular, I intended to resolve how important the surface interface and charge layers are as opposed to bulk reorientation effects. Indeed, the process of ‘Surface-Induced-PhotoRefractive-Effect’ (SIPRE) was suggested in 1998 [45][51][52]. The fundamentals of this process are still not understood fully and several theories have been proposed including a photoinduced change in ion concentration at the interface [53][52]. The key concept in these theories is that they must account for the non-local reorientation which facilitates beam coupling. Building on the work done by these groups previously, a new qualitative model incorporating all these aspects was proposed.

3.5 Proposed Mechanism for the SIPRE

Here I will present a qualitative model to explain the previous experiments on beam coupling [40][48][49][50][54][55]. It incorporates both the influence of applied field and an explanation for non-local reorientation. The key innovation proposed is that the build-up and discharge of surface charge layers are responsible for two-beam coupling gain rather than standard photorefractive processes such as charge excitation, drift and trapping.

The system considered here consists of layers of the photorefractive polymer PVK combined with a nematic liquid crystal. *Poly-N-vinyl-carbazole* (PVK) is a transparent thermoplastic material that possesses good thermal and chemical stability. Pure PVK is a good insulator in the dark and also under visible light illumination [56]. However, it becomes photoconductive upon exposure to light in the ultraviolet region. PVK has been explored in some details, as one of the best photorefractive polymers. It is particularly efficient as photoconductive material being a charge-transporting polymer with good hole conductivity and high concentration of active charge transport sites (carbazole groups). Doping PVK with sensitizers such as trinitrofluorene (TNF) or carbon-60 (C_{60}) shifts the absorption of PVK into the visible band via the formation of a charge transfer states and can increase PVK conductivity

To explain this photorefractive mechanism, it is necessary to first consider the PVK: C_{60} structure under an applied DC field with no illumination. The mobile charges (ions) within the LC drift towards the corresponding electrodes and build up a double charge layer at the LC-polymer interface. Once this charge build up becomes large enough it will act to screen the LC bulk from the external field. The voltage drop can then be regarded as occurring mostly across the photo-conducting polymer layer. As a result, the electric field does not penetrate into the LC bulk and the director configuration remains in its original orientation. Such surface charge layers had been reported in nematics [57] and other systems such as dye-doped liquid crystals, but prior to this explanation, not in LC-photoconducting polymer structures.

Since the PVK layer is photoconducting, illumination of the sample causes charge flow and photo-induced recombination of the charge carriers at the LC-polymer interface. This process of discharge, removes the shielding field, allowing the applied field to penetrate into the LC bulk as demonstrated in figure 3.4. Under spatially non-uniform illumination such as that created by an interference pattern, the resulting surface electric field also becomes spatially varying. In the illuminated regions the applied electric field can penetrate into the LC, causing local reorientation and leading to the formation of a modulated director profile and a refractive index grating.

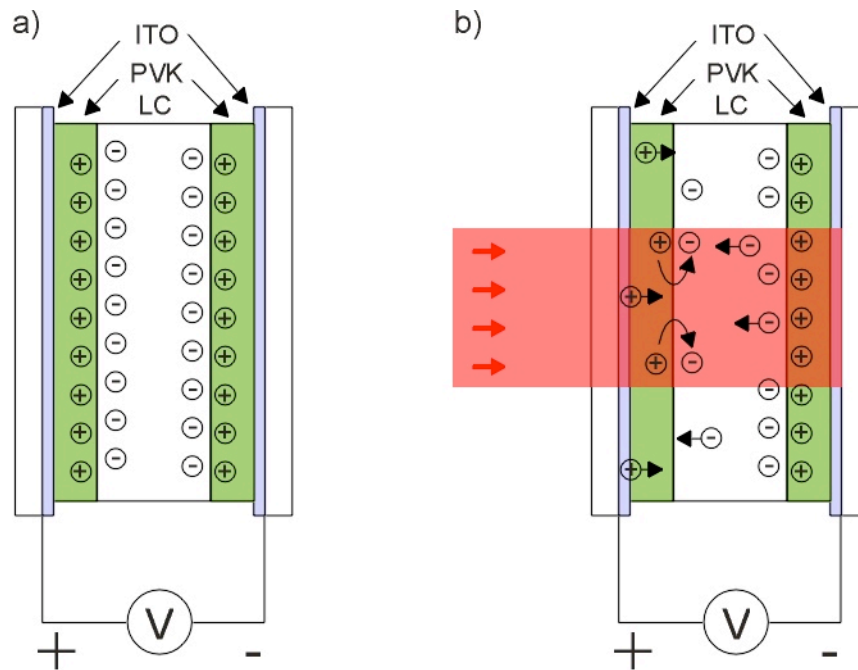


Figure 3.4 – Charge recombination at the interface. a) charge layers build up at the LC-PVK interface under applied field, screening the LC bulk. b) Illumination causes recombination of the charges at the interface, removing the screening effect.

Since a DC bias is required for this process, the transmission of light through such a system can also be controlled by varying the applied field. The system can be designed so as to be driven only by the incident light at a particular wavelength. Figure 3.5 presents a typical scheme with light induced and controlled reorientation. Figure 3.5 a) shows the initial conditions in a PVK:C₆₀ cell with an applied DC field. There is no reorientation without illumination. Once illuminated, reorientation takes place as in image b), but only when the polymer layer is photosensitive to the wavelength of the incident light. This is the visible and near-infrared for PVK doped with C₆₀. In image c), it can be seen that there is no response for pure PVK under visible light, since it is only photo-conducting in the UV region. The system can thus be tailored to respond to a particular spectral region if desired.

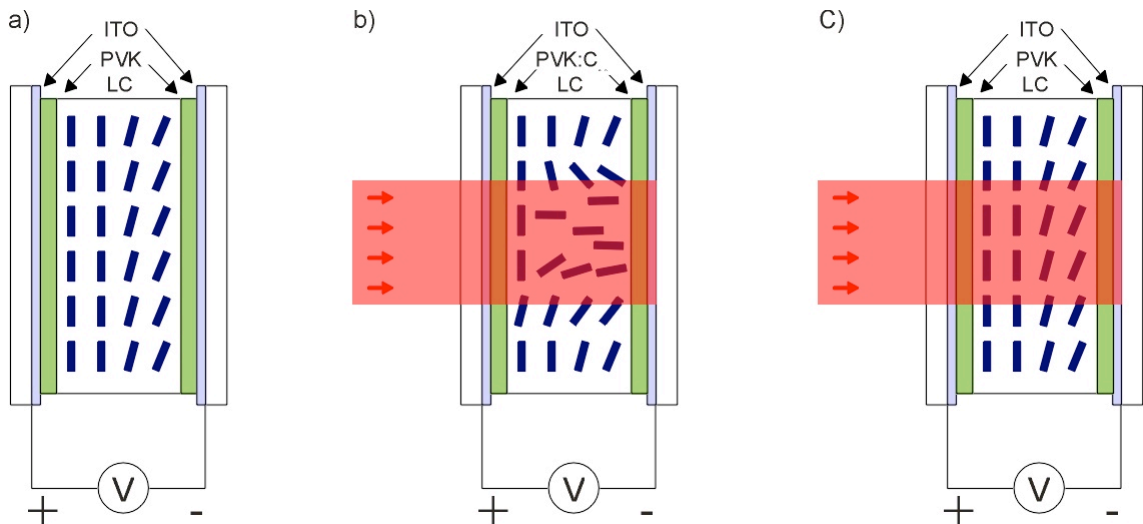


Figure 3.5 – Tailored wavelength response. a) Initial condition with no illumination b) Reorientation under visible illumination for PVK:C₆₀ c) No reorientation with visible light for the pure PVK system

In the LC-polymer structures considered here, the reorientation process is a local one. This means that there is no phase shift between the intensity pattern and the reorientation grating. However, to observe beam coupling, a phase shift of $\pi/2$ is required. Both in my beam coupling experiments and those carried out by other members of our group, beam coupling was observed only in certain geometries, namely when the bisector of the writing beams was at a large angle to the surfaces of approximately 40° . It is therefore proposed that the phase shift between the writing beams and the grating is purely a result of the angle the grating vector makes with the incident intensity pattern. In fact, the condition for a $\pi/2$ phase shift necessary for beam coupling might not be fulfilled in the whole modulated bulk of the LC. At certain angles, only part of the refractive index grating may fulfil these criteria. When the angle between the grating vector and incident beams bisector is in the 30° - 50° region, this part is sufficiently large to fulfil the beam coupling conditions. Figure 3.6 is taken from reference [48] and shows the relationship between angle of incidence and phase shift

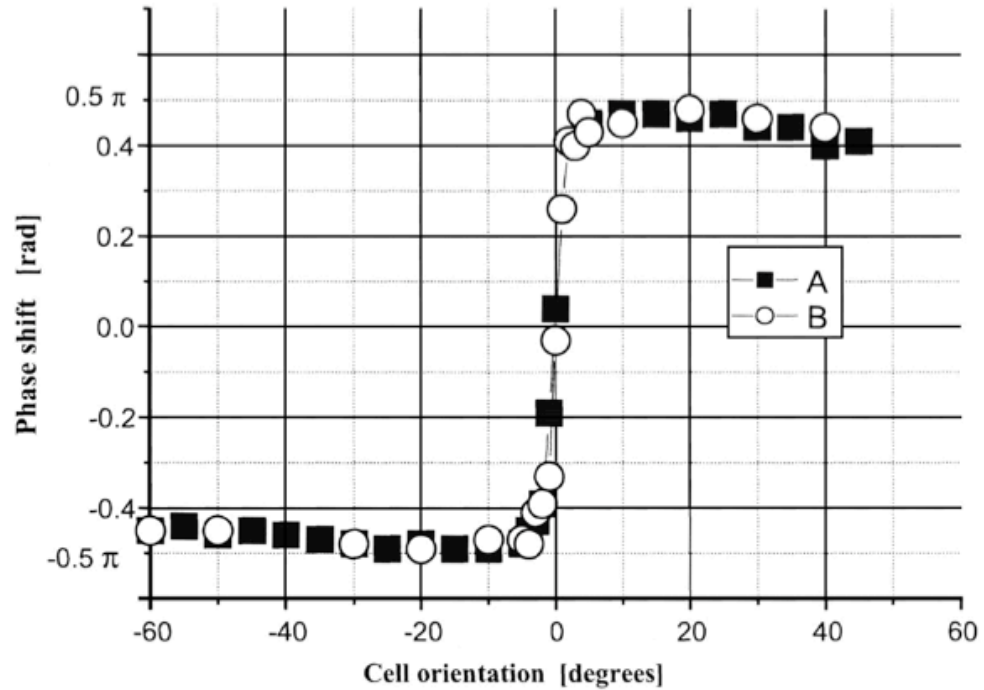


Figure 3.6 – Graph from reference [48]. Dependence of the phase shift on cell orientation. Curves A and B were measured for positive and negative dc bias on the PVK:C₆₀ substrate, respectively.

3.6 Summary

The SIPRE offers the chance of much higher beam-coupling gain response than dye-doped LC systems. There is a lot of macroscopic application focussed data for diffraction efficiency and gain in such gratings, but little is known about the mechanisms involved in such a reorientation. There have been many proposals for possible mechanisms, but the description presented here is the only one which also explains the observed effects under just a DC field with no illumination and the origin of the phase shift.

In the case I considered, the periodic modulation of electric field was induced by high contrast in PVK conductivity when illuminated by light interference pattern. In bright fringes, there was high photoconductivity and electric field penetration to liquid crystal bulk and in dark fringes, low dark conductivity meant no electric field reaching liquid crystal. It is worth stressing that periodic modulation of applied electric field can be achieved via other methods, such as using patterned electrodes or indeed using solid-

state photorefractive windows with periodically induced space-charge field. Hence, the models developed here can easily be applied to a wide range of liquid crystal systems that, indeed, are currently pursued and developed.

Whilst beam coupling results provided an important base for the qualitative description of this process in LC-PVK:C₆₀ structures, it is difficult to achieve more progress without more detailed knowledge of the liquid crystal orientation across the cell. In particular, there was the need to reproduce and simulate the electric field, director and refractive index profiles as well as determining the critical experimental parameters for beam coupling. While such profile maps will be useful for optimising TBC gain, the topic goes beyond just the specific case of two-beam coupling and indeed concerns the wider case of liquid crystal response to periodically modulated electric field

However, being able to understand and predict the profile of a refractive index grating is not a straightforward task. The modulation of refractive index is not uniform across the whole LC bulk. The maximum reorientation takes place in the middle of the cell, where anchoring and the influence of aligning layers on substrates is the weakest. Furthermore, the director distribution is not necessarily symmetric, as the aligning layers on the two substrates can impose different pretilt angles and indeed different anchoring energies. For these reasons, an investigation into surface s in non-periodic (uniform) director profiles was determined to be the best starting point and led to the next part of my work.

Chapter 4 – Uniform Director Measurements

A nematic liquid crystal between two glass plates has a director profile corresponding to the minimum free-energy configuration affected by the strength and orientation of the surface anchoring and the elastic properties of the liquid crystal. Assuming strong anchoring at the surfaces as described in chapter 2, the liquid crystal can be assumed to be a uniaxial crystal whose optic axis (the long axis of the molecules) is homogeneous through the sample. The orientation of the optical axis can then be found via birefringence experiments, thus allowing the determination of the pretilt angle from the cell surface.

The magnitude of pretilt angle is an important parameter of a liquid crystal cell since the alignment of liquid crystal molecules affects the orientation of the refractive index ellipse in the uniaxial cell. Tilt angle also affects the electric field response and the existence of the Freedericksz transition making accurate measurement of the pretilt angle in a liquid crystal cell very important in determining the optimal experimental (and material) parameters for high gain in TBC experiments.

There are several methods of measuring pretilt in a liquid crystal cell. These include the magnetic null method, capacitance techniques and birefringence measurements such as the crystal rotation method [58]. It is important to note that each of these methods measures an average pretilt within a volume of liquid crystal defined by the thickness of the cell and the area of the light beam. Local variations are of course possible within this region. The crystal rotation method was chosen for the experiments in this research. This method is widely used for characterising cells due to ease of experimental construction and the ability to attain the value of pretilt angle to a precision of less than a degree, regardless of cell thickness. The crystal rotation method has been used for many years, yet there is still a lack of explicit general numeric or analytic derivations of the formulae for the pretilt angle.

The aim of this work in this chapter was to systematically study, analyse and optimize the current approaches to pretilt angle calculation from crystal rotation data. Traditional approaches to crystal rotation are limited to determining pretilt angles which deviate less than 20° from planar or homeotropic alignment. Thus, the aim is to find a general expression for pretilt angle from crystal rotation data that can be applied to cells with any value of pretilt and to see how this is derived. In particular, the limits on the available methods and their physical origins will be studied and an attempt made to reduce the limitations. A summary of the two main calculation methods is presented along with the limitations of each method and the physical origins of the limits. An attempt at an analytical expression for pretilt angle and its inherent limits is also presented along with measurements on a series of cells.

4.1 Why Pretilt Angle?

Knowledge of the pretilt angle in a sample can be very important for display applications. A LCD with pretilt will tend to prefer a particular re-orientation direction under applied field and will thus avoid transient and permanent defects between domains from occurring. Such defects lead to poor contrast, brightness and viewing angles. Knowledge of pretilt angle is therefore very important to the display industry.

Pretilt effects obviously govern the direction of the optical axis and the ease of reorientation and therefore can influence beam coupling experiments. Knowledge of the pretilt angle is necessary to understand such experiments. It is also observed from two-beam coupling experiments (see section 5) that maximum diffraction efficiency is observed at rotation angles near 50° when the cell (and thus the director) is at an angle to the bisector of the incoming beams. There is interest in replicating this situation using cells with a high pretilt angle at normal incidence and if successful will provide design flexibility for beam switching or SLM applications.

Pretilt is also very useful as a monitoring method. A simple and relatively quick scan can reveal quantitative changes in the director profile over time, or be used to analyse memory effects where a polarising microscope could reveal only qualitative information. This is a subject of some significance since there is much interest in using

such memory effects on PVK to deliberately adjust surface properties for gratings or waveguiding.

4.2 Determining Uniform Director Orientation

A uniaxial crystal is birefringent and has two intrinsic refractive indices $n_o = n_{\perp}$ and $n_e = n_{\parallel}$. For the rod shaped molecules in a calamitic liquid crystal, n_e is experienced by light vibrating (polarised) along the long molecular axis and n_o by light vibrating perpendicular to this. Light which enters the liquid crystal is split into two components; the ordinary and extraordinary waves which see effective refractive indices n_{ord} and n_{ext} respectively. The refractive index along the path of the ordinary ray is given by the intrinsic ordinary index such that $n_{ord} = n_o$. The refractive index along the path of the extraordinary ray is path dependant and is a function of both the intrinsic refractive indices n_e and n_o . The intrinsic birefringence is given by the difference in the two refractive indices $\Delta n_i = (n_e - n_o)$ whilst the birefringence experienced in a particular propagation direction is given by the difference between n_{ext} and n_{ord} ; $\Delta n_e = (n_{ext} - n_{ord})$.

One method of observing a uniaxial structure is to look at the phase delay (effective birefringence) between the ordinary and extraordinary rays after passing through the crystal. When the wavevector is parallel to the director, both waves see the same refractive index; n_o and this path difference will be zero. When the wavevector is perpendicular to the director, each wave sees a different refractive index and the phase difference will be maximal. This relative phase difference is known as the retardation and can be found by observing the transmission through crossed polars and using the following expressions [59] [60] [61]:

$$\text{Retardation: } \Delta\varphi = \frac{2\pi d}{\lambda_0} f(\alpha, \psi) \quad (4.1)$$

$$\text{Transmission: } T = \frac{1}{2} \sin^2 \left[\frac{\pi d}{\lambda} f(\alpha, \psi) \right] \quad (4.2)$$

Where $f(\alpha, \psi)$ is a birefringence function first specified by [62]:

$$f(\alpha, \psi) = \frac{n_o^2 - n_e^2}{n^2} \sin \alpha \cos \alpha \sin \psi + \frac{n_e n_o}{n^2} (n^2 - \sin^2 \psi)^{\frac{1}{2}} - (n_o^2 - \sin^2 \psi)^{\frac{1}{2}} \quad (4.3)$$

and d is sample thickness, λ_0 is the vacuum wavelength of the probe beam, n_e and n_o are the intrinsic refractive indices as specified above and $n^2 = n_o^2 \cos^2 \alpha + n_e^2 \sin^2 \alpha$. α and ψ are the pretilt and incident angles respectively.

Due to the birefringence of the liquid crystal, a beam of light exiting the cell is a superposition of the ordinary and extraordinary waves. Since one wave will have travelled slower than the other through the medium the linear polarization at the output of the cell will have rotated relative to the polarization of the incident light, seen as a transmission change through crossed polars. Depending on the angle of incidence, the effective refractive indices n_{ord} and n_{ext} seen by the beam will change, resulting in the angular transmission function in equation 4.2.

Measuring crossed polarised transmission for a range of incident angles allows us to determine the incident angle corresponding to a retardation minima or maxima and calculate the optical axis direction via refraction laws.

4.3 Experimental Setup

The simplest geometry of a crystal rotation setup is shown in figure 4.1. A cell is placed on a rotation stage between two crossed polarisers each at $\pm 45^\circ$ to the plane perpendicular to the cell substrates and containing the easy-axis of the molecules. Care is taken to ensure that the cell surfaces lie perpendicular to the wavevector of the incoming beam by aligning the incident and reflecting beams.

Incident angle was varied between $\pm 60^\circ$. The system was positioned within a dark box to eliminate ambient noise. To vary incident angle, the sample was rotated about the axis perpendicular to the easy axis (molecular direction induced by rubbing) but parallel to the substrate plane. The transmission was then observed through crossed polarisers as shown in the diagram in figure 4.1. This is the *crystal rotation method* (CRM).

Code was written using the Wavemetrics IGOR program to control a STANDA stepper motor through a dedicated interface card. The step size could be adjusted, but was typically set to take data in steps of 0.2° degrees of rotation between $+60^\circ$ to -60° from normal incidence. I developed a software system for experimental control, data collection and analysis. I developed a graphical interface to the system (see fig. 4.2) which improved data management speed and allowed photodiode selection, manual stepper motor control and data analysis functions. The photodiode is controlled by a National Instruments data acquisition card. At each data point, the average of 200 photodiode readings are taken and used as the transmission reading for that angle of incidence.

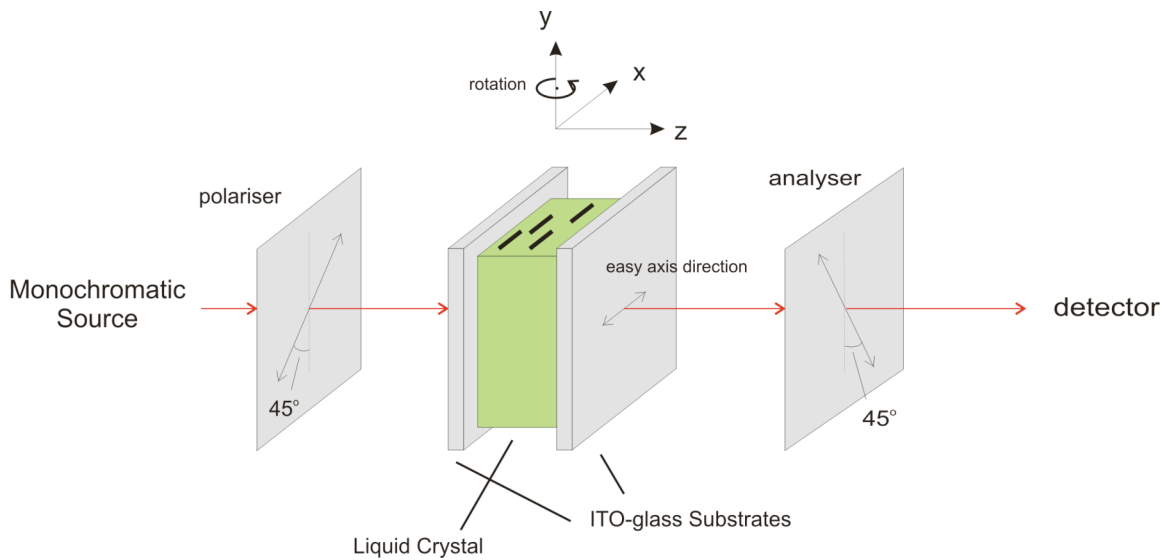


Figure 4.1 – Diagram of experiment to determine optical axis and pretilt

Once the data has been collected, the system can calculate pretilt angle from the angular transmission data using one of several calculation methods presented later in this chapter. Since its creation, this system has become a valuable research tool for sample characterisation, and it is hoped that it can later be extended to cover a wider range of cell types.

Because such a system is transmission-based, any observed birefringence will be an average through the crystal and also across the cross section of the beam (which has a Gaussian profile). Spatial resolution is thus limited by spot size in the plane of the surfaces.

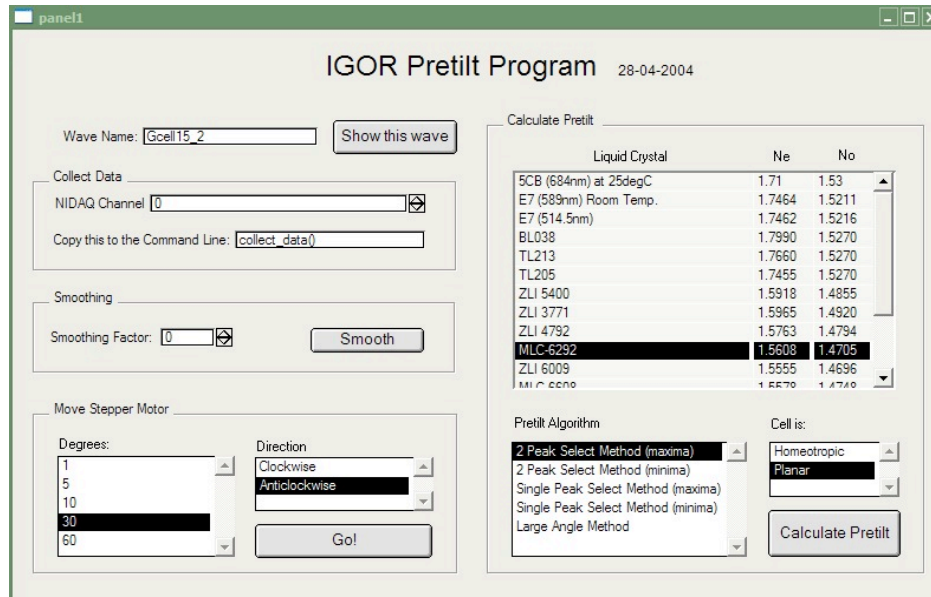


Figure 4.2 – Screenshot of pretilt experiment control software

The system has extremely good reproducibility at any one point on the sample and noise is low. The transmission measurement is time averaged over 200 photodiode measurements to reduce noise. The validity of the measurement can also be tested by rotating the sample by 180° and measuring the transmission in reverse. The resultant transmission pattern should match the original, but be reflected about an incident angle of zero degrees.

The symmetry point in angular transmission corresponds to a retardation minima or maxima. The symmetry point is selected either directly or calculated as the halfway point between two peaks either side of it. The software provides analysis of pretilt angle after a symmetry point is selected (the programs for this are presented in Appendix A). The calculation is based on the approximations in Ong et. al. [63] (equations 4.4 and 4.5), but can also give the full refraction law solution.

For planar cells (wavevector perpendicular to optic axis):
$$\alpha = \frac{\psi}{n_e + n_o} \quad (4.4)$$

For homeotropic cells (wavevector parallel to optic axis):
$$\alpha = \frac{\psi}{n_o} \quad (4.5)$$

4.4 Calculating the Angle of the Optic Axis

Snell's law of refraction is used to calculate the refraction angle in the LC medium as a function of the angle of incidence ψ . Substituting the angle of incidence corresponding to the transmission intensity symmetry point $\psi = \psi_x$ from crystal rotation data, gives the refraction angle parallel or perpendicular to the optic axis of the molecules. For the situation where the beam is refracted along the optical axis, this is simple as it only sees the refractive index n_o . Assuming the material interfaces are parallel to the cell substrates and using a ray-optics model as shown in figure 4.3(a), Snell's law of refraction then states:

$$\begin{aligned}n_1 \sin \psi &= n_2 \sin \theta_{t1} \\n_2 \sin \theta_{t1} &= n_3 \sin (90 - \alpha)\end{aligned}\quad (4.6)$$

thus:

$$\alpha = 90 - \arcsin\left(\frac{n_1}{n_o} \sin \varphi_x\right)\quad (4.7)$$

where $n_3 = n_o$ since the propagation direction is along the optical axis and assuming $n_1 = 1$ for air. The refractive indices of the glass and polymer layers do not enter into the calculations. The small angle approximations $\sin(\psi) = \psi$ and $\arcsin(\psi) = \psi$ (valid with 2% error for $\psi \leq 20^\circ$) can be applied to equation 4.7 which then becomes:

$$\alpha = 90 - \frac{\varphi_x}{n_o}\quad (4.8)$$

Equation 4.8 agrees with approximations in [58] and [63]. The law of refraction/total internal reflection at the air-LC/LC-air interfaces limit the possible refraction angles into the cell and therefore the range of pretilt angles which can be determined. The maximum refraction angle (critical angle θ_c) is determined by substituting $\psi = 90^\circ$ into equation 4.7. For E7 at room temperature using $n_{air} = 1$ and $n_{o,LC} = 1.52$ this becomes $\theta_c = 41.13^\circ$, limiting pretilt to $\alpha > 90 - \theta_c = 48.87^\circ$.

The case for refraction perpendicular to the optical axis is shown in figure 4.3(b) and is more complex since the incoming E-field now has components in both n_e and n_o . To pass perpendicular to the optic axis, the ray must come from the other side of the cell normal, denoted as a negative angle of incidence to distinguish incoming direction. The ordinary ray experiences the non path-dependant refractive index n_o whilst the e-ray experiences some (path-dependant) function of n_e and n_o . Thus a simple expression cannot be derived in this case unless some average of the two refractive indices is used and this will be subject to error. Another method is required to calculate pretilt close to the planar case.

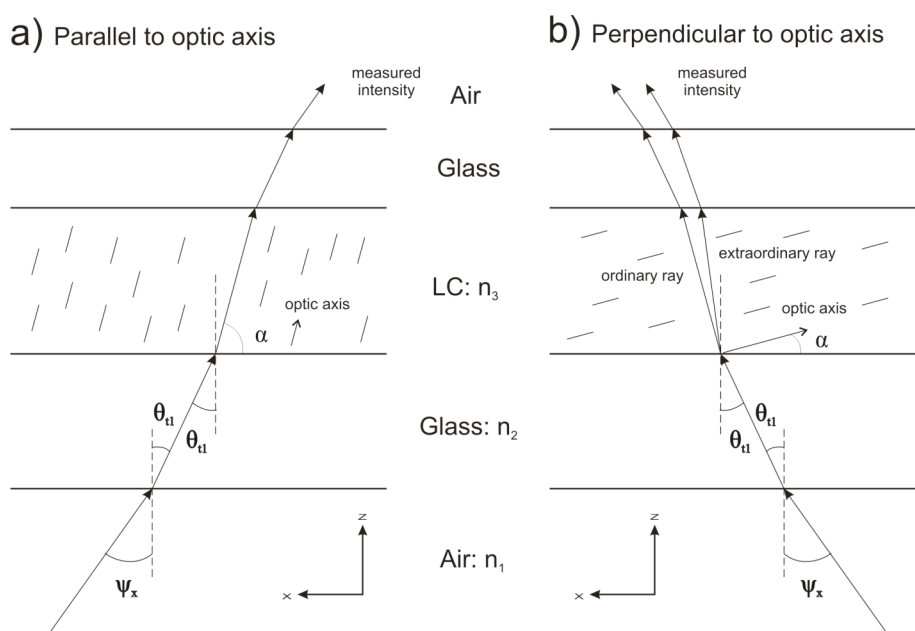


Figure 4.3 - The relationship between ψ_x and α

4.5 Differentiation Method

For any situation where the wavevector of the incoming light is not parallel to the optic axis, the E-field will have components in both n_e and n_o and a more complex relationship is required. The effective birefringence of such a system depends on the angle of incidence, pretilt angle, n_e and n_o . The authors in reference [63] presented pretilt calculations based on substituting measured transmittance and cell thickness, into the transmission equation, giving an implicit relationship between ψ and α . An

improvement to this method was demonstrated by Scheffer and Nehring [58] who determined a relationship by differentiating the birefringence function of the cell $f(\alpha, \psi)$ with respect to ψ and equating to zero at the maximum (symmetry point). If $\delta = df(\alpha, \psi)$ from equation 4.3 then when the retardation is maximum:

$$\left(\frac{d\delta}{d\psi} \right)_{\psi=\psi_x} = 0 \quad (4.9)$$

so:

$$\left(\frac{df}{d\psi} \right)_{\psi=\psi_x} = 0 \quad (4.10)$$

which becomes:

$$\left[\frac{1}{\sqrt{n_o^2 - \sin^2 \psi_x}} - \frac{n_o n_e}{n^2 \sqrt{n^2 - \sin^2 \psi_x}} \right] \sin \psi_x = \frac{n_e^2 - n_o^2}{n^2} \sin \alpha \cos \alpha \quad (4.11)$$

$$= \frac{n_e^2 - n_o^2}{2n^2} \sin 2\alpha \quad (4.12)$$

The resulting equation no longer depends on transmission value, cell thickness or wavelength. This expression can be solved graphically by plotting equation 4.13 as a function of α , and finding the corresponding α for which $F(\alpha) = 0$.

$$F(\alpha) = \left[\frac{1}{\sqrt{n_o^2 - \sin^2 \psi_x}} - \frac{n_o n_e}{n^2 \sqrt{n^2 - \sin^2 \psi_x}} \right] \sin \psi_x - \frac{n_e^2 - n_o^2}{n^2} \sin \alpha \cos \alpha = 0 \quad (4.13)$$

It is obvious that measurement of this value will be limited again by the critical angle of refraction, limiting tilt angle measurement to $\alpha < \theta_c$. A greater restriction however is placed on the pretilt as a result of the mathematical method here. The maximum measurable pretilt which can be obtained using this method can be found by solving equation 4.13 with $\psi_x = 90$. Using parameters for E7, $n_e = 1.74$ and $n_o = 1.52$, this limit is 16.3° .

4.6 Analytical Representation

Equation 4.13 can be solved graphically, but an analytic expression for α would be quicker and easier to solve. This is obviously not possible through simple rearrangement due to the multiple sin and cos terms in α . In conjunction with [64], I have derived an analytical approximation for α using a Taylor expansion. Assuming the difference between n_e and n_o is small compared to their values and starting from the birefringence function in equation 4.3:

$$f(\alpha, \psi) = \frac{n_o^2 - n_e^2}{n^2} \sin \alpha \cos \alpha \sin \psi + \frac{n_o n_e}{n^2} \left(n^2 - \sin^2 \psi \right)^{\frac{1}{2}} - \left(n_o^2 - \sin^2 \psi \right)^{\frac{1}{2}} \quad (4.14)$$

where $n^2 = n_o^2 \cos^2 \alpha + n_e^2 \sin^2 \alpha$ and n_e and n_o are known.

The difference between n_e and n_o is usually of the order of 10%. Setting one as being a small deviation from the other introduces the expansion:

$$n_e^2 = n_o^2 (1 + \varepsilon) \quad (4.15)$$

This assumes that $n_e - n_o$ is small and there will therefore be an error in the final solution since the difference between them is $\approx 10\%$ of their values. This gives an expression for n as:

$$\begin{aligned} n^2 &= n_o^2 (1 + \varepsilon) \sin^2 \alpha + n_o^2 \cos^2 \alpha & (4.16) \\ &= n_o^2 \cos^2 \alpha + \varepsilon n_o^2 \sin^2 \alpha + n_o^2 \sin^2 \alpha \\ &= n_o^2 (\cos^2 \alpha + \sin^2 \alpha) + \varepsilon n_o^2 \sin^2 \alpha \\ &= n_o^2 (1 + \varepsilon \sin^2 \alpha) \end{aligned}$$

Substituting into the birefringence function:

$$f(\alpha, \psi) = \frac{n_o^2 - n_o^2 (1 + \varepsilon)}{n_o^2 (1 + \varepsilon \sin^2 \alpha)} \sin \alpha \cos \alpha \sin \psi$$

$$\begin{aligned}
& + \frac{n_o^2 \sqrt{1 + \varepsilon}}{n_o^2 (1 + \varepsilon \sin^2 \alpha)} \sqrt{n_o^2 (1 + \varepsilon \sin^2 \alpha) - \sin^2 \psi} \\
& - \sqrt{n_o^2 - \sin^2 \psi}
\end{aligned} \tag{4.17}$$

$$\begin{aligned}
& = \frac{-\varepsilon \sin \alpha \cos \alpha \sin \psi}{1 + \varepsilon \sin^2 \alpha} \\
& + \frac{\sqrt{1 + \varepsilon [n_o^2 (1 + \varepsilon \sin^2 \alpha) - \sin^2 \psi]}}{1 + \varepsilon \sin^2 \alpha} \\
& - \sqrt{n_o^2 - \sin^2 \psi}
\end{aligned} \tag{4.18}$$

$f(\alpha, \psi)$ can be expressed as the Taylor expansion:

$$f(\alpha, \psi) = \varepsilon f_1(\alpha, \psi) + \text{Order}(\varepsilon^2) \tag{4.19}$$

then differentiating:

$$\left. \frac{df_1}{d\psi} \right|_{\psi=\psi_x} + O(\varepsilon) = 0 \tag{4.20}$$

Performing the expansion and keeping the coefficients of ε :

$$\begin{aligned}
f_1(\alpha, \psi) & = -\sin \alpha \cos \alpha \sin \psi + \frac{n_o^2 \sin^2 \alpha}{2\sqrt{n_o^2 - \sin^2 \psi}} + \frac{\sqrt{n_o^2 - \sin^2 \psi}}{2} \\
& - \sin^2 \alpha \sqrt{n_o^2 - \sin^2 \psi}
\end{aligned} \tag{4.21}$$

Differentiating:

$$\left(\frac{df_1}{d\psi} \right)_{\psi=\psi_x} = -\sin \alpha \cos \alpha \cos \psi + \frac{n_o^2 \sin^2 \alpha \sin \psi \cos \psi}{2(n_o^2 - \sin^2 \psi)^{1.5}} - \frac{\sin \psi \cos \psi}{2\sqrt{n_o^2 - \sin^2 \psi}}$$

$$\begin{aligned}
& + \frac{\sin^2 \alpha \sin \psi \cos \psi}{\sqrt{n_o^2 - \sin^2 \psi}} \\
& = 0
\end{aligned} \tag{4.22}$$

with error of order $O(\varepsilon)$. This simplifies to:

$$\begin{aligned}
-\sin 2\alpha - \cos 2\alpha \sin \psi \left(\frac{n_o^2}{2(n_o^2 - \sin^2 \psi)^{1.5}} + \frac{1}{\sqrt{n_o^2 - \sin^2 \psi}} \right) &= \sin \psi \left(\frac{-n_o^2}{2(n_o^2 - \sin^2 \psi)^{1.5}} \right) \\
-\sin 2\alpha - \cos 2\alpha \sin \psi \left(\frac{3n_o^2 - 2 \sin^2 \psi}{2(n_o^2 - \sin^2 \psi)^{1.5}} \right) &= \sin \psi \left(\frac{-n_o^2}{2(n_o^2 - \sin^2 \psi)^{1.5}} \right)
\end{aligned} \tag{4.23}$$

equation 4.23 can be rewritten in the form:

$$j \sin(2\alpha) + k \cos(2\alpha) = l \tag{4.24}$$

where:

$$j = -1 \tag{4.25}$$

$$k = -\sin \psi \left(\frac{3n_o^2 - 2 \sin^2 \psi}{2(n_o^2 - \sin^2 \psi)^{1.5}} \right) \tag{4.26}$$

$$l = \sin \psi \left(\frac{-n_o^2}{2(n_o^2 - \sin^2 \psi)^{1.5}} \right) \tag{4.27}$$

Using the trigonometric half-angle formulae:

$$\sin(2\alpha) = \frac{2 \tan(\alpha)}{1 + \tan^2(\alpha)} \tag{4.28}$$

$$\cos(2\alpha) = \frac{1 - \tan^2(\alpha)}{1 + \tan^2(\alpha)} \tag{4.29}$$

equation 4.24 becomes:

$$j \frac{2t}{1+t^2} + k \frac{1-t^2}{1+t^2} = l \quad (4.30)$$

where $t = \tan(\alpha)$. This can be solved as a quadratic in \tan . e.g:

$$(l+k)t^2 - 2jt + (l-k) = 0 \quad (4.31)$$

such that the general quadratic solution looks thus:

$$\tan \alpha = \frac{-2 \pm \sqrt{(2)^2 - 4(l+k)(l-k)}}{2(l+k)} \quad (4.32)$$

$$= \frac{-1 \pm \sqrt{1-l^2+k^2}}{l+k} \quad (4.33)$$

Substituting l and k :

$$\tan \alpha = \frac{-1 \pm \sqrt{1 - \left[\sin \psi \left(\frac{-n_o^2}{2(n_o^2 - \sin^2 \psi)^{1.5}} \right) \right]^2 + \left[\sin \psi \left(\frac{3n_o^2 - 2\sin^2 \psi}{2(n_o^2 - \sin^2 \psi)^{1.5}} \right) \right]^2}}{\left[\sin \psi \left(\frac{-n_o^2}{2(n_o^2 - \sin^2 \psi)^{1.5}} \right) \right] - \left[\sin \psi \left(\frac{3n_o^2 - 2\sin^2 \psi}{2(n_o^2 - \sin^2 \psi)^{1.5}} \right) \right]} \quad (4.34)$$

The negative quadratic solution is discontinuous at $\psi_x = 0$, so choose the positive solution is chosen. Following through, the analytic solution for a planar cell is finally reached as:

$$\alpha = \arctan \left(\frac{\sqrt{1 + \frac{\sin^2 \psi (2n_o^4 - 3n_o^2 \sin^2 \psi + \sin^4 \psi)}{(n_o^2 - \sin^2 \psi)^3}} - 1}{\frac{-\sin \psi (2n_o^2 + \sin^2 \psi)}{(n_o^2 - \sin^2 \psi)^{1.5}}} \right) \quad (4.35)$$

Simplifying this expression:

$$\alpha = \arctan \left(\frac{\sqrt{(n_o^2 - \sin^2 \psi)^3 + \sin^2 \psi (2n_o^4 - 3n_o^2 \sin^2 \psi + \sin^4 \psi)} - (n_o^2 - \sin^2 \psi)^{1.5}}{-\sin \psi (2n_o^2 - \sin^2 \psi)} \right) \quad (4.36)$$

A plot of equation 4.36 as in figure 4.4 shows a limit at $\alpha \approx 20^\circ$ in line with the limit from the law-of-refraction calculations.

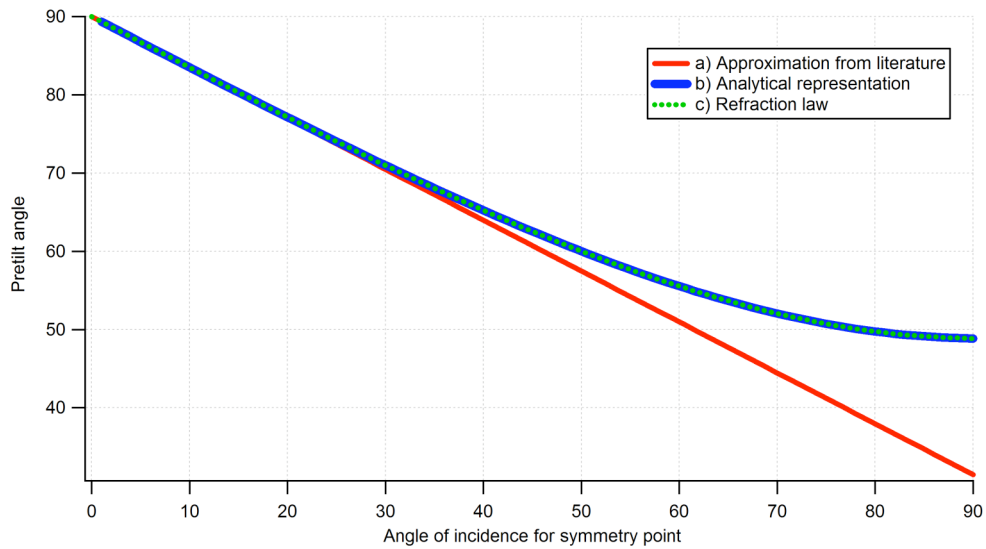


Figure 4.4 - Dependence of pretilt angle α on angle of incidence ψ_x in the case of wavevector close to parallel to the optical axis. $n_e=1.74$ and $n_o=1.52$. a)

Approximation $\alpha = \frac{\psi_x}{n_o}$ from [63] b) Analytical representation from equation 4.37

c) Law-of-refraction calculations from equation 4.5

To extend the range of pretilts which can be calculated, the same methodology can be applied to light refracting along the optical axis by changing the measurement basis to a deviation from the surface normal. This alters the value of n to:

$$n^2 = n_e^2 \cos^2 \alpha + n_o^2 \sin^2 \alpha$$

The quadratic coefficients change such that k becomes positive, resulting in the pretilt angle for propagation along the optical axis:

$$\alpha = 90 - \arctan \left(\frac{\sqrt{(n_o^2 - \sin^2 \psi)^3 + \sin^2 \psi (2n_o^4 - 3n_o^2 \sin^2 \psi + \sin^4 \psi)} - (n_o^2 - \sin^2 \psi)^{1.5}}{\sin \psi (2n_o^2 - 2 \sin^2 \psi)} \right) \quad (4.37)$$

This relationship is shown in figure 4.5.

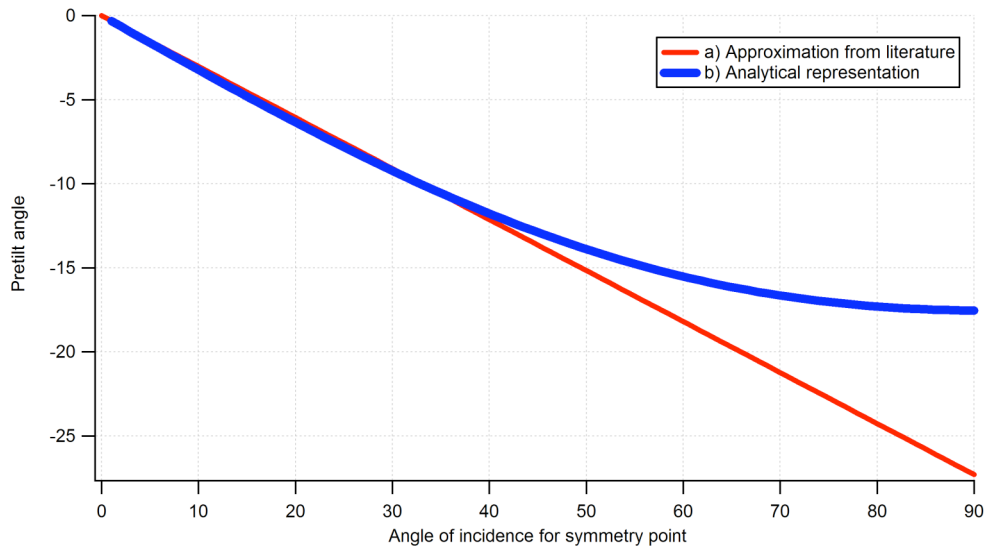


Figure 4.5 - Dependence of pretilt angle α on angle of incidence ψ_x in the case of wavevector close to perpendicular to the optical axis. $n_e=1.74$ and $n_o=1.52$. a)

Approximation $\alpha = \frac{\psi_x}{n_e + n_o}$ from [63] b) Analytical representation from equation

4.36

So how does the range of pretilt angles calculated by this method compare with the other methods presented earlier? The limit on the maximum pretilt angle which can be determined using this method can be found by substituting $\alpha = \pm 90^\circ$ into equations 4.36 and 4.37. The limit is found to be $\approx 17^\circ$ for the planar case and $\approx 20^\circ$ for the homeotropic. It can be seen that even though $n_e - n_o$ is quite large, the solution agrees within 1% of that quoted elsewhere [63] and the exact equation 4.6. Figures 4.4 and 4.5 show this agreement well, but it can be seen that for high angles of incidence ($> 45^\circ$),

this analytical system follows the physical limits in a way that small angle approximations cannot.

4.7 Multiple-Peak Method

The problem with each technique described so far, is that it is reliant on the measurement of a symmetry point ψ_x and is thus experimentally limited by total internal reflection. Gwag et al. [65] presented a technique which removes this limit. It involves measuring the positions of neighbouring peaks in the angular transmission intensity, which are seen even for high pretilt angles (see figure 4.6). This derivation is presented here.

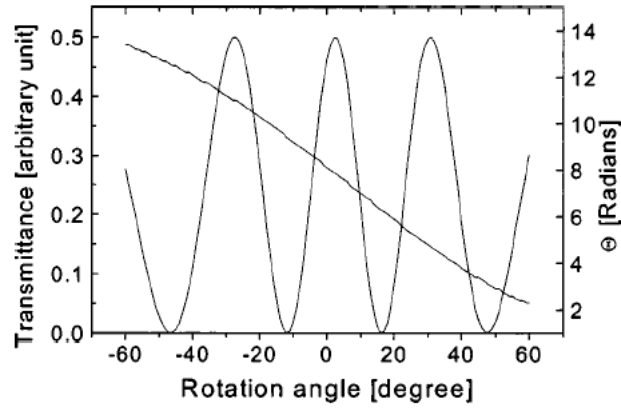


Figure 4.6 - Dependence of the transmittance and retardation upon angle of incidence; ψ_x for high tilt angles where a symmetry point is not seen. [65]

It is known that the transmitted intensity will be zero when the retardation is a multiple of π . ie.: $\phi = \pm n\pi$. Likewise, if the retardation; $\phi = \pi/2 \pm m\pi$, there should be a maximum in the transmission pattern. Equating the equations for retardation;

$$\phi(\psi_1) = \frac{\pi d}{\lambda} f(\alpha, \psi_1) = \pm n\pi \quad (4.38)$$

$$\phi(\psi_2) = \frac{\pi d}{\lambda} f(\alpha, \psi_2) = \pi/2 \pm m\pi \quad (4.39)$$

and dividing equations 4.38 and 4.39:

$$\frac{f(\alpha, \psi_1)}{f(\alpha, \psi_2)} = \frac{\pm n}{\frac{1}{2} \pm m} \quad (4.40)$$

Note that there is no dependence upon wavelength or cell thickness in equation 4.40. If the cell thickness is known then both n and m can be calculated easily. Thus by measuring two angles; ψ_1 and ψ_2 corresponding to maxima and minima in the transmission, α can be calculated from equation 4.40 and substitution of the birefringence function $f(\alpha, \psi)$.

If, however, n and m are not known, α can still be calculated, and herein lies the strength of this method. Take two neighbouring maxima of angular transmission, m and $m+1$. The equation relating these two maxima is:

$$\frac{\pi d}{\lambda} (f(\alpha, \psi_{m+1}) - f(\alpha, \psi_m)) = \pi \quad (4.41)$$

and similarly, for two neighbouring minima:

$$\frac{\pi d}{\lambda} (f(\alpha, \psi_{n+1}) - f(\alpha, \psi_n)) = \pi \quad (4.42)$$

Dividing these two equations:

$$\frac{f(\alpha, \psi_4) - f(\alpha, \psi_3)}{f(\alpha, \psi_2) - f(\alpha, \psi_1)} = 1 \quad (4.43)$$

which does not contain n or m and is thus independent of cell thickness and incident wavelength (except for the wavelength dependence of the refractive indices). The method relies upon solving equation 4.43 for α using four known values of ψ from CRM data. The simplest way to solve this is to do it numerically by plotting equation 4.43 for $\alpha = -90 \dots 90$ and finding the $y=1$ crossing point. Pretilt is then found

numerically using the ratio of the differences between the effective birefringence at 4 incident angles which produce maxima and minima in the angular transmission pattern.

4.8 Evaluating the Multiple Peak Method

On first sight this method seems to offer a solution for calculating the pretilt angles of any cell, since there are no limits on the pretilt angles which can be calculated. Here I present an analysis of this method using sample data to test the procedure computationally. An example graph of equation 4.43 using the data values $\psi_1 = -4^\circ$, $\psi_2 = 5^\circ$, $\psi_3 = 1^\circ$, $\psi_4 = 10^\circ$ as used in [65] has the form:

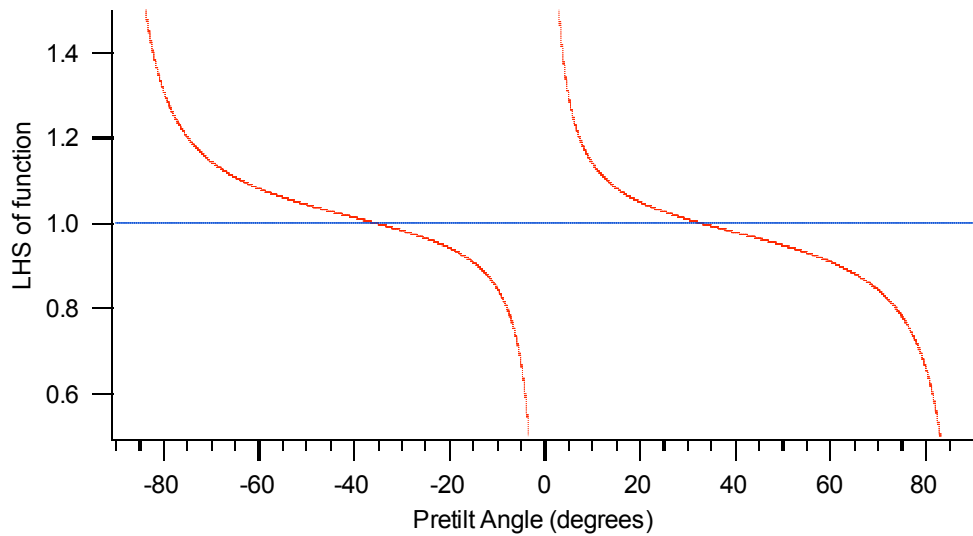


Figure 4.7 – Sample graph to evaluate the multiple peak method using data from reference [65]. The red line indicates the function in eq. 4.43, blue is the $y = 1$ line.

As can be seen, this graph goes to \pm infinity as it asymptotically approaches $\alpha = 0^\circ/90^\circ$. To easily evaluate the value of α for which the equation equals one, one is subtracted from both sides and the absolute value taken:

$$\left| \frac{f(a, \psi_4) - f(a, \psi_3)}{f(a, \psi_2) - f(a, \psi_1)} - 1 \right| = 0 \quad (4.44)$$

Plotting this graphically, something like figure 4.8 is seen. It can be seen now that it is much easier to use a minima finding routine to find the zero crossing points. It is also immediately obvious that for this data, there are two solutions to equation 4.44. the authors of [65] fail to mention this in their presentation of the system. Indeed, two solutions are always found using both simulated and experimental data sources.

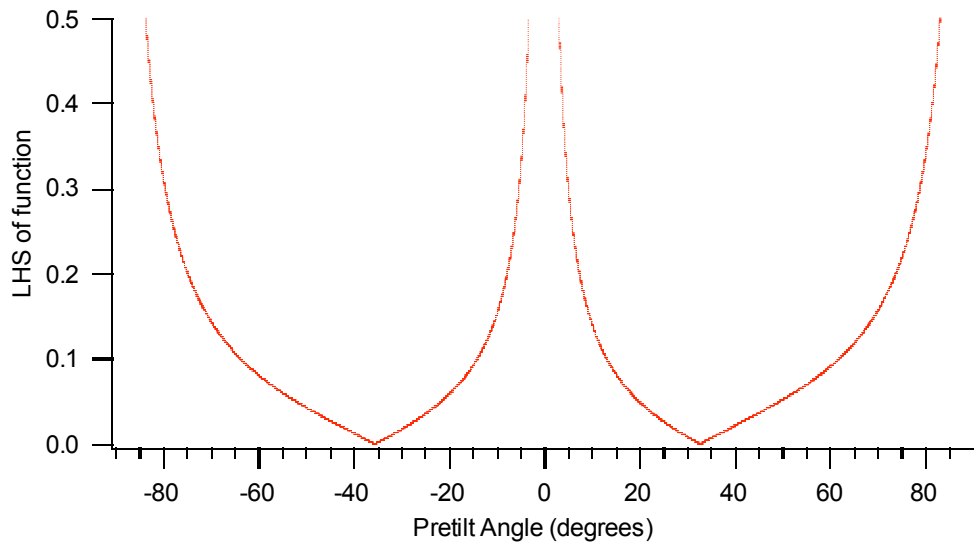


Figure 4.8 – Second sample graph to evaluate the multiple peak method using data from reference [65]. The red line indicates the function in equation 4.44

It therefore appears that some prior knowledge of the director profile of the cell is required to choose between these two solutions. For the sample peak angles, the two solutions are; 32.6314° and -35.6255° . This shows an error of $\sim 2^\circ$ ($\sim 6\%$) with the presented value of $\alpha = 33.4^\circ$.

An attempt to find the correct solution can be made by fitting the two pretilt angles to experimental data using the transmission equation 4.2 and knowing the direction of the incoming beam. Using this procedure on the data provided by the authors in their paper, I fitted the calculated pretilt angle from this data to their transmission pattern. Using the value for psi above and $n_o = 1.4985$, $n_e = 1.627$, $d = 50\mu\text{m}$, $\lambda = 632.8\text{nm}$ for $\alpha = 33.4^\circ$ as in the paper do not reproduce the experimental transmission curve they provide. Figure 4.9 shows the calculated transmission patterns using these parameters for their value of $\alpha = 33.4^\circ$ and a better fit using $\alpha = 31.8^\circ$ or 37.6° . The value of pretilt quoted in [65] is

about 4° out ($\sim 10\%$ error) compared to their experimental results, and I was unable to replicate their calculated pretilt angle.

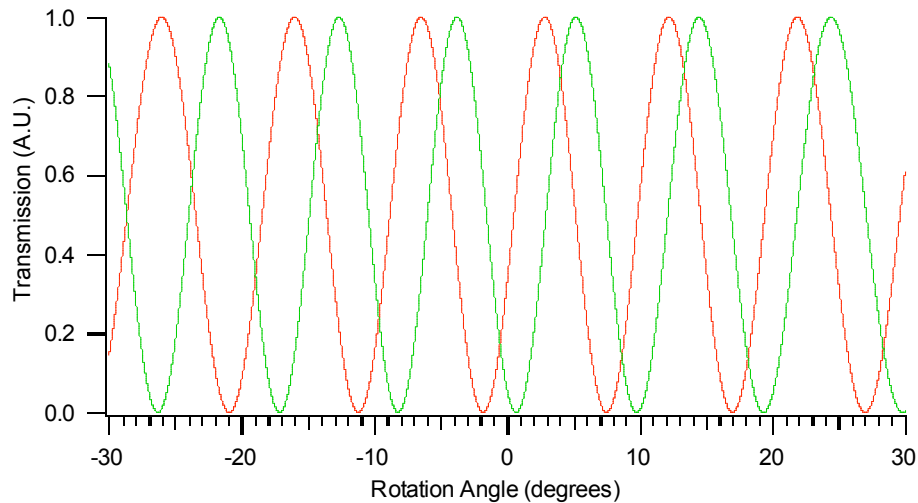


Figure 4.9 – Calculated transmission using equation 4.43 for $\alpha = 33.4^\circ$ (red line) from the paper and $\alpha = 37.6^\circ$ which is a much better fit to the experimental results (green line) in the paper. The transmission curves look very different.

There are two problems with this system:

- Using the author's calculated value of pretilt angle does not result in the transmission pattern they measured experimentally
- Using their method does not return the same pretilt angle that they state.

I can only conclude that this method is either invalid or very sensitive to certain experimental parameters. Subsequent analysis has shown that the system is very sensitive to the value of peak angle extracted from CRM data. Simulations show that altering a single peak by 1° results in up to a 30° change in the calculated pretilt angle which is an unacceptable error. A systematic error of $+1^\circ$ in the value of every peak angle is a little less drastic, but still results in a change to the calculated pretilt of up to 10° , again too high. Another check is to perform these calculations on CRM data rotated about the angle of normal incidence. One should end up with the same magnitude of pretilt angle but this is not seen, the results sometimes being wildly different. Since our experimental results can have up to a 1° error due to the mount backlash, reflection

interference and other factors, these errors are too large to make this method useful for our needs.

4.9 Discussion and Analysis of Each Method

The maximum refracted beam angle is the maximum tilt angle at which the beam can be parallel or perpendicular to the director. Techniques for calculating pretilt which rely on a symmetry point are therefore limited in the maximum pretilt angle which can be determined. Thus, it is impossible to see a symmetry point for a cell with pretilt angle greater than:

$$\alpha = 90 - \theta_c = 90 - \arcsin\left(\frac{n_{air}}{n_{ord} / n_{ext}}\right) \quad (4.44)$$

For the liquid crystal E7 using $n_{air} \approx 1$, $n_o = 1.52$, this limits the range of measurable pretilt angles to $\alpha < 13.6^\circ$ and $\alpha > 48.87^\circ$. Larger limits are apparent in calculations. Using the small-angle approximation ($\sin \psi_x = \psi_x$) in equation 4.7 incurs an error of $< 2\%$ for $\psi_x \ll 20^\circ$. This limits the pretilt angles to $\alpha > 90 - (20^\circ / n_o) \pm 2\%$ which is $\alpha > 74.84^\circ \pm 2\%$ for E7. The limit in the determination of planar pretilt is again limited by the maximum angle of refraction, but a far larger limit arises from the differentiation method and is shown to be $\alpha < 16.3^\circ$ for planar pretilt in E7. This limit is also seen using the analytical representation I have developed. The analytical representation agrees to within 1% of that obtained in reference [63] for $\alpha < 16^\circ$.

It is obvious that a method is needed to measure pretilt of any angle, as there is a range of pretilt angles $13.6^\circ < \alpha < 48.87^\circ$ from the cell normal which cannot be determined from symmetry points. Complex structures such as a hybrid cell with homeotropic and planar alignment surfaces (so that it should have an average 45° tilt) therefore become much more difficult to analyse.

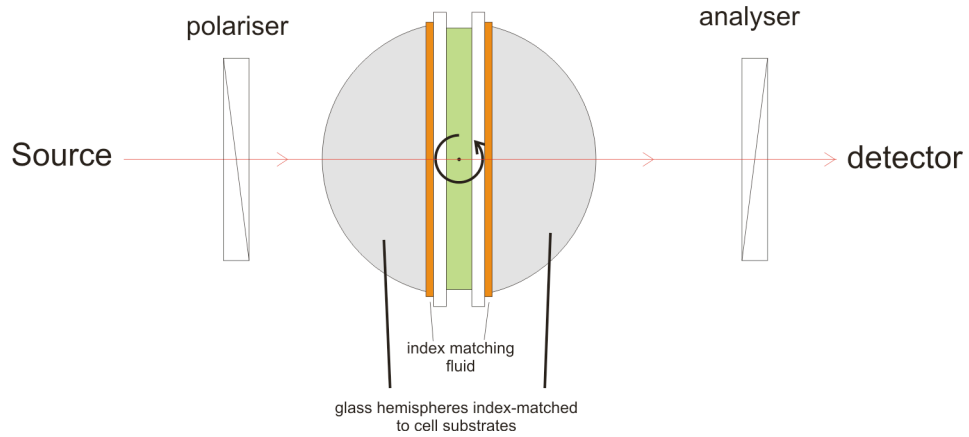


Figure 4.10 – Experiment to remove pretilt measurement limit due to refraction

A proposed solution to this problem is illustrated in fig. 4.10 where index matching fluid and a hemispherical glass block are used to avoid refraction problems. Such a system is however expensive, messy to use and presents technical issues in mounting the cell.

The system proposed by Gwag et al presents a useful alternative as it can calculate pretilt $0^\circ < \alpha < 90^\circ$ and is independent of cell thickness and wavelength. In situations where a symmetry-point cannot be seen, the multiple-peak method can be used and currently provides the only proposed solution which can determine pretilt of any angle from this type of data. Simulations conducted using this method show that it is highly sensitive to the measured incident angles of the transmission peaks. A variation of $\pm 1^\circ$ in transmission peak measurements can result in an inaccuracy of up to 30° in the measured pretilt. This error is unacceptable and as a result, this method is not as useful as it first seems and it becomes worth pursuing other alternatives further.

It is also important to remember that the Fresnel reflection/transmission coefficients will change with the angle of incidence, and a correction for these effects to reduce transmission at higher angles of incidence was incorporated. To some extent these effects can be ignored as only the angle of incidence for which certain peaks appear is needed for calculation of the optical axis direction, not their transmission magnitude.

In summary, for planar or homeotropic angles less than approximately 13° , the approximations: $\alpha = \frac{\psi_x}{n_e + n_o}$ and $\alpha = \frac{\psi_x}{n_o}$ [63] respectively can be used and agree within

1% of the exact solutions in equation 4.6. It is hoped that in the future, using a combination of the analysis methods presented here, an ‘all-in-one’ pretilt device can be developed and which can be used to characterise any new sample.

4.10 Experimental Results

Pretilt angle measurements have been performed for two types of liquid crystal each with two types of polymer layer. The liquid crystals used were E7 and LC1294. These two substances will be used extensively in the beam coupling experiments described in Chapter 5, and knowledge of their pretilt angles is very valuable in setting the parameters for modelling and understanding the TBC process. The alignment polymers used were *Poly-N-vinyl-carbazole* (PVK) and *Polyimide* (PI), the former being the photoconductive layer necessary for beam coupling and the latter a non photo-conducting alignment layer. The amphiphilic surfactant PA-ZLI-3334 was also used to induce homeotropic surface alignment. The samples presented here were constructed with antiparallel rubbed surfaces to create uniform director alignment throughout the sample.

It has been found that for all cells, there is a variation in transmission pattern at different spots in the cell. In most cases of large-domain, well aligned cells (as verified by polarising microscope) the symmetry point in transmission is seen at the same angle of incidence, implying that the director profile is uniform throughout the sample. It can be seen however that the peaks in the transmission pattern appear to move further apart or closer together over successive data sets. There are several factors influencing the angular transmission intensity, including the intrinsic refractive indices of the material, the wavelength of the probe beam and the thickness of the sample. Since the former two should be invariant in this problem, it is assumed that these variations at different spots are due to slight thickness variations. This is a reasonable assertion since the cell is held apart by spacers at each end but may bow in the middle, or the aligning layers could not be of uniform thickness. This is consistent with simulations of the changes introduced by thickness which show that even a thickness variation of $2\mu\text{m}$ can have a significant change to the observed transmission pattern as shown in figure 4.11.

For each sample, a scan is taken twice in the same position (to eliminate any anomalies) and at two or three other positions across the cell. The average pretilt is calculated from these measurements. Even with the same liquid crystal-polymer combination and the same surface treatment there are small variations in pretilt angle between cells. The results presented here are therefore indicative of the alignment found in similar structures and have been expressed as an average value with error corresponding to the maximum difference observed between our samples.

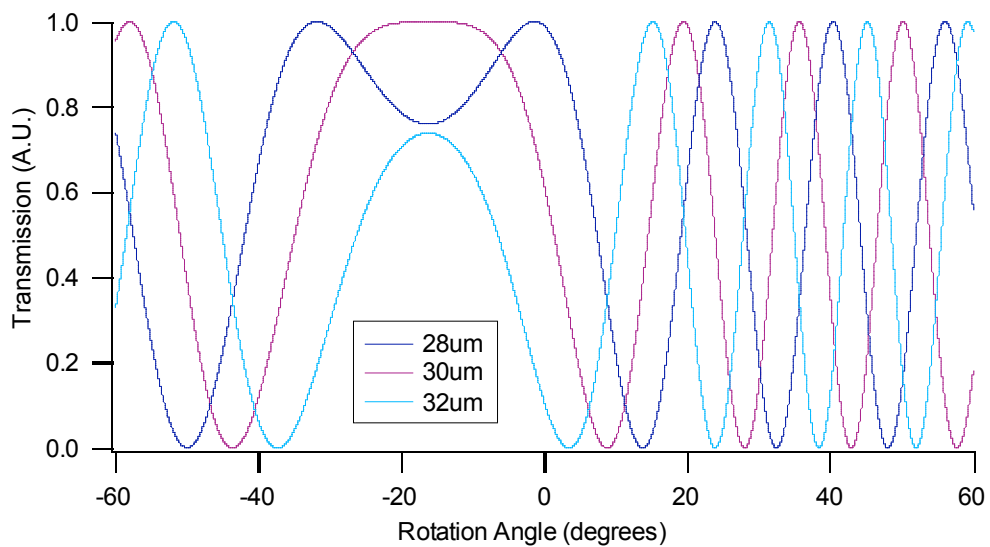


Figure 4.11 - Simulated Transmission curves for different thicknesses of cell using equation 4.2. Purple = 32 μm , dark blue= 30 μm , light blue = 28 μm . Here $\alpha = 4.9^\circ$

Transmission patterns for two E7 and two LC1294 cells, one with a PVK layer and one with a PI layer are shown in figures 4.12 to 4.15. For both liquid crystals with a PVK layer, the symmetry point is centred at normal incidence, giving a measured pretilt of $0^\circ \pm 0.7^\circ$. In contrast, the PI samples exhibit a pretilt of $4^\circ \pm 1^\circ$ for the E7 cells and $5^\circ \pm 0.9^\circ$ for the LC1294 samples. The rubbing strength on PI surfaces can affect the anchoring energy and the magnitude of pretilt, generally due to the varying period and size of the rubbed grooves on the surface. Strong noise is also seen around the point of normal incidence due to interference from interfacial reflections.

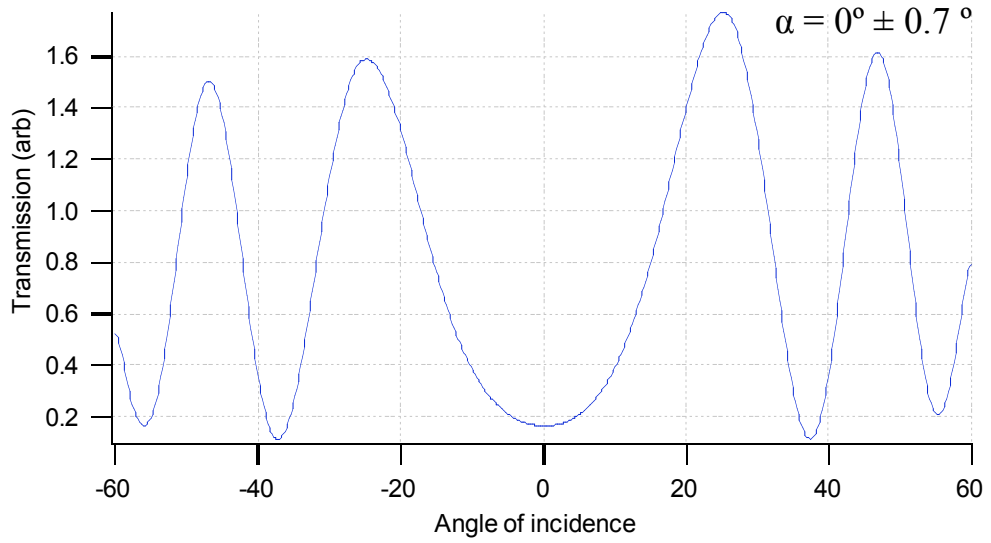


Figure 4.12 – Measured transmission function for the E7-PVK structure. 30 μ m thickness cell

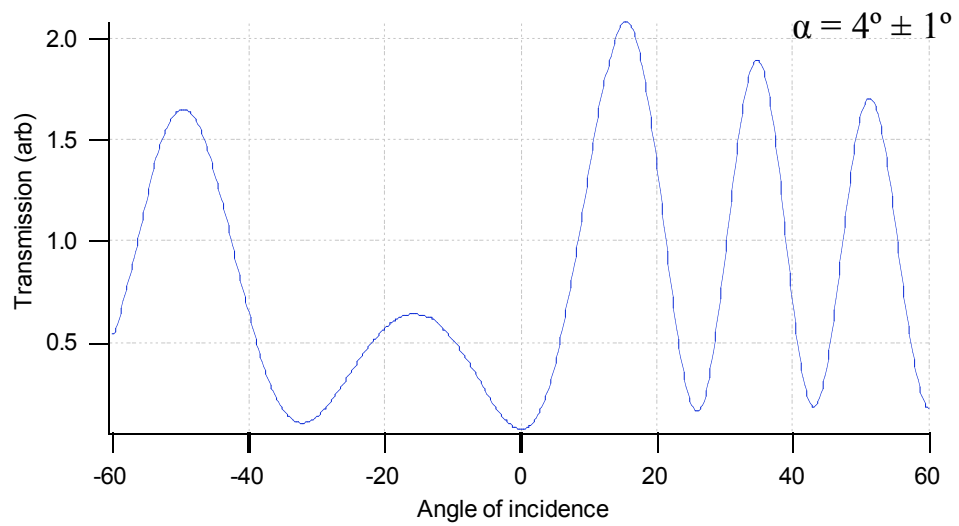


Figure 4.13 - Measured transmission function for the E7-PI structure. 30 μ m thickness cell

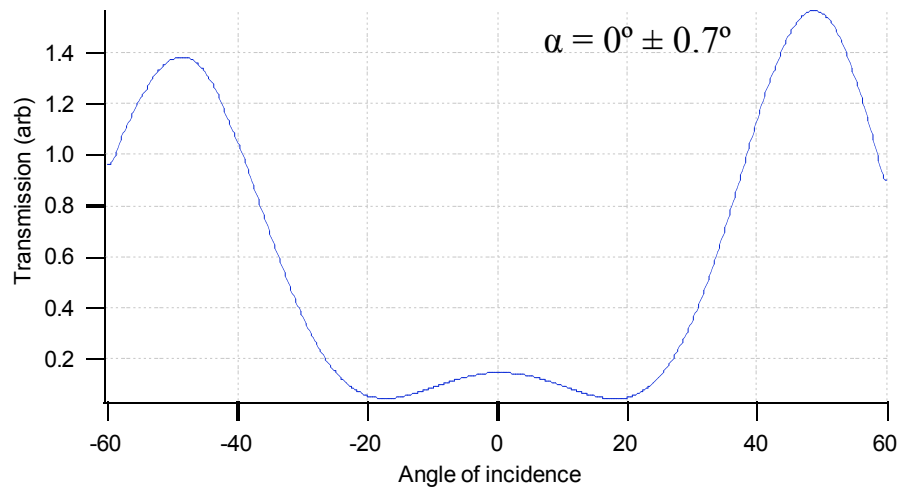


Figure 4.14 - Measured transmission function for the LC1294-PVK structure.
10 μ m thickness cell

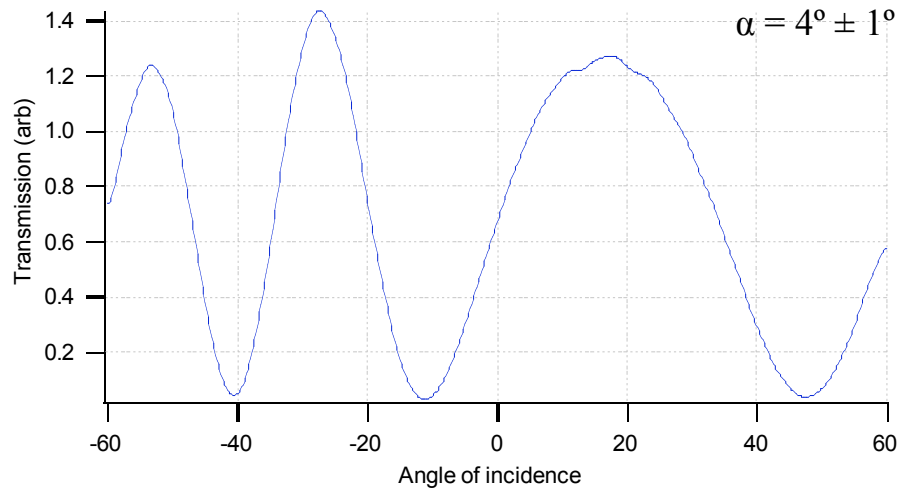


Figure 4.15 - Measured transmission function for the LC1294-PI structure

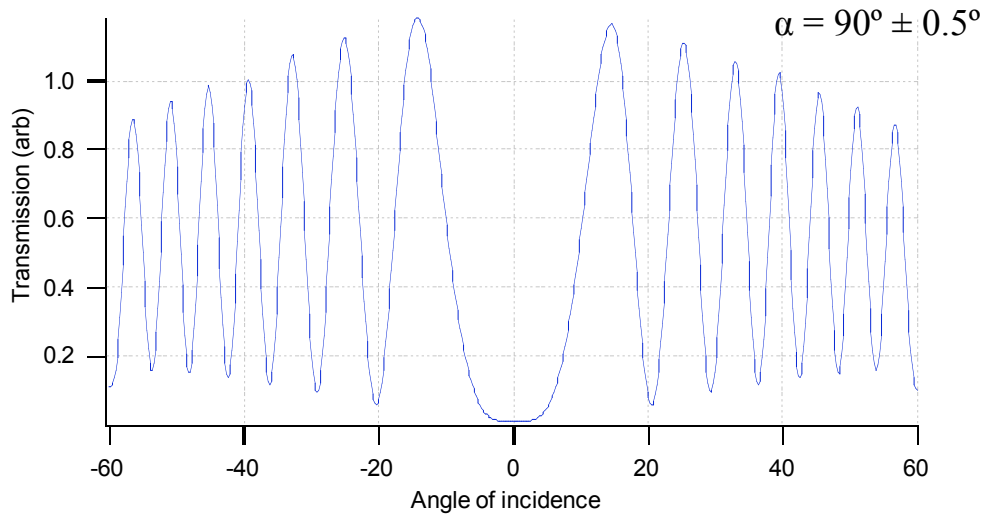


Figure 4.16 - Measured transmission function for the E7-homeotropic structure. 30 μ m thickness cell

Figure 4.16 shows a sample constructed with the homeotropic surfactant. Again there is virtually no pretilt, the angle made with the surfaces being 90°.

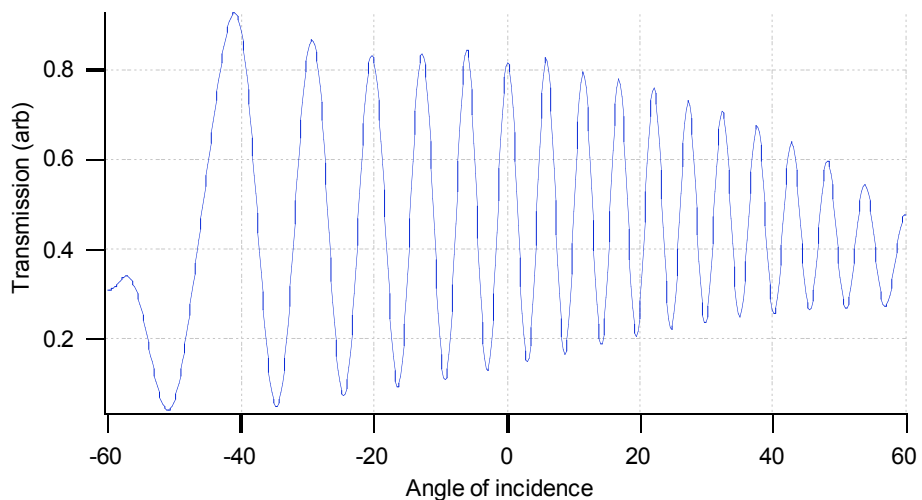


Figure 4.17 - Measured transmission function for the E7- hybrid structure. 30 μ m thickness cell

Figure 4.17 illustrates a sample constructed with PI on one surface and the homeotropic surfactant on the other to create a cell in which the director is not uniform and the molecules bend from 4° on one surface to 90° from the other. Since the CRM experiment averages the birefringence through thickness, providing the anchoring strengths of both surfaces are equal such a sample will look as if its director is at 45° to

the surface. In practice, the anchoring strengths of both surfaces are likely to be different. As can be seen clearly from the figure, there is no symmetry point seen, as the incident light cannot refract along the optical axis. Such a cell would therefore be a candidate for the multiple-peak method suggested in Gwag et. al. [65].

4.11 Magnetic Null Experiments

The crystal rotation method is just one way of measuring the average molecular orientation in a liquid crystal cell. In addition to this, the Magnetic Null method was evaluated to see whether it could provide a more accurate measure of pretilt or allow the determination of larger pretilt angles.

The principle of this method is fairly simple. The cell is placed between two poles of a magnet and rotated whilst observing how some physical property such as the capacitance, or as in our case, the optical retardation varies with field strength. The idea is that the magnetic field distorts the LC and thus the measured property, but at one particular angle, it aligns with the direction of the molecules and changing field strength does not change the measured value. If the cell is not completely homogeneous, then it might not be possible to find a point which is completely independent of field strength, and in this case we can look for the angle corresponding to a minimal change in retardation with field strength. This will give an effective average value of molecular orientation in the cell.

The experimental setup used to test this system is shown in figure 4.18. The cell is mounted such that the rotation axis is perpendicular to the magnetic field and the easy axis. The cell is placed between crossed polarisers and within the magnetic field and a laser beam is passed through. The transmission intensity is measured by a photodetector. The rotation arm was marked every degree to show angle of rotation from the starting point. The cell is initially set up with the x-axis parallel to the magnetic field and this is calibrated as the zero rotation angle. This provided a rotation angle measurement with an accuracy of 2° . Transmission vs. field strength data were then taken for a series of rotation angles.

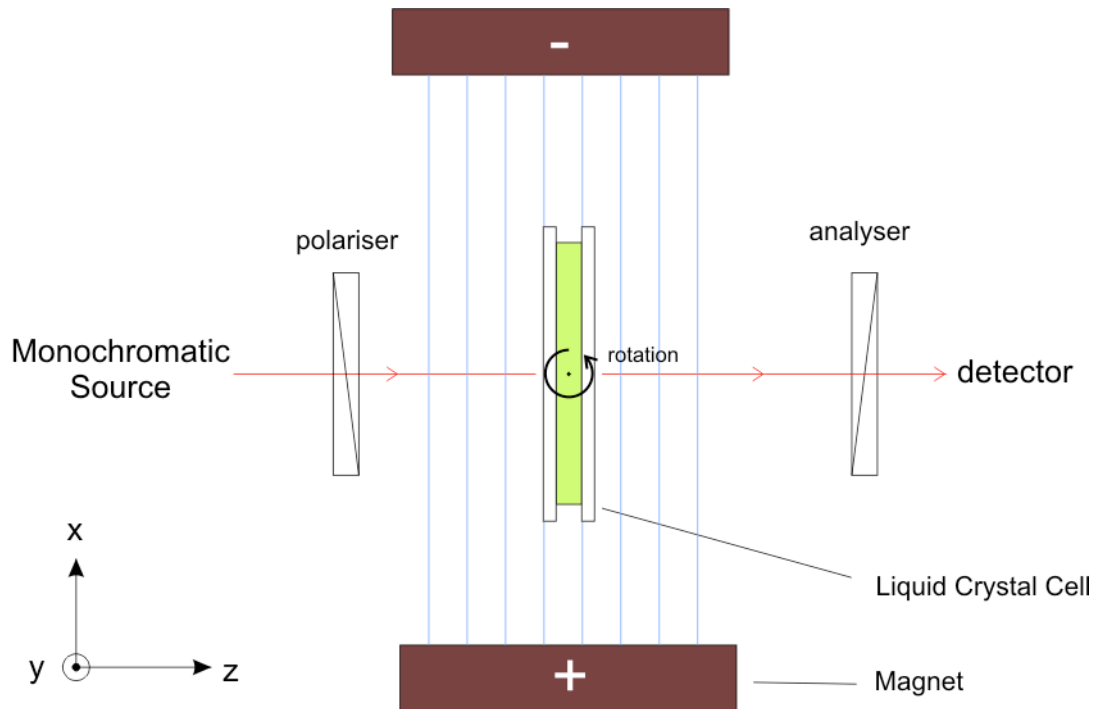
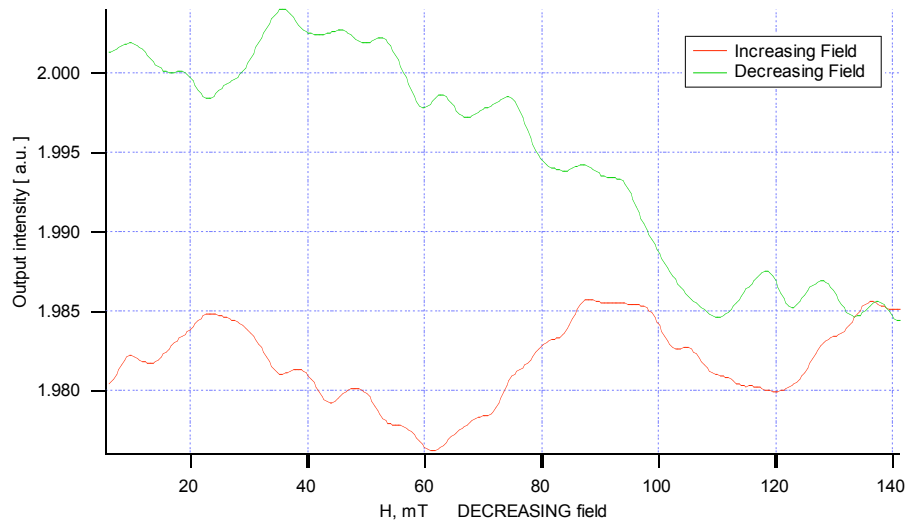
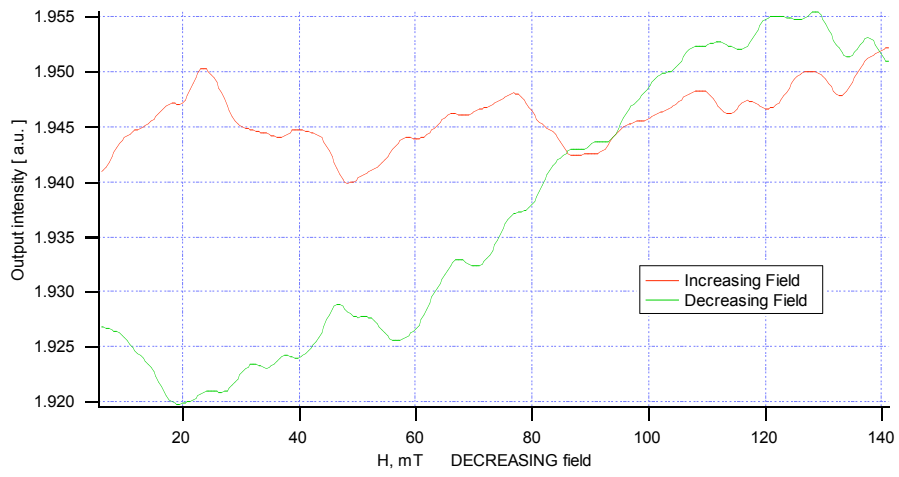


Figure 4.18 – Experimental setup for magnetic null experiments

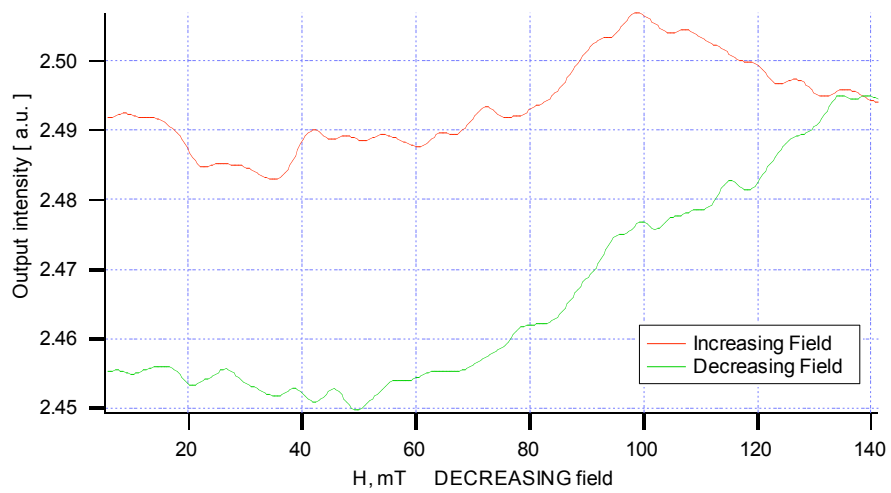
Magnetic null experiments were performed on some test cells to assess the suitability of the method for measuring large pretilt angles. It was discovered that the accuracy of this experimental setup was insufficient to adequately measure pretilt angle with the precision of the CRM. Sample data for Cell 2 (PI surfaces filled with E7) can be seen in figure 4.19 a-d. This figure shows the optical transmission through the LC as the applied magnetic field is increased (red line) and then decreased (green line). I performed this experiment for a number of different rotation angles and deduced the direction of average orientation corresponding to the angle for which the optical transmission difference for increasing and decreasing field is the largest.



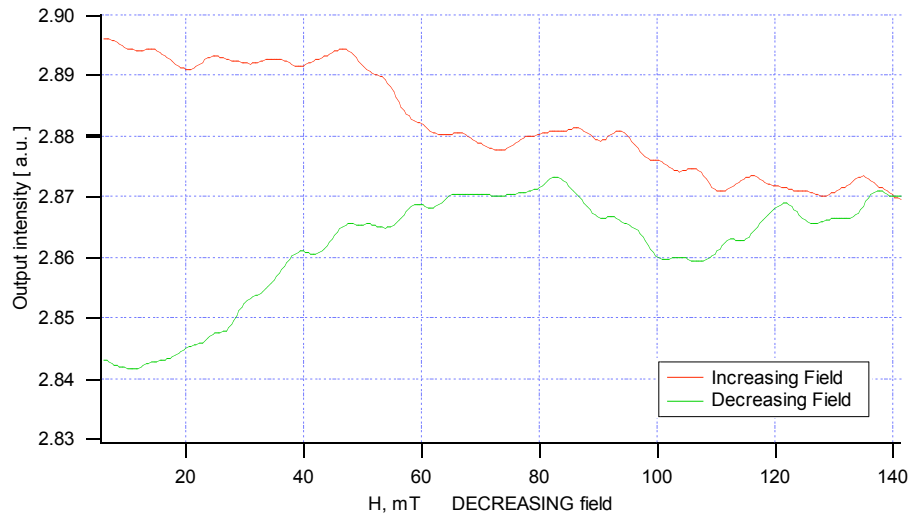
a) PVK sample rotated by 0 degrees



b) PVK sample rotated by 1 degree



c) PVK sample rotated by 2 degrees



d) PVK sample rotated by 3 degrees

Figure 4.19 – Example magnetic null data sets showing the change in transmission variance with angle.

As can be seen from this sample data, there is definitely a decrease in the transmission with field towards zero degree rotation. Although this is inconsistent with the expected pretilt value for a PI cell (between 3-15°), it matches the pretilt of $0.1^\circ \pm 0.06^\circ$ established for this cell using the crystal rotation method. However, for other test cells, similar results showed that the signal noise was too high to accurately pick the smallest transmission difference with increasing field. Every effort was made to cut out optical noise via external light sources. The noise source could be due to turbulence or scattering in the LC cell or of vibration of the mount. These conditions could be improved by using a higher intensity laser beam to reduce background effects. Regardless, without significant time and equipment investment in this experiment, the data are not conclusive and cannot be used to verify the CRM results.

4.12 Ageing and Damage Effects

As previously described, pretilt measurements can be used to monitor director profiles in uniform samples. Measurements of pretilt angle have been made on both E7 and LC1294 samples constructed over 1 year ago to see if they differ from the newly constructed cells.

Measurements have also been performed on samples of both liquid crystals exhibiting optical ‘damage’ effects. Such samples have been subjected to large electric fields (greater than 20 Volts) whilst under illumination from a 543.5nm green laser operating at 5mW maximum output. An example of this damage can be seen in figure 4.20.

E7 is a well known LC material and is known to be stable for many years. This is confirmed by our observations, in which all the measured pretilt angles for 1 year old cells fall within the range observed for new cells, and I can conclude that the cells tested here are also long-lasting.

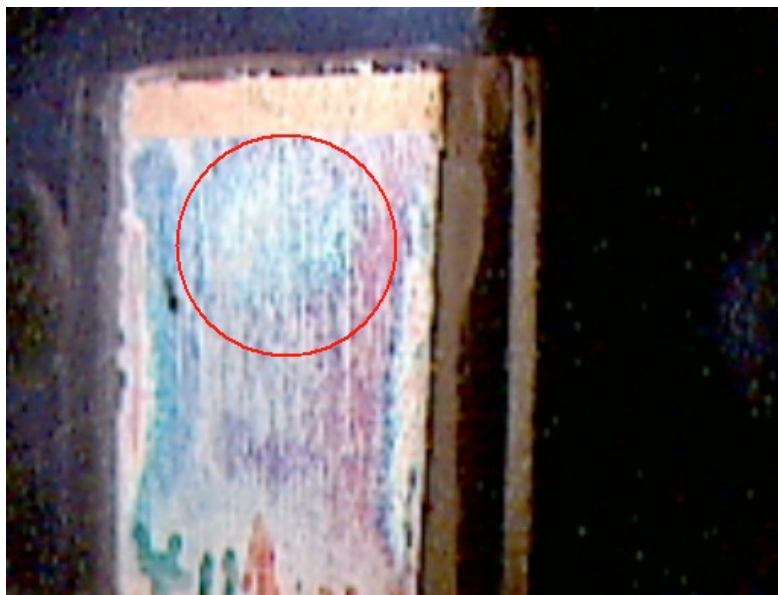


Figure 4.20 – Polarising microscope image of a damage spot caused by a 5mW beam and 20V applied DC. The large red circle shows the damaged region (slightly bluer area). Two other damage spots can also be seen towards the bottom of the picture leftover from an earlier experiment.

Attempts to create optical damage in E7 were unsuccessful. Subjecting the sample to applied voltages of 0-50V and up to 5mW of incident optical laser power created no observable long-term effects under either a polarising microscope or pretilt measurements once removed.

LC1294 in contrast is a newer experimental mixture and little is known of the stability lifetime of its director profile and surface alignment. This LC was synthesised recently, and is designed to have a very large optical anisotropy, making it an important

candidate for beam coupling experiments. Experiments on year-old LC1294 cells indicated that like E7, the pretilt and hence molecular alignment fell within the range established for new cells of the same type. I can hence reason that these cells also have an alignment lifetime on the scale of years.

However, unlike E7, LC1294 cells showed optical deformation when subjected to high field ($>20\text{V}$) and under illumination from the 5mW green laser. Preliminary experiments show a definite change in the director profile within the damaged region, most likely due to a modification of the surface via a photo-induced alignment process or residual surface charge. The damaged area is approximately equal to the beam spot size, so in any subsequent investigation of the director profile, the probe beam must be focussed to a point smaller than the damage spot to avoid measuring defects occurring at the edge of the damaged region. I have as yet been unable to determine the director structure within these regions due to the non-standard transmission patterns that have been seen (see figure 4.21). Possible reasons for this are that the alignment has become random or has split into domains and is not uniform across the probe beam cross section or the cell thickness. Beam diameter is approximately half that of the spot size, so it is unlikely edge defects are being observed, although this needs further investigation to completely rule out.

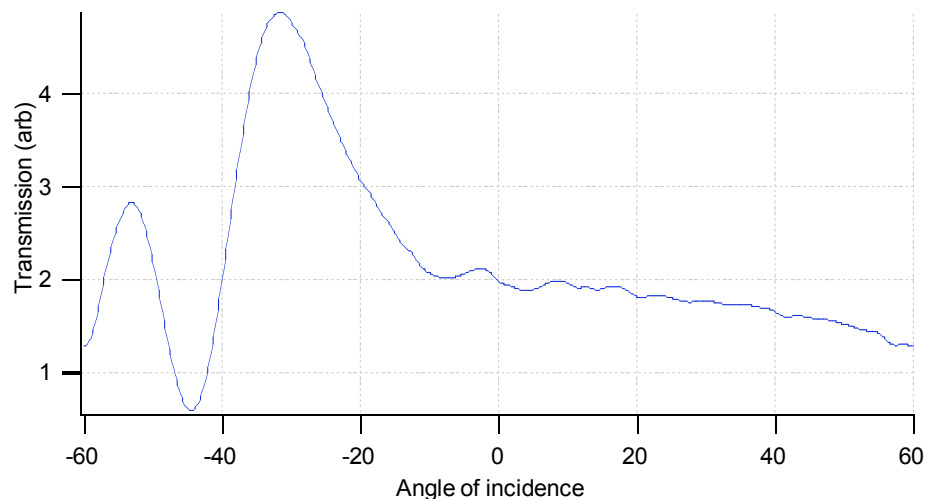


Figure 4.21 – Transmission patterns from damaged areas. From this data it seems unlikely that there is a uniformly oriented structure in the damaged region

I can therefore conclude that the alignment of LC1294 is not stable under extreme conditions and this must be taken into account when assessing its usefulness as a candidate for photorefractive applications. This material is attractive because it offers high contrast index gratings when selectively reoriented, but its susceptibility to optical and applied field effects are undesirable for beam coupling applications. There has however, been some interest expressed in using these features to write patterned and controllable waveguiding channels into the LC-polymer interface. This is not possible with the traditional LC materials such as E7 and 5CB.

4.13 Summary

It was found that measuring pretilt angle gave a good indication of director alignment in uniform (non-periodic) cells. I developed a computer controlled apparatus to measure crossed-polarised transmission versus angle for any standard cell, and calculate the pretilt angle using different algorithms. Existing work did not provide explicit links between CRM data and pretilt angle and was limited in calculable pretilt angle range. I investigated a derivation for the calculation of pretilt angle to try to and remove these limits. Unfortunately it was found that an optical setup is intrinsically limited by total reflection effects. Extensive analysis of a proposed method for measuring any pretilt angle using CRM data could not be reconciled with the author's published data or my own.

I presented results of pretilt angle calculations for two types of liquid crystal commonly used in photorefractive experiments, and crucially observed damage and memory effects when using LC1294 with high (>20V) voltages. Unfortunately, this makes this novel material unsuitable for beam coupling, but makes it useful for applications requiring some kind of patterned electrodes.

The results obtained here have provided a key understanding of the two LC materials involved in SIPRE experiments, and also provided the basis for some analysis tools which may be extendable to periodic director configurations.

Chapter 5 – Periodic Modulation of Director Profiles

Liquid crystals offer many advantages over crystals as photorefractive materials, the major two being that they offer significant orientational enhancement and gain even under weak applied fields and are much less expensive. The surface induced photorefractive effect (SIPRE) has been exploited to achieve high gain two beam coupling using simple, cheap cells with specific liquid crystal-polymer combinations. However, the underlying physical mechanisms behind this effect are not fully identified at this point, and further investigation is needed to better understand them. Such investigation is not only relevant for exploiting photorefractive polymer-liquid crystal structures in applications such as spatial light modulators or light valves, but is also relevant and important to the area of surface and interface effects between polymers and liquid crystals.

In this chapter I will discuss initial observations of the surface induced photorefractive effect in the cells fabricated in our lab, and the proposed theory to explain the observed optical response. I will then detail a mathematical model that has been developed and show some initial simulations performed using this model to predict the electric field, director profile and resultant refractive indices within cells of various configurations. In particular, my aim was to develop these profiles for the case of periodically varying (in space) electric field applied to the surface and validate and refine them via comparison with experimental data.

5.1 Periodic Modulation of Director Profiles

Two beam coupling can be observed in liquid crystal cells, such as for example, those that include photoconductive alignment layers, as described in Chapter 3. However, beam coupling gain can only be observed for certain combinations of liquid crystal and alignment layers and appears to be highly dependant on experimental geometry. Certain polymer layers such as PVK have been shown to produce high beam coupling gain with

E7 but not with other liquid crystals. Similarly E7 will not exhibit beam coupling with all alignment layers. It has been proposed that surface effects at the LC-polymer interface play a much larger role than was previously thought. This is the surface-induced-photorefractive-effect [45]. A model has been proposed to explain this mechanism which revolves around mobile charges creating a screening layer and photo-induced discharge of this layer (see section 3.5).

In my investigation of two-beam coupling, I focussed on two liquid crystals; the well known commercial mixture E7 and a new novel liquid crystal mixture LC 1294, manufactured by a group in Warsaw [66]. This new experimental liquid crystal was synthesised to offer higher birefringence than regular LCs and therefore makes it attractive for beam-coupling and diffraction efficiency experiments. Refractive index and birefringence parameters of this novel LC are presented in table 5.1, and for E7 in table 5.2

a) Optical properties at 20°C

Wavelength λ (nm)	n_{\parallel}	n_{\perp}	Δn
480	1.8204	1.4974	0.3230
589	1.8130	1.5010	0.3120
632.8	1.8081	1.5040	0.3041

b) Optical properties at 60°C

Wavelength λ (nm)	n_{\parallel}	n_{\perp}	Δn
480	1.7877	1.4984	0.2893
589	1.7817	1.5011	0.2806
632.8	1.7776	1.5022	0.2754

Table 5.1 – Refractive index and birefringence of LC1294 at two different temperatures

Wavelength λ (nm)	n_{\parallel}	n_{\perp}	Δn
589	1.7462	1.5216	0.2246

Table 5.2 – Refractive index and birefringence of E7 at 20°C. [67]

These cells had a rubbed PVK:C₆₀ layer on one substrate and rubbed polyimide on the other substrate to give an approximately uniform planar alignment. The pretilt on the PI surfaces will induce a slight splay deformation into this orientation.

The details of two-beam coupling interaction and experiments were described in detail in chapter 3. Figure 5.1 presents the schematic diagram of the set-up I used for measuring gain and its dependence on applied voltage.

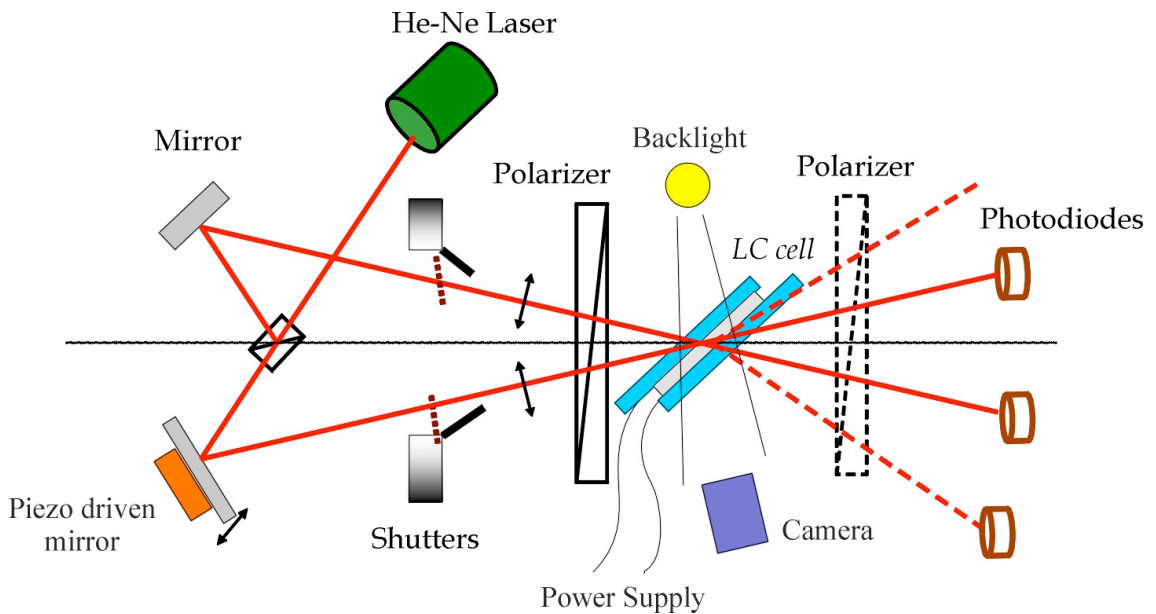


Figure 5.1 – Experimental apparatus for gain vs. voltage experiments

A liquid crystal cell was mounted on a rotation stage and could be precisely turned around the vertical axis (perpendicular to the plane containing the incident beams) at the point of intersection with the incident beams. The cell was arranged so its photosensitive substrate (with PVK:C₆₀) was the one onto which light was incident first.

Data acquisition software (Wavemetrics IGOR) was used to control the operation of electric shutters that blocked or unblocked the beams, as well as cell rotation and the

application of electric field. In this way, two-beam coupling gain dependence on several experimental parameters, such as DC field magnitude or the angle of cell tilt could be measured with a high degree of accuracy.

The two incident beams ($\lambda=543\text{nm}$) that formed the interference pattern on the cell were p-polarized in the plane of incidence. Their intensities were approximately the same and equal to $400 \mu\text{W}/\text{cm}^2$, in order to keep their incident intensity ratio equal to one. The interference pattern incident on the liquid crystal cells had a fringe spacing of $15\mu\text{m}$. The intensities of transmitted beams and of first order diffracted beams were measured on photodiodes and data stored on a computer.

In earlier work the optimum conditions for cell rotation - the so-called cell tilt, which is the angle between the normal to the cell surface and the bisector of the angle between incident beams - to observe high gain was established. Gain was observed in the ‘probe’ beam, being the beam with the largest angle of incidence from the cell normal. The optimum value of the cell tilt was found to be approximately equal to 30° . Hence, for the experimental results presented here, I kept the cell tilt constant and equal to 30° .

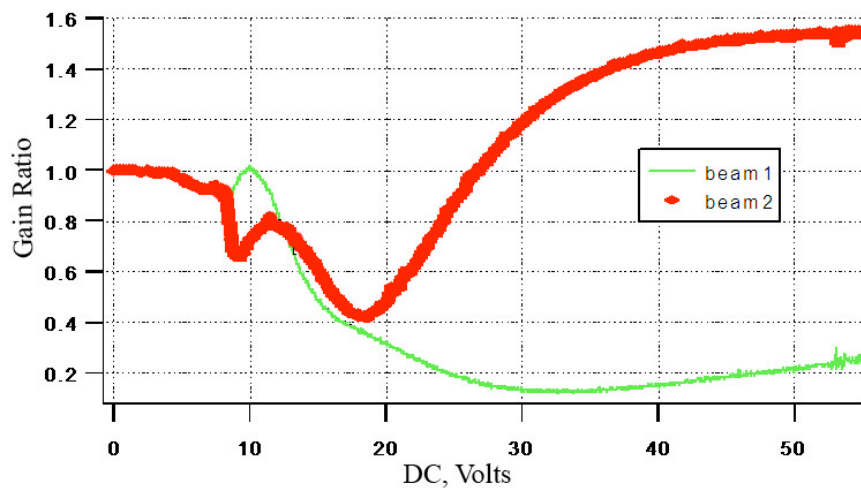


Figure 5.2 - Gain ratio; G versus applied DC electric field for an E7-PVK:C₆₀ cell. Cell thickness was $30\mu\text{m}$ and grating spacing $\Lambda=15\mu\text{m}$. Between 8 and 25 volts, both ratios are less than one. This is most likely due to scattering by the turbid crystal or by diffraction into higher Raman-Nath orders due to a small $\pi/2$ phase shift region.

Figure 5.2 presents the results of optimum, highest two-beam coupling gain ratios (G) for E7 measured as a function of applied DC field. It shows the maximum beam-coupling gain measured in the E7 cell. This was found to have been around the 1.55 mark. The cell was $30\mu\text{m}$ and the optimum grating spacing (used for this measurement) for high gain was $15\mu\text{m}$.

The best results for LC1294 were in thinner cells, $7\mu\text{m}$ thick and $3.5\mu\text{m}$ grating spacing. The optimum grating spacings for the E7 and LC1294 cells were both different, but the ratio of thickness to grating spacing was 2:1 in both cases. Figure 5.3 presents the data on the highest two-beam coupling measured in such a cell.

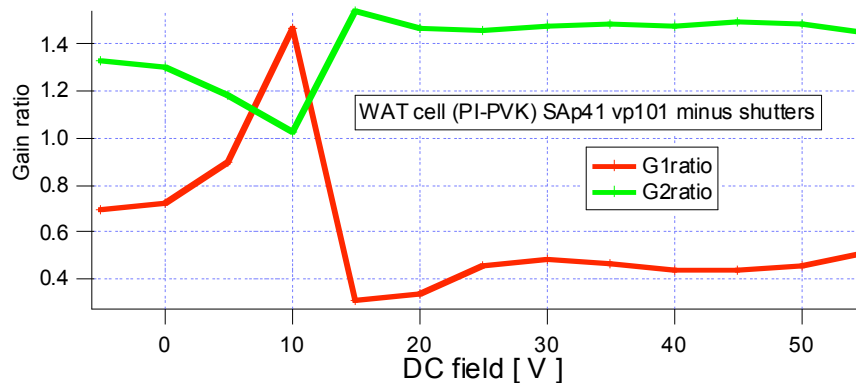


Figure 5.3 - Gain ratio; G versus applied DC electric field for a LC1294-PVK:C₆₀ cell.

Two-beam coupling gain showed similar dependence on applied DC field as observed for E7 and with the maximum gain ratio also comparable ($G=1.5$). As the LC 1294 cell thickness was over four times smaller than the one used for E7, it is clear that high birefringence of LC 1294 indeed contributed to enhanced gain. However, when comparing the two figures (5.2 and 5.3), it is clear that gain in LC 1294 does not show the same smooth dependence on DC field as measured for E7. Indeed, this result is indicative of several issues encountered with LC 1294. The attempts to fabricate good quality, stable and thicker ($30\mu\text{m}$) cells with this liquid crystal were not successful.

So, while the optical efficiency of LC1294 was similar to E7, and on top of this, it exhibited ‘memory effects’ and stability problems as described in section 4.12. These memory effects were only generated under the conditions of illumination and large

applied field ($>20\text{V}$). They manifested as a ‘burned-in’ image of the TBC grating at the LC/surface interface and were present over a time period of at least several months. The quality of the memory-image also degraded over time, making the cell unstable for further beam-coupling.

It could be suggested that such memory effects were due to some modification at the LC-photoconducting layer interface, for example, charge modification or photo-alignment. Such effects are seen in identical cells with PVK:C₆₀ on both surfaces and not in cells with PI on both surfaces. This implies the effects to be due to the PVK-LC interface. In this case, these earlier beam coupling experiments will have acted as evidence for dynamic pattern writing at the surface interface between LC1294 and a photoconducting polymer layer.

This, along with the need for understanding the SIPRE, prompted further work into understanding the interactions at LC-photoconducting layer interfaces. While, in principle, it was possible to carry out extensive experimental tests to find a particular combination of cell and liquid crystal parameters and geometry to achieve high two-beam coupling gain, there was no guarantee for their long term reproducibility and stability. It was much more critical to investigate in detail the nature and key mechanisms behind reorientation gratings in liquid crystals driven by surface effects. As described in chapter 3, beam coupling is only observed in certain experimental geometries and a better knowledge of the interaction process would also allow one to design better liquid crystal mixtures or experimental setups to optimise beam-coupling parameters such as the gain.

As discussed earlier, a considerable amount of beam coupling and diffraction efficiency data has been gathered on the performance of these SIPRE systems, but these tell us very little about the actual processes going on. Currently, it is very difficult to predict the optimum experimental geometry or LC mixtures for specific applications prior to testing. Hence validating the mechanism proposed for the SIPRE and described in chapter 3 has proved more difficult than expected. Understanding these processes became a priority for my further work on this topic. Indeed, this was the motivation for the rest of my work and in particular investigating the director profiles formed during

the process of the SIPRE, with the intention of being able to predict the optimum material and experimental parameters.

5.2 Experimental transmission profiles

Initial experiments took the form of observing the grating through a polarising microscope with a second white backlight source as shown in figure 5.3 and in more detail in figure 5.4. In this experiment a grating was created by crossing two laser beams within an E7-PVK:C₆₀ cell to create an interference pattern and then applying a field of around 10V.

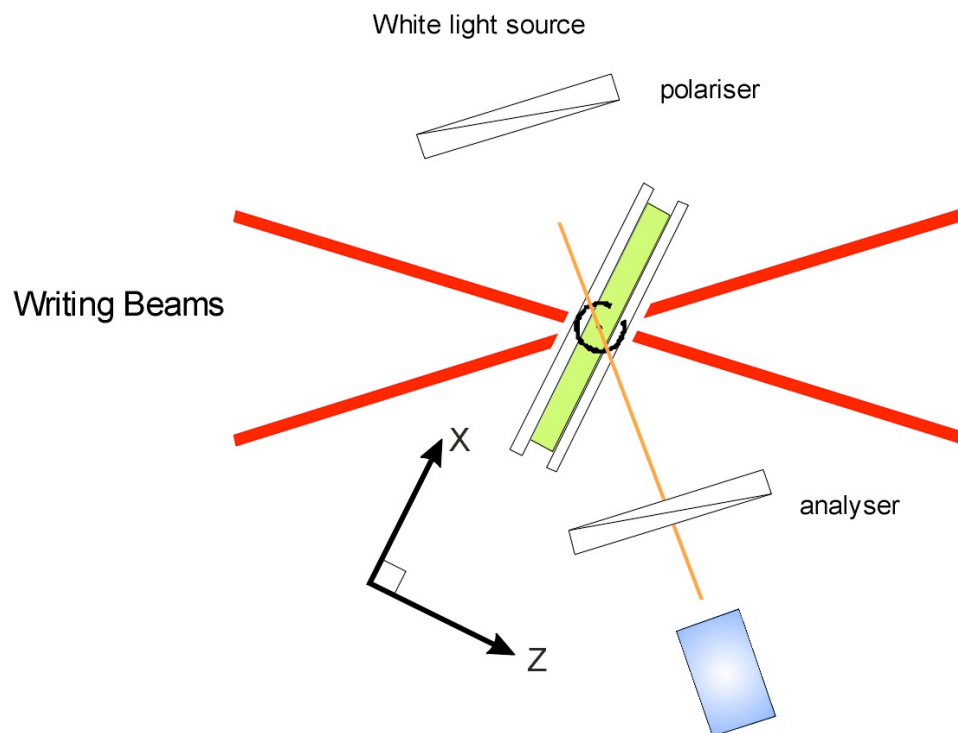


Figure 5.4 – Experimental setup for observing grating formation.

A small webcam was positioned to the side of the optical setup, pointed at a lightbox (tungsten bulb) illuminating from the opposite side of the cell. Calculations using the angles of incidence of the two beams predicted a grating spacing of approximately 100 μ m. The result of this experiment is shown in figure 5.5 and after compensating for the viewing angle, a fringe pattern with a grating spacing of around 100 μ m is indeed seen. A 100 μ m grating was chosen for this experiment because it was relatively quick to create a grating of this order of spacing than lesser sized gratings, and because of the

limited resolution of the optics attached to the camera. It is expected that these observations could be extrapolated down to smaller grating spacings such as those used for the typical beam coupling experiments described earlier, as long as the ratio of grating spacing to cell thickness remains constant.

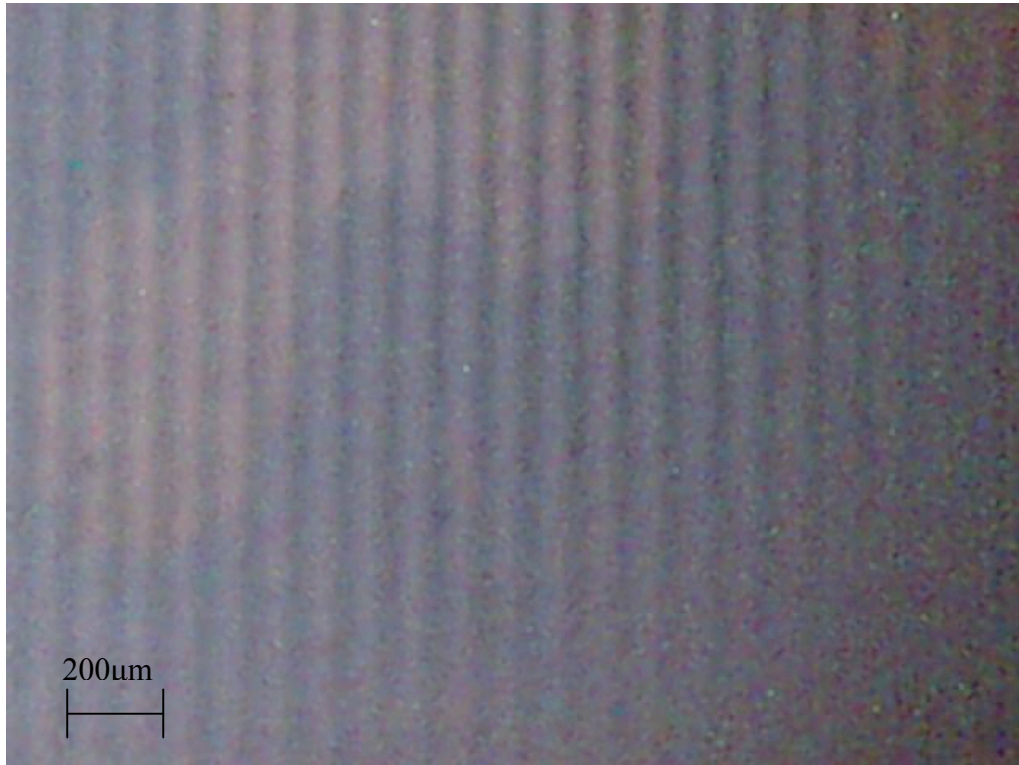


Figure 5.5 – Reorientation grating viewed through a polarising microscope (along the x-axis)

The camera exhibited a large amount of noise at low light levels and the automatic contrast made accurate grating size measurement impossible. High intensity light cannot be used to observe the LC, as this will affect the reorientation. Since the contrast and noise in these images is quite poor, mainly due to the low intensity of the background white light source, this was replaced with a brighter green LED (a different wavelength to the writing laser) to improve image contrast which was partly successful. However, there was still some level of noise/scattering in the dark regions (see fig 5.6). It is also worth adding that the quality and contrast of the images taken deteriorates when they are presented on paper.



Figure 5.6 - Polarising microscope image of a grating back-illuminated by a green LED and under applied voltage of 25V. Contrast is still bad and there is a lot of image noise.

A second, high brightness white LED was then used which improved the images and allowed much easier observation of the grating formation. Using this system it was possible to capture video footage of the grating formation. Some of these frames are shown in fig 5.7. Extracting cross-sectional line profile information from these images and using a calibration image of known size, the grating spacing for different applied field strengths can be calculated. Figure 5.8 shows cross-sectional line profile data extracted from the video and image data captured using this system.

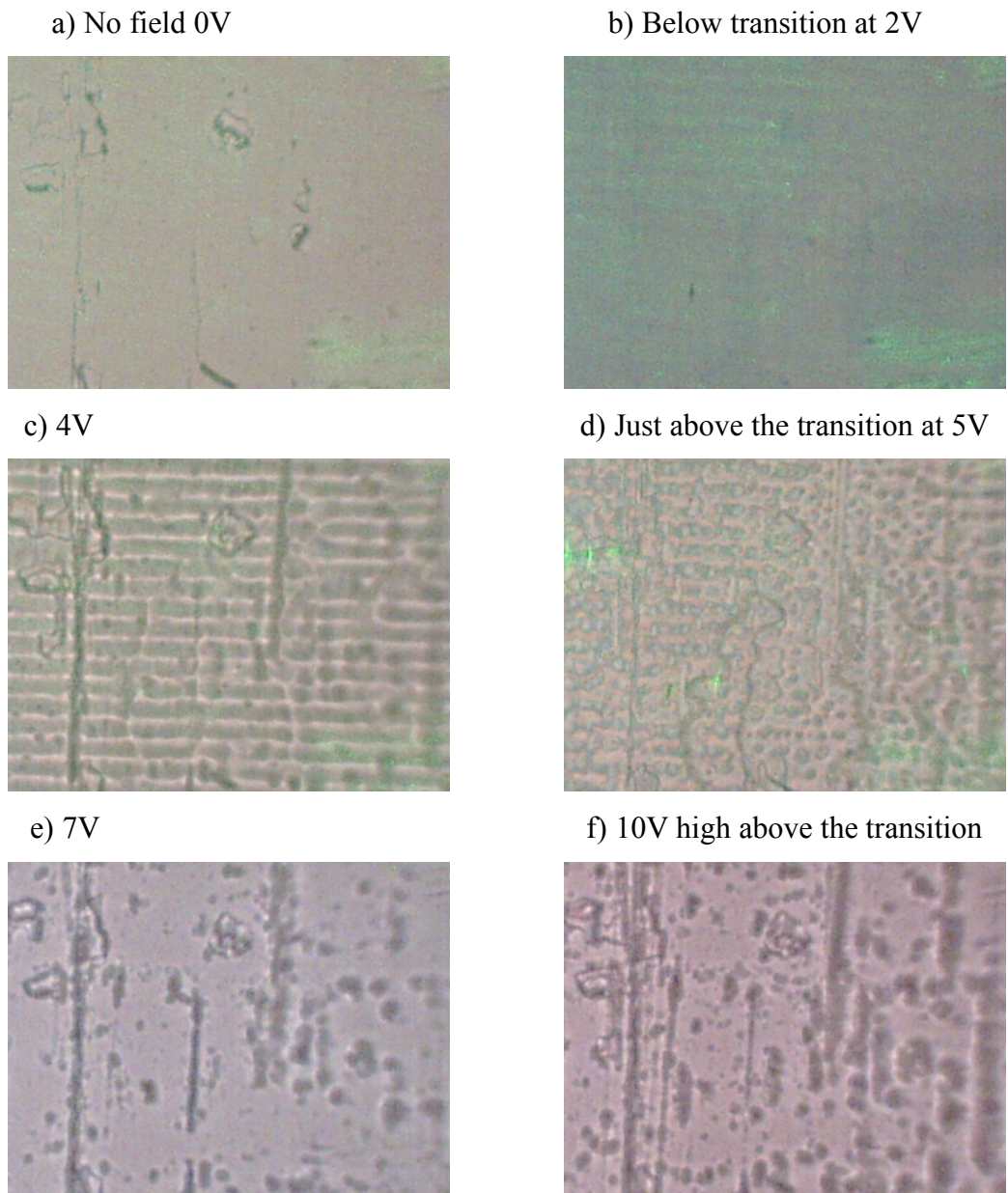
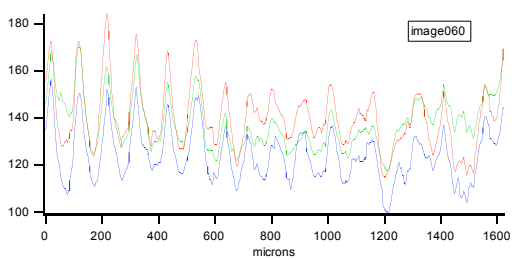
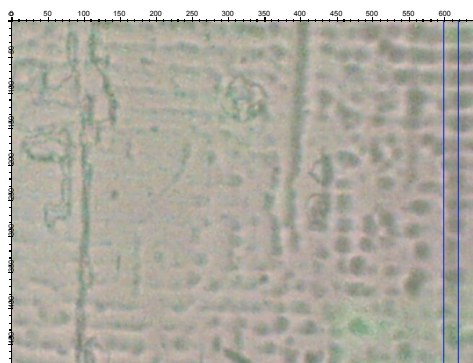


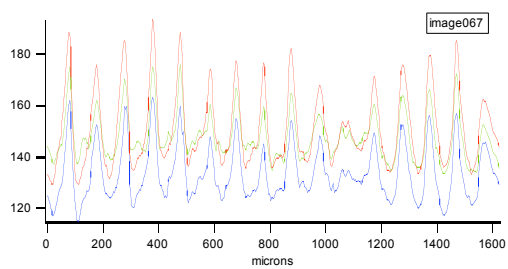
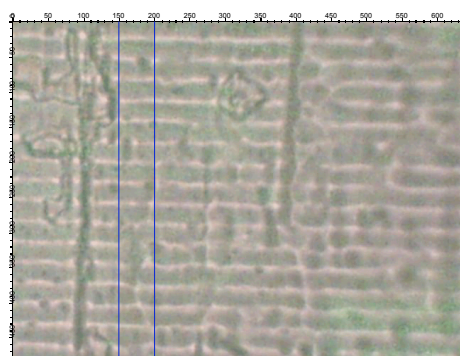
Figure 5.7 – Polarising microscope images of steady state grating at different applied voltages. Backlit by bright white LED.

a) 3.1v



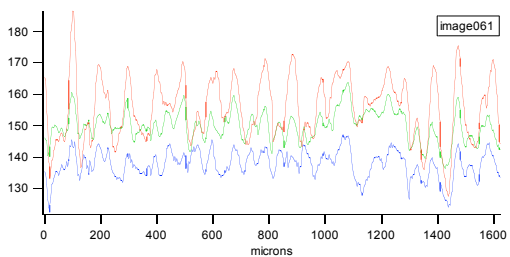
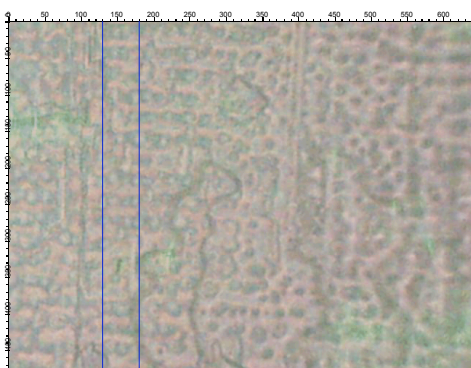
Mean Peak Spacing 101.85 +/- 5um

b) 4v



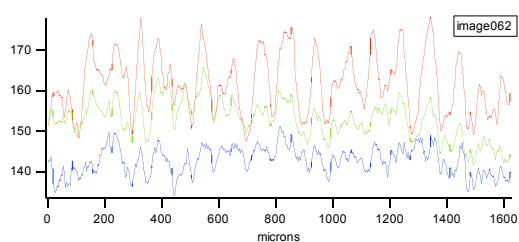
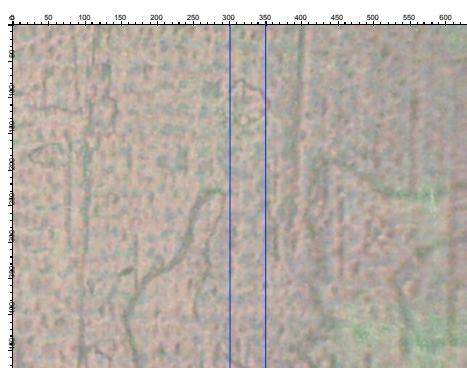
Mean Peak Spacing 99.4 +/- 4.3um

c) 5v



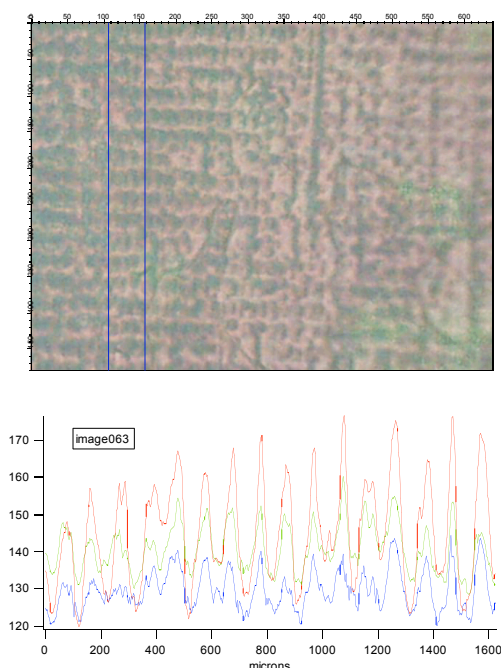
Mean Peak Spacing 101.85 +/- 5um

d) 6v



Mean Peak Spacing 95.6 +/- 5um

e) 7v



Mean Peak Spacing 101.85 +- 5um

Figure 5.8 - Polarising microscope images of a grating under different applied voltages. The line profiles are extracted from the images using the data range contained within the blue lines and provide grating spacings in microns. The red, green and blue lines represent the relative strength of their respective pixel colour values.

From these data a dynamic change in the gratings can be clearly seen as the field strength is increased, yet the grating spacing remains constant (within error estimates) for all voltages. This is likely due to the automatic contrast of the camera used which makes it difficult to see small changes in the width of the reoriented regions. It is concluded that this method provides good visual feedback of the grating with field strength, but cannot be used to accurately examine director profiles. This may be possible using a higher resolution camera positioned closer to the cell and without automatic gain.

5.3 Other experimental approaches to mapping periodic director profiles

It would be ideal to be able to inspect experimentally the director profile and use that information for better understanding of surface effects. The system investigated here, unlike in many other liquid crystal applications, has periodically changing electric field along the x-axis (due to periodic illumination) and therefore periodically changing director orientation. The experimental validation of such a periodically changing director is challenging and technically difficult for several reasons:

- i) There are presently no appropriate experimental methods to directly observe the variation of director field within a liquid crystal, mainly because any imaging apparatus would also need to have sufficient resolution (sub grating spacing) to observe such variation.
- ii) One must also overcome the technical challenges of re-creating the beam-coupling conditions (requiring electric field and writing lasers) at the same time as imaging the structure. It is difficult to position an observation apparatus close enough to measure the director yet not disrupt the writing beams
- iii) If such an imaging system is optical, then there is also the problem of optical diffraction from the grating structures whose spacing is on the order of microns. To avoid diffraction, and also to differentiate the writing and probe beams, the optical observation must be performed at a different frequency to the writing beams.

These restrictions rule out a lot of optical probing techniques, such as those used in chapter 4 for the investigation of uniform director profiles. Regarding point i), two experimental observation methods were evaluated, but both turned out to be unsuitable for this project.

The first method investigated was the half [68] or fully-leaky [69][70] guided mode technique as pioneered by Roy Sambles and colleagues. This is an optical technique in which the LC cell is sandwiched between two high-index optical prisms using index matching fluid. Early versions of this method relied upon using a specially designed

liquid crystal cell with a gold or silver surface layer. Via total reflection the input optical field would couple into a fully guided mode and surface plasmon-polariton in the metal layers. Reflectivity data versus incidence angle could be analysed to give information on the optical tensor of the LC over the depth of the evanescent optical field at one surface position. Using metal layers presented several problems, not least surface alignment problems with the LC. For these reasons, the metal layers were dropped in favour of coupling with index matched prisms [68] using the ‘Half-Leaky-Guided-Mode’ (HLGM) technique. With the loss of the surface plasmon, the modes became ‘leaky’ and broadened the reflectivity data, but yet retained enough resolution to extract director configuration information. Later, it was shown that by utilising both transmission and reflectivity data at different polarisations, sufficient resolution could be achieved to test commercial cells by using index-matched prisms.

These guided-mode systems offer an attractive method for analysing director structure, and can make use of a standard optical bench setup, the only technical difficulty being mounting the cell to the prisms with index matching fluid. Unfortunately, these methods are unsuitable for our periodic director structures, as they are based on optical frequencies and do not have the resolution to observe our micron-scale variations without being diffracted.

The second popular method of observing director structures is fluorescence confocal polarizing microscopy (FCPM). A traditional polarising microscope reveals only 2-dimensional data on liquid crystal orientation averaged through the depth of the sample. Confocal microscopy allows the microscope to focus on an adjustable narrow focal plane within 3-D space. The distance of this plane from the lens can be adjusted, and one can ‘scan’ through layers of a transparent material to build up a 3-D image. In FCPM, the liquid crystal sample is doped with a small amount of anisometric fluorescent particles which follow the alignment of the neighbouring liquid crystal molecules and director. Such a system is described by Lavrentovich in [71]. The system is attractive since the fluorescent doping partly avoids the problem of optical diffraction and it can create 3-dimensional maps of director orientation. However, these microscopes are very expensive to create and complex to maintain. Another major downside is that it cannot be used to evaluate existing cells or commercial samples since the LC must be doped with fluorescent particles during construction.

So method one cannot be applied to periodic structures of micron scale, and method two could in principle be used to investigate our samples, but requires significant investment and would still present considerable technical challenges in setting up a microscope at the same time as the grating. As a result of this evaluation, I concluded that there were two ways the problem of observing periodic director structures could be approached. These were either by direct/indirect experimental observation of the director with a high-tech and complex setup, or by using macroscopic photorefractive properties to inform a simulated model of a periodic structure, and comparing the output to other macroscopic properties such as diffraction efficiency or gain.

Modelling and simulation of these structures therefore became the logical and necessary step forward to increase our understanding of the SIPRE process. The rest of this chapter will focus upon my simulations of LC cells with periodically varying surface electric fields. Rather than model the entire photorefractive charge transfer process, I instead concentrated on the proposed result of these interactions, which is to create a periodically varying surface potential along one surface of the cell. I would look at how this affected the liquid crystal molecules and director within the cell and whether the predicted director profiles could be reconciled with experimental data. This would then act as an indicator as to whether the proposed theory of modulated surface potential was correct. Such simulation would also be useful in a more general sense for periodic electrodes in displays for instance.

5.4 Director Profile Modelling

To understand the reorientation process, I decided to perform modelling to simulate the reorientation mechanism and resultant director profiles of the cell. Parameters resulting from simulated propagation through the predictions can then be compared with experimental data.

Our model uses the Q tensor representation of director field [72] described in Appendix B and summarised here. This representation was chosen since it allows for reorientation in three dimensions. The cell is represented as a two dimensional Gauss-Lobatto grid in which the points become more closely spaced toward the surfaces. This is because all

the action is hopefully going on near the surfaces where the rate of change of director with distance is expected to be higher. The z-axis is therefore non-uniformly spaced and represents the cell thickness. The x and y axes are parallel to the surface plane but since this case is only dealing with a one dimensional grating, the x-direction represents the grating vector and the y-direction is assumed infinite. This grid represents the full thickness of the cell in z and one period in the intensity pattern in x. This is shown in figure 5.9.

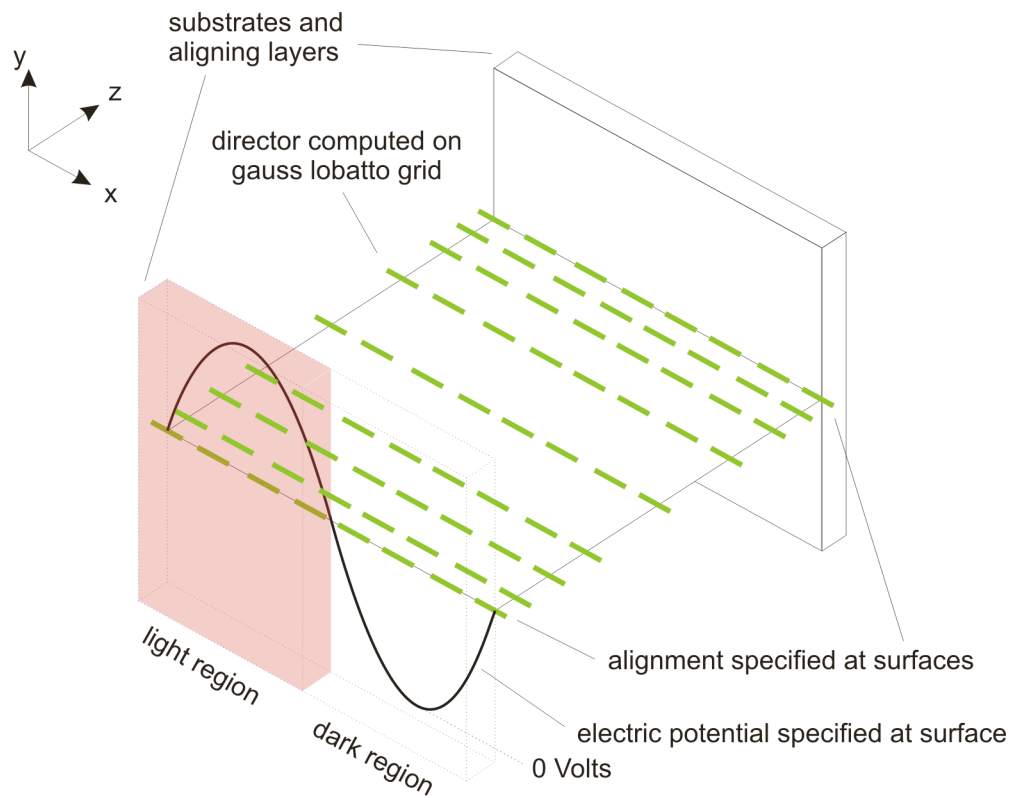


Figure 5.9 – Diagram of the axes used in modelling

In this model as a simplified starting point, a boundary potential is specified as a function of the direction; $\varphi(x)$. The assumption is that the \sin^2 light intensity pattern translates to a \sin^2 spatially varying surface potential via photo-induced recombination of charges. Whether the results of this model agree with experiment is a good test of this proposition.

The surface potential is used to calculate the x and z components of the electric field vector across the cell at each grid point. Knowing the electric field profile, the model resolves the director field by finding the minimum free energy for each point on the

grid, balancing the surface anchoring forces, the intrinsic elastic forces and the electric field forces on the molecules. This is accomplished by representing the liquid crystal order parameter as a traceless 3x3 symmetric tensor. Then the free energy density is defined as [73]:

$$L = \frac{1}{2}L_2 |\nabla Q|^2 + \frac{1}{2}A(T - T^*)\text{Tr}(Q^2) - \frac{\sqrt{6}}{3}B\text{Tr}(Q^3) + \frac{1}{4}C\text{Tr}^2(Q^2) - \frac{1}{2}\varepsilon_0 \mathbf{E} \cdot \varepsilon \mathbf{E}, \quad (5.1)$$

The leftmost term in this expression corresponds to the elastic energy, the last term the electrostatic energy and the others the bulk energy. T^* is known as the pseudo-critical temperature and is defined as a temperature point slightly below the nematic-isotropic transition temperature; T_c . It represents the point at which the isotropic phase becomes thermodynamically unstable and the LC is purely nematic. ε is a function of the dielectric tensor. Physical values of these parameters are discussed later in section 5.6. The free energy is used to obtain an equation of motion for the director field:

$$\xi \frac{\partial Q}{\partial t} = L_2 \nabla^2 Q - A(T - T^*)Q + \sqrt{6}BQ^2 - C\text{Tr}(Q^2)Q + \frac{2\varepsilon_0 \Delta \varepsilon}{3} E. \quad (5.2)$$

where non-dimensional parameters are introduced. These parameters are calculated from physical values and used as inputs to the simulation:

$(\xi, \zeta) = (x, z)/L_z$	L_z , Period of the modulation, length of x axis
$\beta = L_x/L_z$	Aspect ratio of the cell
$S = \frac{3C}{2B} \hat{S}$	Scaled order parameter
$Q = \sqrt{\frac{3}{2}} S \mathbf{n} \otimes \mathbf{n}$	Scaled tensor order Parameter
$T_c - T^* = \frac{2B^2}{9AC}$	T_c , Clearing point temperature
$\vartheta_Q = \frac{T - T^*}{T_c - T^*}$	Reduced temperature

$\xi_0^2 = \frac{9C}{2B^2} \frac{L_2}{L_z^2}$	Diffusion constant
$\tau_d = \frac{9C}{2B^2} \xi$	
$\tau = t/\tau_d$	non-dimensional time,
$\varphi = \hat{\varphi}/\varphi_0$	non-dimensional voltage, φ_0 typical voltage
$\varepsilon = \overline{\nabla\varphi \otimes \nabla\varphi}$	non-dimensional electrostatic tensor
$\chi_a = \frac{9\varepsilon_0\Delta\varepsilon C^2}{2L_z^2 B^3} \varphi_0^2$	Anisotropic electrostatic coupling
$\chi_l = \frac{82\varepsilon_0\varepsilon_l C^3}{8L_z^2 B^4} \varphi_0^2$	Isotropic electrostatic coupling

Finally five equations describing the components of the tensor field Q are obtained and the director orientation; \hat{n} , can be extracted from them These are shown in Appendix B.1.2.

5.5 Simulating the Model

The mathematical director representation presented in the previous section required computational modelling to be truly useful. A computational system was developed by [64] for this. The computational model however, was not easy to use by an experimentalist. It combined several dimensional parameters into unphysical proprietary non-dimensional parameters to simplify observing how the model varies as they change. To make the simulation as close to reality as possible, it was necessary to convert these to dimensional parameters that can be approximated from experiment.

For these reasons, I implemented an experimentalist's user interface known as DMAP (Director MAP). This program was written in MATLAB due to its extensive in-built support for scientific functions, and consists of a graphical interface on top of a series of calculations routines for the director configuration. It allows liquid crystal parameters and boundary conditions to be set by the user. The director field is obtained via the described model and displayed to the user as a data file or a choice of visualisations as shown in figure 5.10. It also allows selection between either a simple-yet-fast 2D scalar algorithm for the director calculation or the full 3D tensor implementation described in

the last section. The director angle along with the electric potential may be specified at each grid point along the surface.

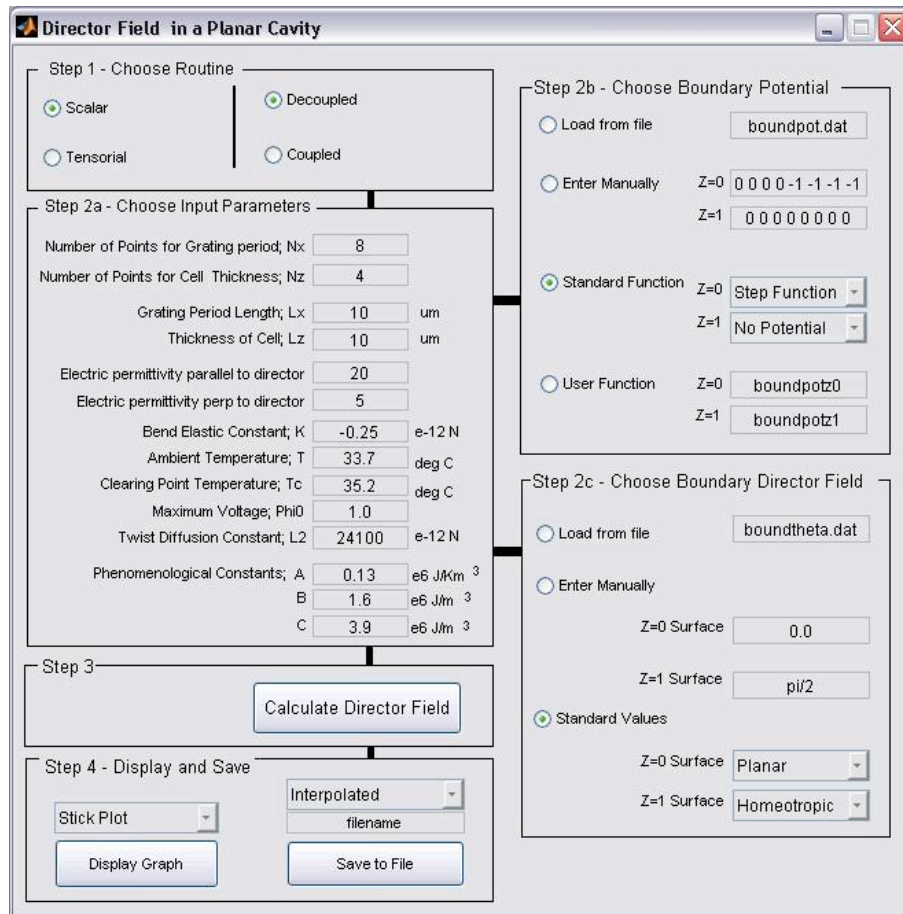


Figure 5.10 – Screenshot of the main DMAP program interface showing the input parameters

I also created graphical outputs from the simulations, providing contour, surface and stick plots for the electric field, refractive index and director configurations respectively. Examples of these graphs can be seen later in figures 5.12 to 5.14. Developing this program and refining the input parameters was a non-trivial task, but made assessing the effects of varying input parameters much easier and saved a lot of time in interpreting the simulation results.

Before implementing an interface to the computational model, it is useful to define the requirements of such a system to the user. The model is designed to be used by an experimentalist

to compare with experimental data and should therefore deal with physical inputs and outputs. Most important, is therefore the correct translation of user-entered physical parameters to the non-dimensional parameters of the model. In discussion with several possible end users, the agreed requirements were:

- Input Section
 1. The user must be able to specify the boundary condition on the potential. For ease of use, this may be done in a variety of ways:
 - a) Read the data from a file.
 - b) Enter the data by hand through a pop up window.
 - c) Chose a function from a small range (e.g. step function or sine squared function).
 - d) Use a user specified function.
 2. The user must be able to specify the boundary condition on the director field as above. Moreover, this must be possible both in the scalar case where the director field is represented by the angle θ and in the case where the tensorial representation is used. In the tensorial case, the boundary conditions should be given as the vector components of the director field and of the scalar order parameter.
- Output Section
 1. Produce surface and contour plots of all scalar fields and of the components of the electro-static field. These plots should be done using the interpolated fields.
 2. Produce stick or ellipsoid plots of the director field, also on the interpolated fields.
 3. Give the user the possibility to save any field in interpolated or non-interpolated form to a file.

Having assessed the requirements of the system, I then decided upon the procedure for program flow and the necessary user interface. The user interface provides a link between the user and the computational routines. It translates input parameters familiar to the experimentalist into non-dimensional parameters required by the model, executes the model with these parameters and then allows the user to visualise or save the results.

The interface is controlled by a 4 step procedure:

-
1. Choose Routine: Allows the user to choose which computational method to execute
 2. Enter Input Parameters.
 3. Execute Routine: Pressing this button starts the calculation routine, converting the input parameters, executing the computational routines, and creating a data set which can then be viewed or saved.
 4. Process Output.

Now I could turn my attention to translating the input parameters from physical to non-dimensional.

5.6 Input Parameters for the simulation

The interface allows the user to set the value of parameters in the mathematical model. The parameters are required to be non-dimensional. The job of the interface is therefore to translate typical physical parameters of Liquid Crystals into their non-dimensional equivalents to be supplied into the computation routines. Typical values of both the material properties and general system parameters can be found in tables 5.3 and 5.4.

ϵ_{\parallel}	20 (at $\approx 25^{\circ}\text{C}$)
ϵ_{\perp}	5 (at $\approx 25^{\circ}\text{C}$)
T_c	35.1°C
L_2	2.4×10^{-12} (N for $\hat{S}=0.65$)
A	$0.13 \times 10^6 \text{ JK}^{-1}\text{m}^{-3}$
B	$1.6 \times 10^6 \text{ Jm}^{-3}$
C	$3.9 \times 10^6 \text{ Jm}^{-3}$

Table 5.3 - Input Parameters for 5CB taken from [73][74]

n_x	8
n_z	4
L_x	10 μm
L_z	10 μm
T	25 $^\circ\text{C}$
ϕ_0	10 V
ϵ_{\parallel}	20
ϵ_{\perp}	5
T_c	35.1 $^\circ\text{C}$
L_2	$2.4 \times 10^{-8} \text{N}$
A	$0.13 \times 10^6 \text{ JK}^{-1} \text{m}^{-3}$
B	$1.6 \times 10^6 \text{ Jm}^{-3}$
C	$3.9 \times 10^6 \text{ Jm}^{-3}$

Table 5.4 - Default Input Parameters

I will describe each of these parameters in more detail.

- n_x ; n_x defines the number of grid points along the x-axis and thus defines the resolution of the model. The x-axis is defined as the axis along which there is a varying potential and ranges from $x = 0$ to $x = 1$. Increasing the value of n_x will thus allow the resolving of molecular direction with finer positional accuracy, at the expense of increased computation time. The grid points are distributed linearly across the cell.
- n_z ; Similarly, n_z defines the number of grid points in the model along the z-axis, representing the thickness of the cell. The z-grid points are on a non-linear Gauss-Lobatto grid since the most reorientation is expected to occur near the surface. The number of z points returned in the final data is equal to $n_z + 2$ due to the addition of an extra grid line at each boundary ($z = 0$ and $z = 1$) representing the boundary director states. The initial values for n_x and n_z are chosen to provide fast computation time with reasonable resolution. If aliasing-type effects are noticed, n_x or n_z can be increased.
- L_x ; The wavelength/period in microns of the boundary potential. This effectively defines the width of the model or the period of the interference grating along the

x-axis. This value is used with L_z to calculate the cavity aspect ratio β ; and also to scale the data matrix for output graphs.

- L_z ; The thickness or the cell measured in microns. In the model, this is the distance $z = 0 \rightarrow 1$. This value is used to scale the graphs as well as in the calculation of χ_α and ξ_0^2 . An increase in L_z will decrease both non-dimensional values quadratically. Typical cell thicknesses range from 10 – 100 μm .
- ε_{\parallel} and ε_{\perp} ; These are the electric permittivity parallel and perpendicular to the LC director respectively. They are used in the calculation ε_l and $\Delta\varepsilon$ used by the non-dimensional parameters α and γ and χ_α . A larger $\Delta\varepsilon$ increases both α and χ_α a linearly.
- T, T^*, T_c ; These are the ambient temperature of the liquid crystal, the pseudo-critical point at which the isotropic phase becomes unstable and the clearing point temperature respectively. They are used in the non-dimensional parameter θ_Q . It is the values $T-T^*$ and T_c-T which are important. One can use an ambient temperature $\approx 1.5^\circ$ lower than the critical point as this represents the molecules still in the nematic regime yet easy to reorient. $T_c = 35.2^\circ$ for the Liquid Crystal 5CB. T^* is calculated from the critical point temperature and the phenomenological constants A, B and C (see below)
- L_2 ; The diffusion coefficient L_2 as defined in appendix B. This is dependent on the twist elastic constant and the scalar order parameter. Typical values are $L_2 = 2.4 \times 10^{-12} \text{N}$ for $S=0.65$ and $K_2 = 3 \times 10^{-12} \text{N}$. L_2 is linearly proportional to the non-dimensional diffusion constant ξ_0^2 .
- A, B, C ; Phenomenological constants for the Landau De-Gennes model. These are different for each liquid crystal. Values for the Cyano-biphenyl homologues are in Coles [74] and for 5CB they are: $A=0.13 \times 10^6 \text{ JK}^{-1} \text{m}^{-3}$, $B=1.6 \times 10^6 \text{ Jm}^{-3}$, $C=3.9 \times 10^6 \text{ Jm}^{-3}$. These values affect the scalar order parameter; S , the pseudocritical temperature, ξ_0^2 and χ_α .

Also required as input parameters are the boundary conditions:

- Potential; The potential on the boundaries $z = 0$ and $z = 1$ is specified as n_x element row vectors in one of four ways:

-
1. Load From File; The potential is read-in from the file specified in the current working directory. The first n_x fields in the file (separated by white space) become an n_x element row vector representing $\varphi_z = 0, x = 0 \rightarrow 1$ and the $(n_x + 1) \rightarrow (n_x \times 2)$ fields an n_x element row vector representing $\varphi_{z=1, x=0 \rightarrow 1}$.
 2. Enter Manually; The user must enter an n_x element string of numbers, separated by white space characters to represent the normalised boundary voltage.
 3. Standard Function; The user is allowed to choose from three pre-defined scenarios; a step function, sinusoidal, or \sin^2 potential. These are simply calculated as a function of the normalised position along the boundary; ζ .
 4. User Function; The strings entered must be the name of a valid function in the same directory which return an n_x element column vector of potential when supplied with an n_x element column vector of ζ (x-position) values from zero to one.

The resulting row vectors are then transposed for input into the calculation routines.

- Scalar Boundary Director; This is specified by two scalar angles, one at $z = 0$ and one at $z = 1$. The angles are specified in radians. When loading from a file, the file should contain two numbers separated by whitespace. The first is read as the angle the molecules make with the x-axis at the $z = 0$ boundary and the second as the pretilt at $z = 1$ boundary.
- Tensor Boundary Director; The specification of the tensor boundary conditions are more complex. The user is required to enter the 5 components of the tensor; $a_{0 \rightarrow 5}$ without multiplication by the scalar order parameter. These 5 components are then each multiplied by the scalar order parameter; S_{eq} and provided as parameters to the computation.
 1. Load From File; The first 5 fields in the file (separated by whitespace or delimiter characters) are taken as the values $a_{0 \rightarrow 5}$ above for the $z = 0$ boundary and the second 5 fields as the $a_{0 \rightarrow 5}$ values for the $z = 1$ boundary.
 2. Enter Manually; The components are entered as 5 numeric values separated by whitespace characters in the order a_0 to a_5 .

5.7 Simulation Results - Electric Field

The electric field is specified as a function of x each grid point along both surfaces. It is assumed that the surface charge modulation follows the \sin^2 intensity function and therefore that the electric field along the boundary is also a \sin^2 function. The second boundary potential is set at 0 Volts to represent the side of the cell connected to ground. First, I generate electric-field vectors for each grid point from the surface potentials. Then I create contour profiles of the resulting electric field strength from these. Contour profiles for $30\mu\text{m}$ thick cells with different grating spacings are shown in figure 5.11.

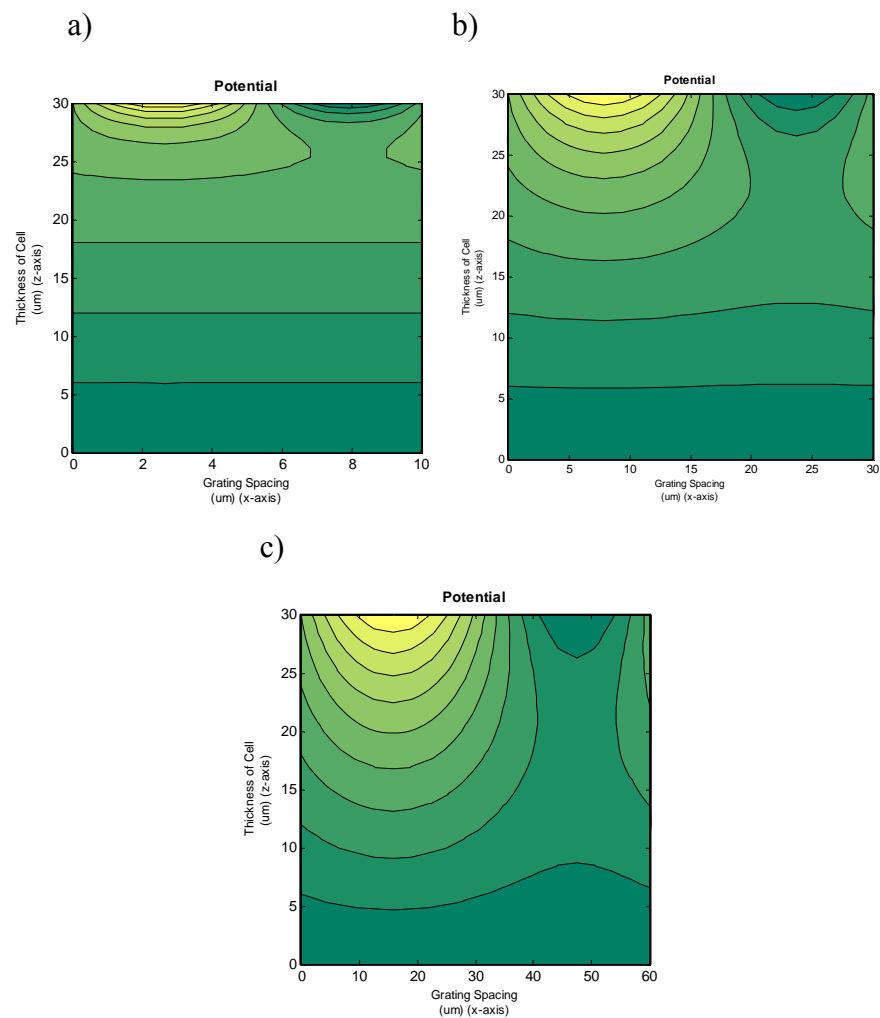


Figure 5.11 – Electric Field simulations as a function of grating period for $30\mu\text{m}$ thickness cells. a) $10\mu\text{m}$ grating period b) $30\mu\text{m}$ grating period c) $60\mu\text{m}$ grating period

It can clearly be seen that for grating spacing much larger than thickness the electric field variation penetrates far into the cell and the dark regions see much lower field strength. For grating spacing less than thickness the electric field variation penetrates only a short distance into the cell before following a uniform decline to the far substrate.

This key discovery tells us that to affect more of the LC bulk with reorientation then the size of cells is of critical importance. For example, thinner cells allow greater bulk reorientation for the same illuminating grating spacing.

5.8 Simulation Results – Director Fields and Refractive Index

Knowing the electric field distribution in our cell, one can use the model to calculate the resultant director vector; \hat{n} , at each point on the grid. The director structures and corresponding refractive index plots predicted from this electric field are shown in figures 5.12 and 5.13.

There is a lot of information to take in from these diagrams, but a few key points to bring out. Firstly, the parameters for the model were tuned to the experimental data using values in ref. [72] and a definite bulk Freedericksz transition can be seen between 3-4V, corresponding with experimental observations. Thus one can be fairly confident that the simulation represents the actual physical situation very closely.

As shown in the previous section, for larger grating spacing to cell thickness ratios, the electric field infiltrates further into the LC bulk. This has a knock on effect with the director orientation as seen in figure 5.12, namely that the electric field modifies more of the liquid crystal alignment for larger values of grating spacing. Reorientation takes place deeper into the cell and the grating becomes more uniform across the thickness of the cell.

This becomes more evident examining figure 5.13. It can clearly be seen that the threshold voltage for bulk reorientation occurs between 2 and 5 volts. For small grating spacings (i.e. 10 μ m) this means that the entire bulk is mostly reoriented. Looking at the

refractive index profile for 60 μm grating spacing at 5V, one can see that because the electric field is now fully affecting the bulk, the conditions are getting closer to a binary grating with approximately half the bulk affected. At this point just above the Fredericksz transition, the largest difference between maximum and minimum refractive index occurs, namely a case where there is a balance between surface forces and electric field (figure 5.14a – bottom right). These would be the ideal conditions to observe high diffraction efficiency. Looking at figure 5.14b, it can be seen that increasing the applied field does not increase the quality of the refractive index grating, and can actually introduce unwanted extra modulation to the refractive index.

In this model the director field is uncoupled to the electric field and does not account for the alteration of electric field by induced polarization on the LC molecules. Some work has been started on an extension to this model incorporating these effects, and such a simulation would be a good extension of these results.

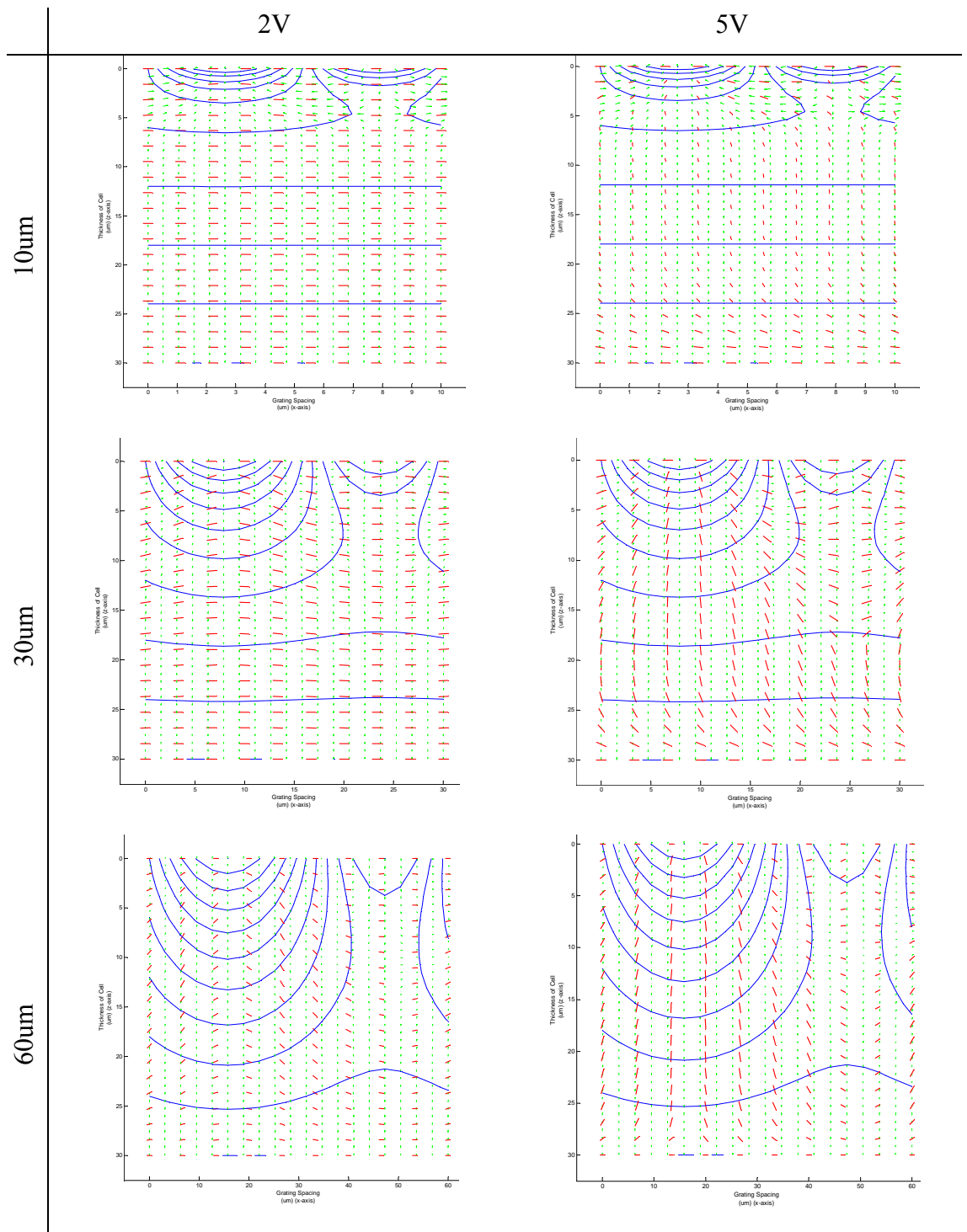


Figure 5.12a – Electric field (blue lines) and director orientation (red lines) for 30µm thick cells with varying grating period and applied fields of 2V and 5V. The green arrows show electric field vectors. The electric field modifies more of the liquid crystal alignment for larger values of grating spacing.

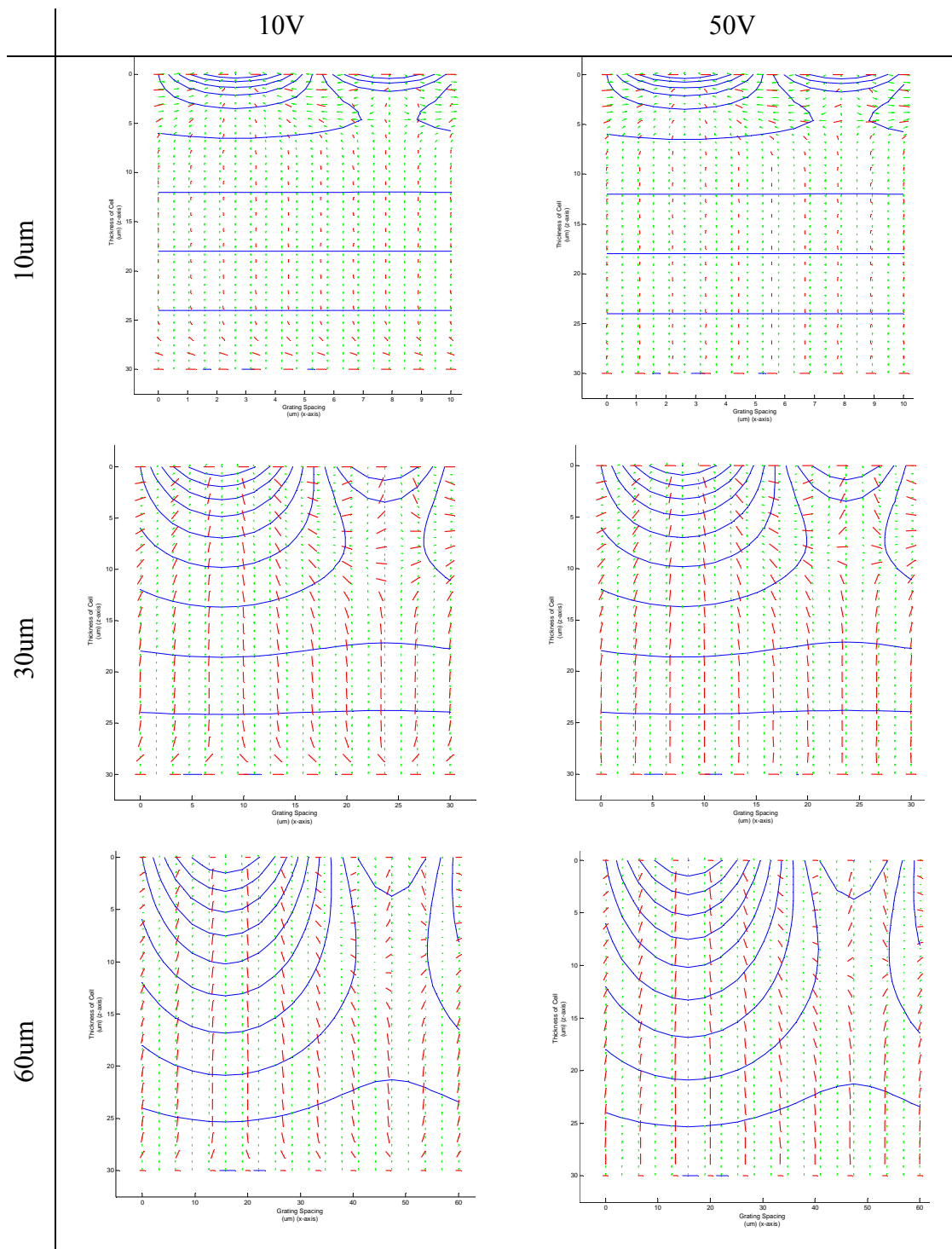


Figure 5.12b – Electric field (blue lines) and director orientation (red lines) for 30 μm thick cells with varying grating period and applied fields of 10V and 50V. The green arrows show electric field vectors. The electric field modifies more of the liquid crystal alignment for larger values of grating spacing.

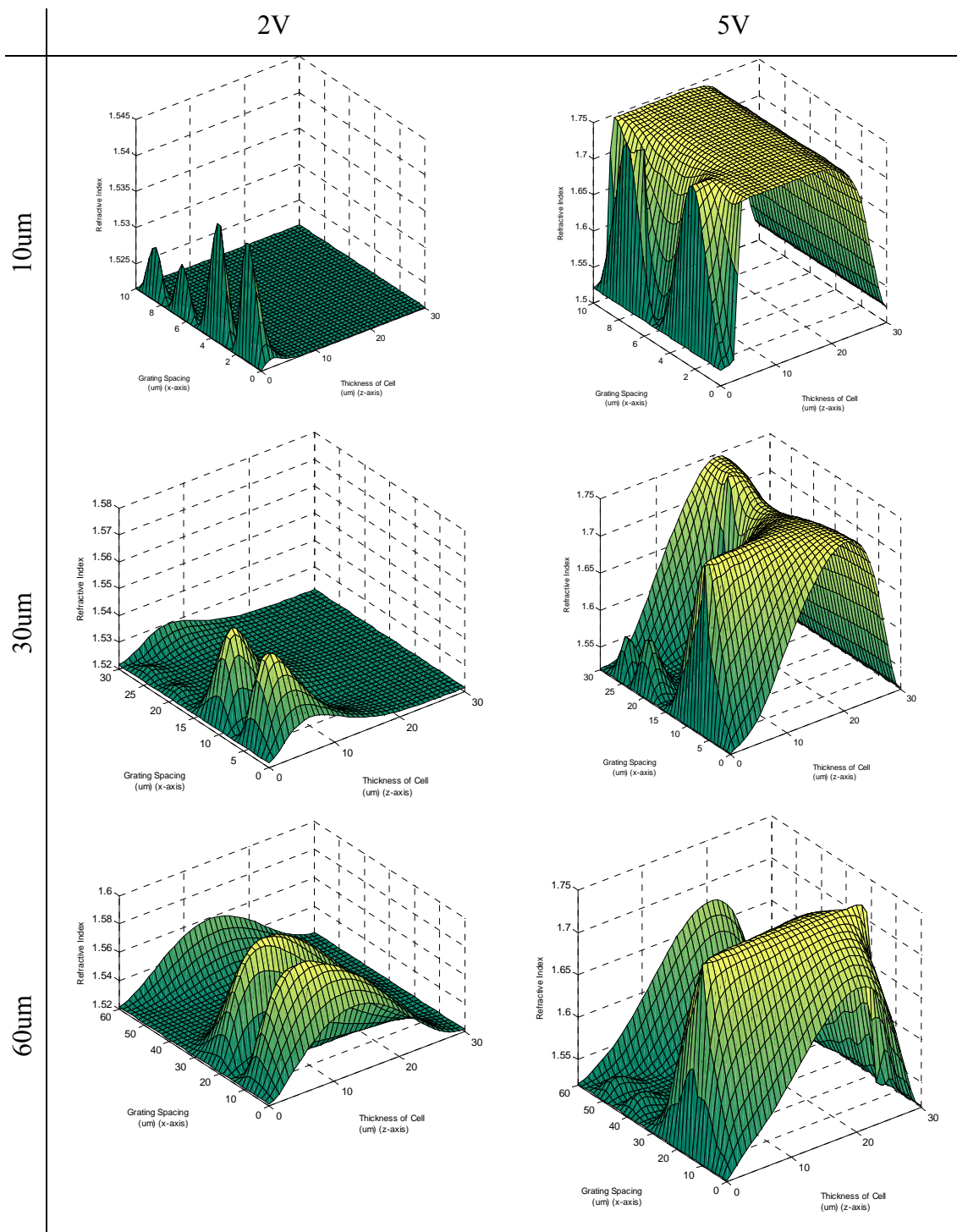


Figure 5.13a – Refractive index surface plots of the cells in figure 5.3a for a 543.5nm probe beam with wavevector normal to the glass substrates. The height represents the refractive index seen by this beam for the molecular orientation at that point. The largest modulation of refractive index is seen for large values of grating spacing just above the threshold (bottom right image).

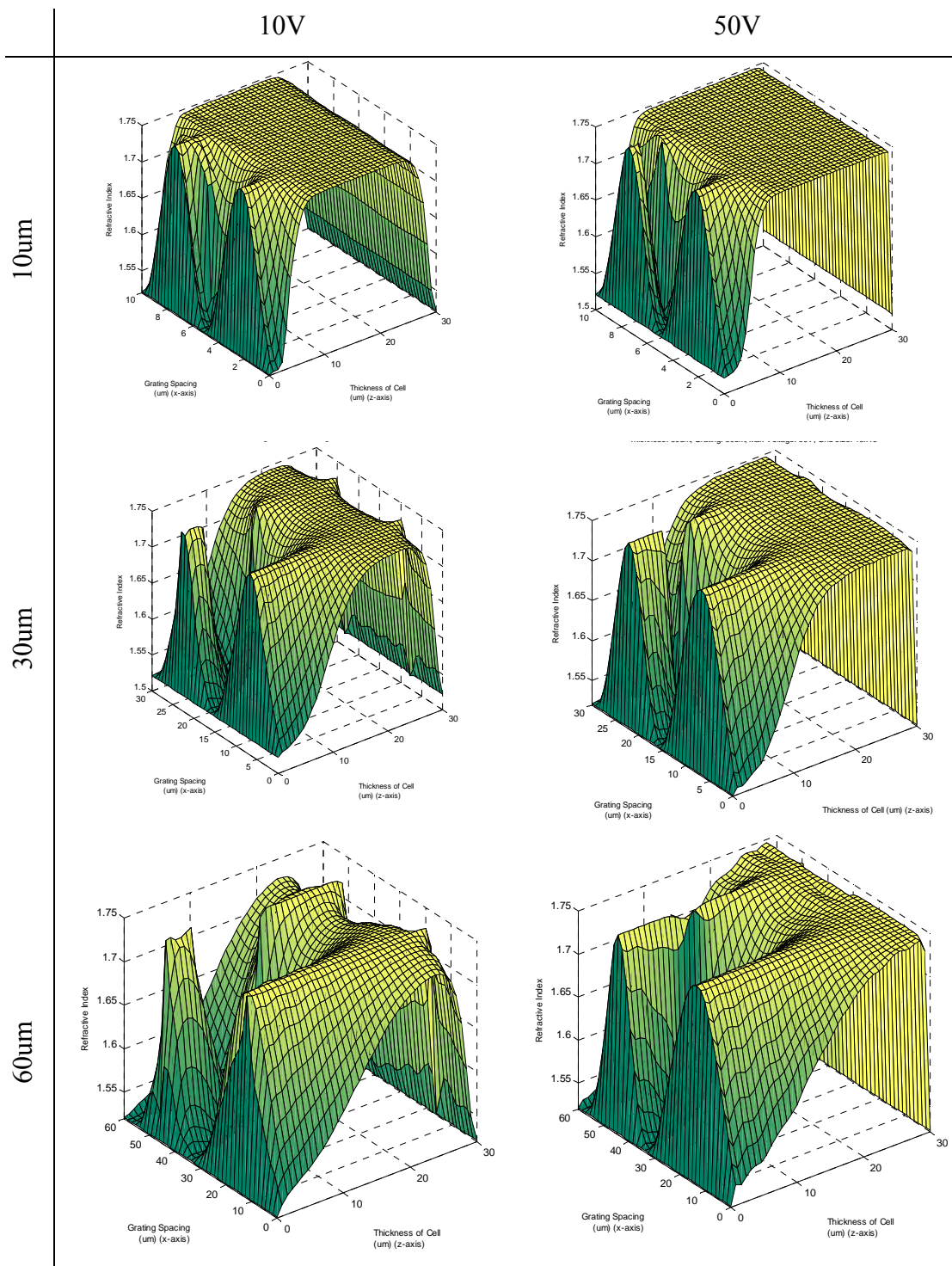


Figure 5.13b – Refractive index surface plots of the cells in figure 5.3b for a 543.5nm probe beam with wavevector normal to the glass substrates. The height represents the refractive index seen by this beam for the molecular orientation at that point. For applied fields above 10V bulk reorientation is seen and the index modulation of the gating is low.

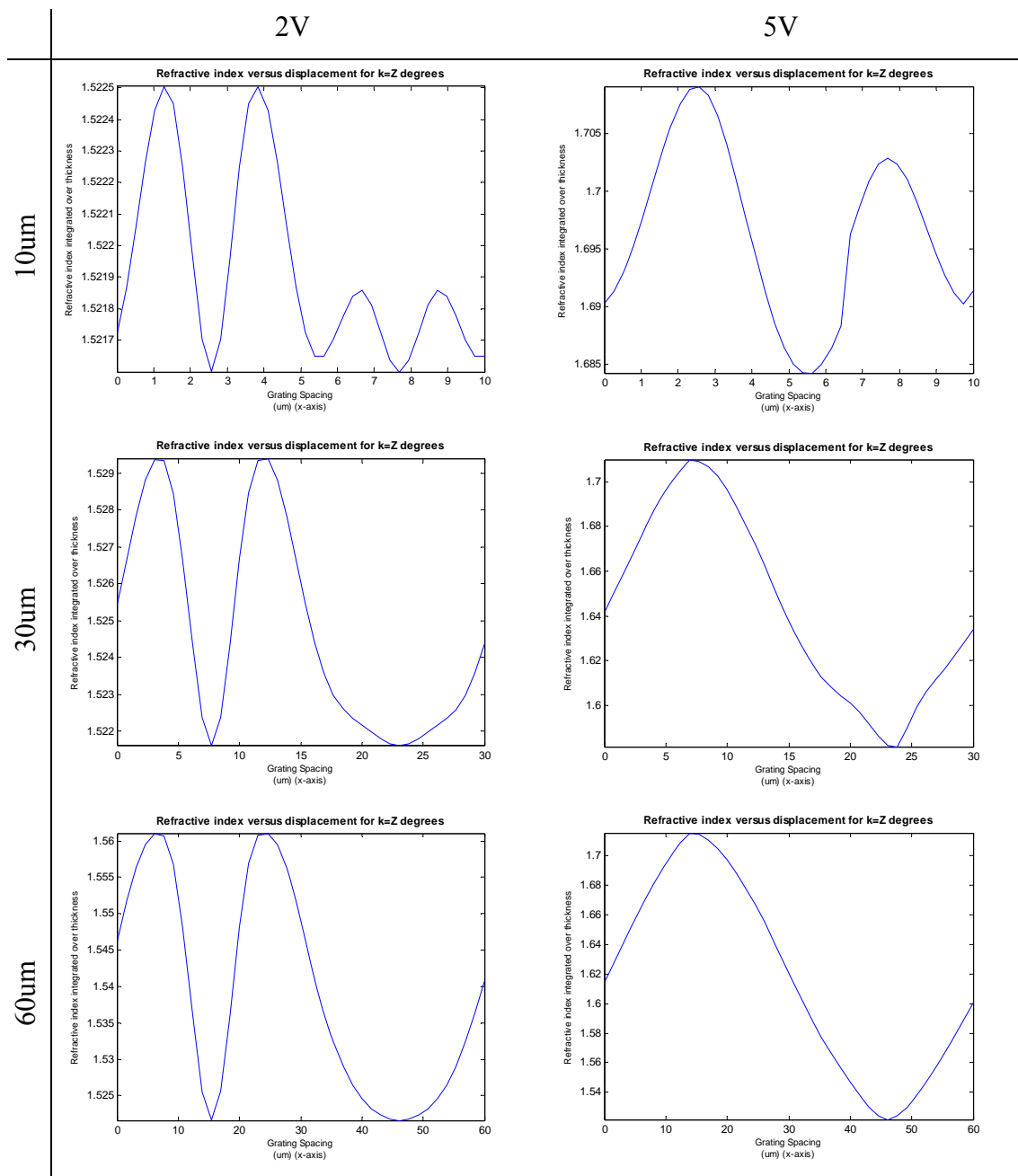


Figure 5.14a – Cross sectional refractive index plots from figure 5.4a averaged through the thickness of the cell. This is the average refractive index seen by light of wavelength 543.5nm travelling through the cell. Such data could be used to calculate diffraction efficiency. The largest index modulation is seen just above the Fredericksz transition threshold at 5V with a large grating spacing to thickness ratio of 60 μ m/30 μ m (bottom right image). These would be the best conditions to observe a large diffraction efficiency.

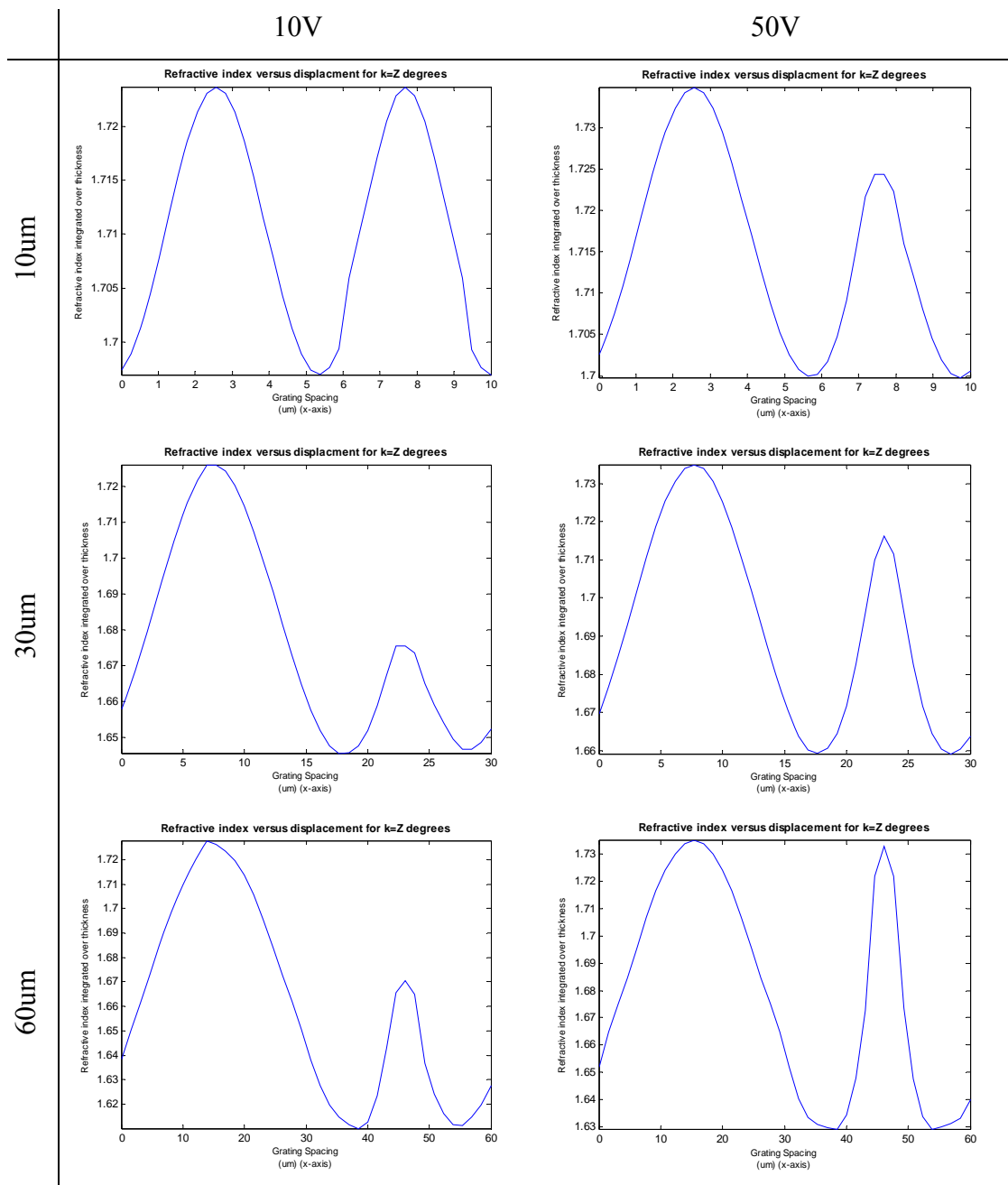


Figure 5.14b – Cross sectional refractive index plots from figure 5.4b averaged through the thickness of the cell. This is the average refractive index seen by light of wavelength 543.5nm travelling through the cell. These graphs are showing that increasing the applied field does not increase the refractive index modulation of the grating, but does seem to increase the extreme values of the modulation range.

5.9 Refining the simulation via birefringence experiments

The essential parameters and simulation developed in the previous sections required further development to allow comparison between the experimental results presented in sections 5.1 - 5.2 and the simulated results in the previous section. As previously noted, it is not technically possible to directly observe and map the periodic director profile to compare with simulated transmission profiles or director maps. For this reason, I chose a different method to validate the calculated maps. By simulating non-periodic director structures and extracting optical data, such as the birefringence, it is possible to refine the simulation parameters until they best represent the real-life material. One could then be reasonably confident of using these parameters for more complex geometries and for observing how varying other inputs affected the simulation.

The approach I took was to examine the birefringence of a non-modulated uniform cell which could be easily compared between simulations and experimental results. Once it was established that the material parameters for the simulation were correct for a uniform cell, these parameters could then be used in a more complex periodic configuration to predict the director profiles and refractive index modulation more accurately.

To this end, a series of birefringence experiments were performed on a range of similar cells and compared with the output from the simulation. These experiments involved systematic measurements on three cells with the same thickness and liquid crystal. All cells were filled with the liquid crystal E7 and two polymer aligning layers, PVK and polyimide were used. Three cells were fabricated as described in chapter 2, using the configurations shown in table 5.5.

To perform the experimental part of this comparison, a standard cell-between-polarisers setup (as in for example figure 4.1) was used. To investigate the optical response versus electric field, a voltage was applied across the cell whilst measuring the optical transmission using a 543.6nm laser beam. To prevent charge drift and the build-up of a screening layer at the interfaces, an AC field at 1KHz was applied. Even though this is

an applied AC field, the liquid crystal response to field strength is comparable to an equivalent strength DC field.

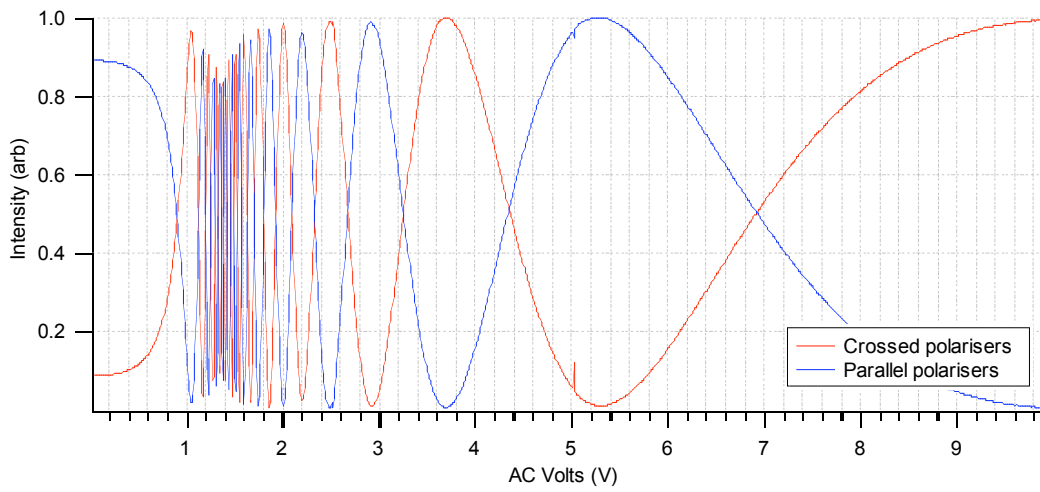
Cell #	Surface 1	Surface 2	LC filling	Width	Cell type
308	PI	PI	E7	30 μ m	Tilted planar
309	PVK:C60	PVK:C60	E7	30 μ m	Planar
310	PI	PVK:C60	E7	30 μ m	Planar with small pretilt on PI surface

Table 5.5 – Sample configurations for birefringence experiments

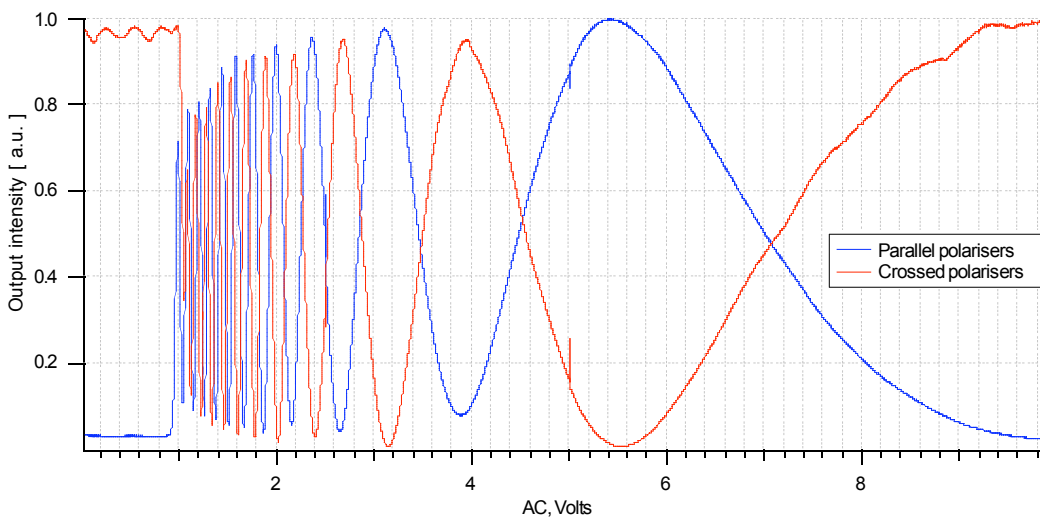
The LC cells were placed between crossed polarisers, measuring the optical transmission through the cell as a function of applied field. The experiment would then be repeated using parallel polarisers to provide a second data set and to check that this was the inverse of the first set of data. Data for these three samples is shown in figure 5.15.

To understand this data, it is necessary to consider how the LC responds to electric field. At sufficiently high voltage (in this case greater than 10 Volts, the LC molecules are completely reoriented with the field direction and in this case the total birefringence experienced by a beam passing through the cell ought to be at its lowest. As the field strength is decreased, the birefringence increases and the optical transmission is modulated as the ordinary and extraordinary beams go in and out of phase with each other. The first peak in transmission (maxima for parallel polarisers and minima for crossed polarisers) encountered whilst reducing field strength from full reorientation thus corresponds to a phase change of 2π between the ordinary and extraordinary beams. Counting down then the subsequent transmission peaks, each maxima is separated by 2π in phase, therefore the number of phase differences of π can be counted by using the voltage at each minima and maxima as a data point to produce a phase difference vs. voltage graph as in figure 5.15 d.

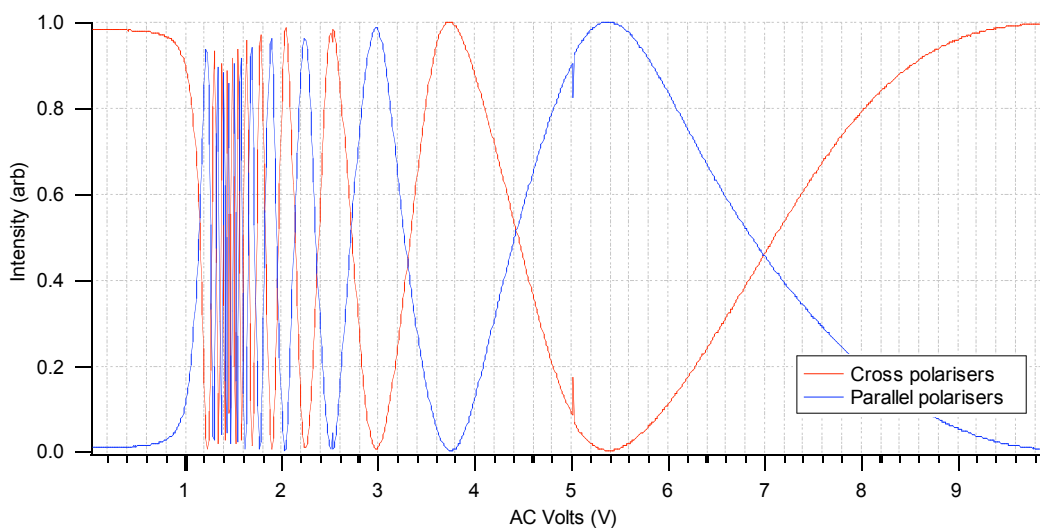
a) Cell 308 optical transmission



b) Cell 309 optical transmission



c) Cell 310 optical transmission



d) Retardation

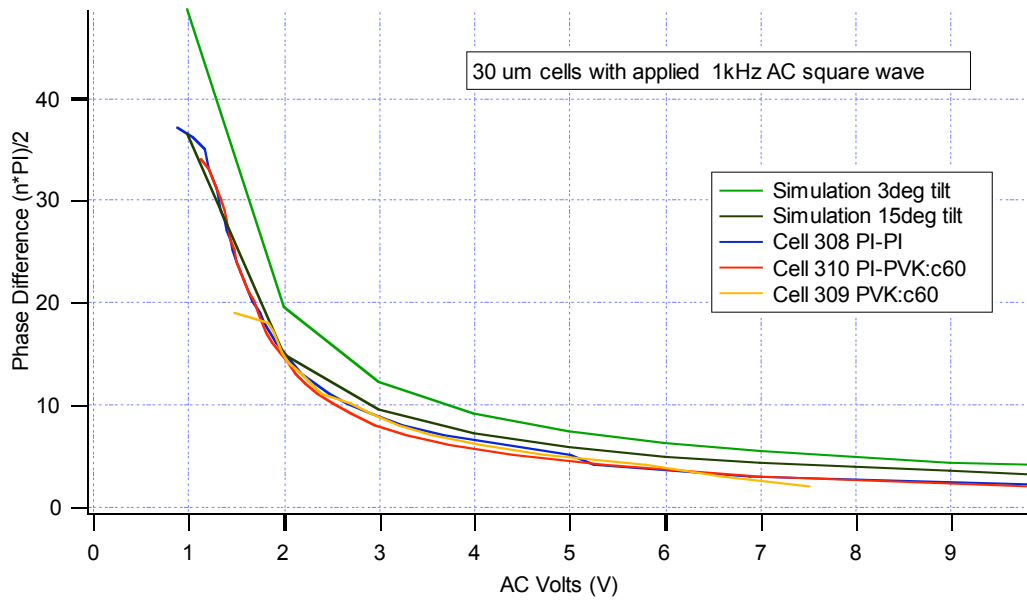


Figure 5.15 – Optical transmission data for three similar cells and equivalent calculated retardation

To compare against simulation, I had to extract birefringence data from simulated cells. A non-periodic cell was simulated using the same parameters as in section 5.7 and 5.8, generating a director map on a finite grid. To calculate the birefringence through this structure, I took the average of the birefringence at each grid point across the thickness of the cell. The birefringence at each lattice site is calculated using the relation:

$$\varphi = \frac{2\pi L_z \Delta n}{\lambda} \quad (5.3)$$

Where: $L_z = 30\mu\text{m}$
 $\lambda = 543.6\text{nm}$

using the refractive indices $n_e = 1.7462$ and $n_o = 1.5216$ for E7. This provided the phase difference/retardation for a beam incoming at an angle perpendicular to the surfaces. Since the simulation defines a ‘fixed’ pretilt angle for the closest layers of molecules to the surfaces (equivalent to strong anchoring), it is possible that for a small grid or a thin cell, these might have an overbearing effect on the director profile and thus the

birefringence. For this reason, I performed two series of simulations, one using a pretilt angle of 3° , similar to known values for PI, and one using a much higher pretilt of 15° to approximate the effects of weak anchoring.

Comparing the experimental retardation against that calculated via simulation (as half of the birefringence), I can ‘fit’ these curves by tuning the simulation parameters until the data matches more closely. The theoretical lines show the best fit which was obtainable by varying the material parameters of the simulation. There are many parameters in the simulation, and to avoid straying too far from sensible physical values, I started with known values for the permittivity and elastic constants of E7 (see table 5.4), as well as the Landau-de Gennes constants for 5CB; a known LC which is similar to E7. The simulation parameters for electrostatic coupling, diffusion constant, initial noise, Landau coefficients, grid size and surface angle were then varied to obtain the best fits of retardation.

As can be seen from figure 5.15d there is an apparent difference of π between the experimental and simulated phases. To begin with, this discrepancy was thought to be due to taking the wrong experimental maxima as the first 2π peak (i.e there may have been another peak above 10V). Repeated experiments to higher voltages (up to 40V) have shown that this is not the case and that the 10v peak is definitely the first and should correspond to a retardation of 2π . The second possible mechanism for this variation could be due to the width of a ‘fixed’ layer of surface molecules which are anchored very strongly nearer the surfaces of the cell. In the simulation the first layer of molecules on each surface is strongly anchored as a boundary condition, but if this layer were to be thinner there would be less birefringence and better agreement with experiments. This could be a function of simulation resolution and the use of a larger grid in the simulation would make this surface boundary less significant and hopefully reduce the birefringence.

Simulations were performed with larger grid sizes up to 32×32 points which did not change the calculated birefringence values. Lengthy computation time made simulations with grids larger than this unfeasible and thus I was not able to test this hypothesis further. It can be seen in figure 5.15d that enforcing a larger (15°) pretilt on the surfaces

in the simulation moves the curve closer to its experimental counterparts. This indicates that this difference is due in some way to the fixed boundary conditions in the simulation.

Despite this small discrepancy in absolute retardation value, the shape of the theoretical and experimental curves match very well and indicate that the material parameters used here match those of the experiments well and that the behaviour of the systems are similar. Hence, this gives confidence in the predicted director configurations and refractive index maps shown in figures 5.12-5.14.

5.10 Summary

There has been considerable interest in improving liquid crystal materials and structures to achieve high diffraction efficiencies and two-beam coupling gain ratios using the SIPRE. The previous reported attempts concentrated on considering various combinations of liquid crystal materials, dopants and polymers to achieve the maximum two-beam coupling gain. In my experiments, carried out on E7 and newly synthesised liquid crystal LC 1294 combined in cells with photosensitive, doped polymer PVK:C₆₀, I demonstrated that high gains can indeed be observed. However, in order to optimise the gain and at the same time achieve long term stability and reproducibility, the effect of experimental geometry, material constants and periodic modulation of electric field on the surface need to be included and modelled.

In the approach presented in this chapter I concentrated on establishing the essential experimental and material parameters to aid the theoretical simulations of reorientation gratings. This was the first step in getting a better understanding of the SIPRE process. I performed basic observations of the profile of gratings formed during the SIPRE and but their analysis proved challenging. Very high contrast and low noise was needed, as well as detecting fringe spacing with micron size resolution. Further work will need to be carried out to use the grating images to extract the information about director configuration. .

Since full-director observation was not technically feasible, I produced a comprehensive modelling tool to simulate such profiles. Part of the task included creating a

computational wrapper and developing software for a theoretical model of director field. Using this software, it was discovered that the ratio of grating spacing to cell thickness was a key factor in the amount of reorientation and the shape of the director profile. The model predicted the best diffraction efficiency at just above threshold voltage (between 2-5 volts) and high grating spacing to thickness ratio. I then compared simulated birefringence for non-periodic structures with experimental results to check and feed the experimentally established material parameters into simulations. A very good match was found for birefringence measurements and their theoretical fit. This test of parameters used for the theoretical model gave an important validation of director and electric field maps for the more complex case of periodic structures.

In future work, in order to produce a more direct simulation and comparison with experimental diffraction efficiency and two-beam coupling data, a full-beam propagation modelling will need to be carried out. The next step would be to do this in isotropic, periodically modulated media, and then extend that to propagation through the simulated director profiles presented in this chapter. This will then allow for the direct comparison between macroscopic experimental variables and simulation and also identify the optimum experimental conditions and configurations for various device applications. Work is currently underway towards this future work with simulations through isotropic media.

Chapter 6 – Conclusions and Further Work

Liquid crystals are extremely attractive candidates for photorefractive photonics applications due to the fact that they are inexpensive and exhibit high nonlinear optical response.

A system for measuring the director direction in a uniform cell has been developed and shown to be valid for director angles $0-16.3^\circ$ and $48.8-90^\circ$ from the surfaces, depending on the refractive indices of the material. I have analysed this method to measure the pretilt in a large number of cells which agree with published results for similar materials. It has been determined that the technique described in Chapter 2 produces cells with alignment stable for at least one year. It has also been determined that PVK alignment layers exhibit zero pretilt, a factor that must be considered during TBC experiments. I present some magnetic null method results which agree with the CRM but exhibit too much signal noise for our main experiments. Mathematical methods for the calculation of pretilt angle are presented and evaluated. I also use the developed system to characterise some cells which have been ‘damaged’ and exhibit long-term memory effects. It is found that it is easy to replicate these effects using high optical power in the LC1294-PVK samples, but not E7-PVK samples. It is theorised that these effects are the result of some uncontrolled surface charge at the LC-polymer interface. Hence, LC1294 is probably not a good candidate for beam coupling or optical switching applications, but has considerable promise for writing permanent or semi-permanent patterns with light and electric field [75].

I have created, characterised and simulated a series of cells utilising the liquid crystals E7 and LC1294 and polyimide and PVK alignment layers. I have also performed simulation to determine the director profiles of a cell with a periodic boundary potential. I have drawn conclusions from the preliminary data and it is clear the grating spacing to cell thickness ratio governs the penetration of electric field into the LC bulk. We also have seen that the largest refractive index variation occurs at a voltage just above the threshold for reorientation which is the ideal point for high diffraction efficiency.

Furthermore, I have used the cells with photoconductive alignment layers to create gratings using the surface-induced photorefractive effect and measured the period of these gratings and examined their formation and appearance with increasing voltage. I have compared the optical retardation with increasing applied AC field strength of three different cells to the equivalent simulated retardation and used a fitting process to obtain simulation parameters more suited to real cells.

6.1 Future for the Project

The work presented here has established a basis for the continued application of the surface induced photorefractive effect in liquid crystal-polymer systems to photonics devices. I have also established several new avenues of interest for LC-polymer devices. There are several avenues of further extension to this project, following up options which were not carried out due to time restrictions.

An interesting option would be to extend the pretilt characterisation work to create an ‘all-in-one’ pretilt measurement system utilising a variety of measurement and calculation methods to be able to reliably and accurately determine the pretilt angle of any cell placed into it.

To extend the simulation work I have carried out, a good experimental counterpart would be to use fluorescence/polarising confocal imaging to look at how the 3-dimensional director structure changes through the thickness of a cell. This would be a tricky experiment to perform but ultimately rewarding and very insightful. Another method of comparing the simulated results to experiment would be to extract diffraction efficiency data from the refractive index plots in figures 5.13 and 5.14 and compare these to experimental results for similar cells.

The simulation work presented here could also be extended and refined. Firstly by creating a simulation where the electric field is coupled to the director field and takes into account the feedback on electric field strength caused by induced polarisation on the LC molecules. Secondly, by including the flexoelectric effect caused by splay in the

LC, which; if not present in the unmodulated cell, will be present as a periodic splay in the modulated cell.

In the longer term, from a devices point of view, it would be interesting to investigate new materials (liquid crystals and polymers) to try to achieve higher diffraction efficiencies and beam-coupling gains. By increasing the resolution of the spacing, the focus can be moved to 2 dimensional gratings in the form of spatial light modulators. The work presented here will be key to the understanding of which materials to choose for which of these applications.

Appendix A – IGOR Programs to Determine Pretilt Angle from CRM Data

Presented here are the computer codes developed and used for taking the data in chapter 4. The main function is named `collect_data()` and controls the equipment and data acquisition. The later functions are analysis functions used to determine pretilt angle from the collected data.

```
// Program to calculate the pretilt angle of a LC cell (30-09-2005)
// Version 8

Function pretiltbuttonpress(ctrlName) : ButtonControl
    String ctrlName
    SVAR wavenam = root:panelwaves:globalwavename
    WAVE /T lctable = root:panelwaves:lctable

    variable Ne
    variable No
    variable align

    controlinfo /W=panell lclist
    // Number of selected row from listbox "lclist" returned as
    V_Value
    Ne = str2num( lctable [V_Value][1] )
    No = str2num( lctable [V_Value][2] )

    controlinfo /W=panell listalign
    // Number of selected row from listbox "listalign" returned as
    V_Value
    align = V_Value

    controlinfo /W=panell listmethod
    // Number of selected row from listbox "listmethod" returned as
    V_Value

    if ( V_Value == 0)
    // If first item in list selected
        findpeaks(wavenam, Ne, No,1,align)
        // call function to calculate pretilt angle from 2 user
        selected maxima
    elseif ( V_Value == 1)

        findpeaks(wavenam, Ne, No,2,align)
        // call function to calculate pretilt angle from 2 user
        selected minima
    elseif ( V_Value == 2)

        findpeaks(wavenam, Ne, No,3,align)
```

```

        // call function to calculate pretilt angle from 1 user
        selected maxima
elseif ( V_Value == 3)

        findpeaks(wavenam, Ne, No,4,align)
        // call function to calculate pretilt angle from 1 user
        selected minima
elseif ( V_Value == 4)
        peakratio(wavenam, Ne, No)
        // call function to calculate pretilt angle from user
        selected peaks
endif
End

Function motor_button(ctrlName) : ButtonControl
    String ctrlName
    WAVE /T step = root:panelwaves:step
    variable stepval

    controlinfo /W=panell liststep
    // Number of selected row from listbox "liststep" returned as
    V_Value
    stepval = str2num( step [V_Value] )

    controlinfo /W=panell listmotordir
    // Number of selected row from listbox "listmotordir" returned
    as V_Value
    if ( V_Value == 1)
    // If anticlockwise is selected
        stepval = stepval*-1
        // Set step to be negative
    endif

    MOT(stepval)

End

%%%%%%%%%%%%%%%%%%%%%%%%%%%%%%%%%%%%%%%%%%%%%%%%%%%%%%%%%%%%%%%%%%%%%%%%%%%%%%
%%%%%%%%%%%%%%%%%%%%%%%%%%%%%%%%%%%%%%%%%%%%%%%%%%%%%%%%%%%%%%%%%%%%%%%%%%%%%%

// Functions for collecting data
// Collect data() - Function creates angular intensity wave using
Crystal Rotation Method. Modified from Andriy's version 05-02-2004
// MOT() - used to move the stepper motor +/- 1,5,10,30,60 degrees.
Modified from Andriy's version 27-04-2004.
//

Function collect_data()
    SVAR wavenam = root:panelwaves:globalwavename
    // get values of wavename and NIDAQ
    NVAR channel = root:panelwaves:NIDAQchannel
    // from global variables

    variable stepsf=60, stepsb=60
    // number of degrees forward/backward. If this is changed from
    60 then STEPB60.exe will need to be changed
    variable k=0
    variable n=0

    ExecuteScriptText "\"C:\CRYSTAL ROTATION\PASCAL
FILES\STEPB60.exe\"" //Move motor 60 degrees back

```

```

variable t0
t0= ticks
do
while( ticks < (t0+720) )
// delay for 1 seconds starting from next line
t0= ticks
//sleep 00:00:15
//Pause to let the motor get into position

Make/N=((stepsf+stepsb)*5+1)/O intensity //
Wave to store transmitted intensity as cell rotates. /O
overwrites any waves with the same name
setscale /I x (stepsb*-1), stepsf, "degrees", intensity
// Set x-axis to measure in degrees.
intensity =0

display /N=intengraph intensity
//display graph to show data being taken

do
// loop for rotating cell and collecting data

    Variable Average=0
    Variable/G Photo3=0
    Variable ,j=0
    j=0
    Photo3=0

    do
        Photo3+=fNIDAQ_ReadChan(1, channel,1)
        //Take a reading and add it to the total.
        j += 1
        // Increment the loop variable.
    while(j < 200)

    Average = -Photo3/200
    //Find the average value
    print Average
    print n
    intensity [n] = Average
    Dowindow /K intengraph
    display /N=intengraph intensity

    ExecuteScriptText/B      "\"C:\CRYSTAL      ROTATION\PASCAL
    FILES\FORW20.exe\""
    //Move the motor forward 0.2 degrees

    t0= ticks
    do
    while( ticks < (t0+35) )
    // delay for ? seconds starting from next line
    //t0= ticks

    n+=1
    //Increment the loop variable
while (n!=(stepsf+stepsb)*5+1)
//keep repeating until full range has been measured

if ( cmpstr( wavenam, "intensity" ) )
// if wave not already named 'intensity' then

```

```

        if ( waveexists($wavenam) )
            killwaves $wavenam
            // If the named wave exists, delete it
        endif
        rename intensity, $wavenam
        // Rename data wave to name specified by user.
    endif

    display $wavenam
    // display the wave as a graph

    t0= ticks
    do
    while( ticks < (t0+100) )
        // delay for 1 seconds starting from next line
        t0= ticks
        ExecuteScriptText          "\"C:\CRYSTAL          ROTATION\PASCAL
        FILES\STEPB60.exe\"""      //Move motor 60 degrees back
    endwhile

end

Function MOT(step)
    variable step
    if (step==1)
        ExecuteScriptText          "\"C:\CRYSTAL          ROTATION\PASCAL
        FILES\STEPB1.exe\"""      //Move motor 1 degrees clockwise
    elseif (step==5)
        ExecuteScriptText          "\"C:\CRYSTAL          ROTATION\PASCAL
        FILES\STEPB5.exe\"""      //Move motor 5 degrees clockwise
    elseif (step==10)
        ExecuteScriptText          "\"C:\CRYSTAL          ROTATION\PASCAL
        FILES\STEPB10.exe\"""     //Move motor 10 degrees clockwise
    elseif (step==30)
        ExecuteScriptText          "\"C:\CRYSTAL          ROTATION\PASCAL
        FILES\STEPB30.exe\"""     //Move motor 30 degrees clockwise
    elseif (step==60)
        ExecuteScriptText          "\"C:\CRYSTAL          ROTATION\PASCAL
        FILES\STEPB60.exe\"""     //Move motor 60 degrees clockwise
    elseif (step==1)
        ExecuteScriptText          "\"C:\CRYSTAL          ROTATION\PASCAL
        FILES\STEPF1.exe\"""      //Move motor 1 degrees
        counterclockwise
    elseif (step==5)
        ExecuteScriptText          "\"C:\CRYSTAL          ROTATION\PASCAL
        FILES\STEPF5.exe\"""      //Move motor 5 degrees
        counterclockwise
    elseif (step==10)
        ExecuteScriptText          "\"C:\CRYSTAL          ROTATION\PASCAL
        FILES\STEPF10.exe\"""     //Move motor 10 degrees
        counterclockwise
    elseif (step==30)
        ExecuteScriptText          "\"C:\CRYSTAL          ROTATION\PASCAL
        FILES\STEPF30.exe\"""     //Move motor 30 degrees
        counterclockwise
    elseif (step==60)
        ExecuteScriptText          "\"C:\CRYSTAL          ROTATION\PASCAL
        FILES\STEPF60.exe\"""     //Move motor 60 degrees
        counterclockwise
    endif
end

```

```

// Functions to calculate pretilt angle using peak selection method
//
// findpeaks(wavenam) - displays wave in window and ask the user to
draw boxes around 2 symmetrical peaks, then
// calculates symmetry point and pretilt using eq. 3.2 in
paper ONG (1991)
// pauseforgraph(graphname) -displays graph with cursors and wait for
user to press continue
// UserCursorAdjust_ContButtonProc(ctrlName) - hides graph window
when "continue" is pressed and continues program
//

// findpeaks(wavenam) - parameters are; wavenam -> string of wave
name containing angular intensity readings
// Peak values are calculated using waves own scaling. the waves x-
axis should therefore be already scaled in degrees to
// get a pretilt angle in degrees

function findpeaks(wavenam, Ne, No,mode,align)

    string wavenam
    variable Ne
    variable No
    variable mode
    variable align
    variable peak1
    variable peak2
    variable PsiX
    variable alpha
    string grphname="PretiltAngle"

    display $wavenam
    //display the graph in a new window
    DoWindow/C $grphname
    // Rename the window so that the rest of the function can
reference it

    if (mode ==1)
    // if selected 2 peak (maxima)
        pauseforgraph(grphname)
        // call function to show graph and button
        getmarquee /K bottom
        // Find left and right values of the selection box
        findpeak /R=(V_left,V_right) $wavenam
        //Find the first peak in the selection
        peak1=V_PeakLoc
        //V_PeakLoc returns the x value corresponding to the max y
value

        pauseforgraph(grphname)
        // call function to show graph and button
        getmarquee /K bottom
        // Find left and right values of the selection box
        findpeak /R=(V_left,V_right) $wavenam
        //Find the first peak in the selection
        peak2=V_PeakLoc
        //V_PeakLoc returns the x value corresponding to the max y
value

        PsiX=((peak1+peak2)/2)

```

```

        // Find symmetry point in wave

elseif (mode ==2)
// if selected 2 peak (minima)
pauseforgraph(grphname)
// call function to show graph and button
getmarquee /K bottom
// Find left and right values of the selection box
findpeak /N /R=(V_left,V_right) $wavenam
//Find the first minima in the selection
peak1=V_PeakLoc
//V_PeakLoc returns the x value corresponding to the max y
value

pauseforgraph(grphname)
// call function to show graph and button
getmarquee /K bottom
// Find left and right values of the selection box
findpeak /N /R=(V_left,V_right) $wavenam
//Find the first minima in the selection
peak2=V_PeakLoc
//V_PeakLoc returns the x value corresponding to the max y
value

PsiX=((peak1+peak2)/2)
// Find symmetry point in wave

elseif (mode ==3)
// if selected 1 peak (maxima)
pauseforgraph(grphname)
// call function to show graph and button
getmarquee /K bottom
// Find left and right values of the selection box
findpeak /R=(V_left,V_right) $wavenam
//Find the first minima in the selection
PsiX=V_PeakLoc
//V_PeakLoc returns the x value corresponding to the max y
value

elseif (mode ==4)
// if selected 1 peak (minima)
pauseforgraph(grphname)
// call function to show graph and button
getmarquee /K bottom
// Find left and right values of the selection box
findpeak /N /R=(V_left,V_right) $wavenam
//Find the first minima in the selection
PsiX=V_PeakLoc
//V_PeakLoc returns the x value corresponding to the max y
value
endif

if (align ==0)
// if selected homeotropic
alpha= PsiX/No
// calculate pretilt using symmetry point
elseif (align ==1)
// if selected planar
alpha= PsiX/(Ne+No)
// calculate pretilt using symmetry point
endif

```

```

    print "Pretilt angle is:",alpha
    DoWindow/K $grphname // Kill self

end

Function pauseforgraph(graphname)

    string graphname

    DoWindow/F $graphname // Bring graph to front
    if (V_Flag == 0) // Verify that graph exists
        Abort "Pauseforgraph: No such graph."
        return -1
    endif

    NewPanel/K=2 /W=(139,341,382,432) as "Pause for Selection"
    DoWindow/C tmp_PauseforGraph
    // Set to an unlikely name
    AutoPositionWindow/E/M=1/R=$Graphname
    // Put panel near the graph
    DrawText 21,20,"Drag the selection box around the peak"
    DrawText 21,40," and then press Continue."
    Button button0,pos={80,58},size={92,20},title="Continue"
    Button button0,proc=UserCursorAdjust_ContButtonProc
    PauseForUser tmp_PauseforGraph,$Graphname

End

Function UserCursorAdjust_ContButtonProc(ctrlName) : ButtonControl
    String ctrlName
    DoWindow/K tmp_PauseforGraph // Kill self
End

////////////////////////////////////
////////////////////////////////////

// Functions to calculate pretilt angle using multiple peak method.
// (Jin Seog Gwag et al. 2003)
//
// peakratio(wavenam) - Calculates pretilt angle using ratio of
// birefringence functions for 2 maxima & 2 minima in angular
// transmission
// as for findpeaks() function, waves x-axis should be scaled in
// degrees already
//
// f(alpha, beta, Ne, No) - calculates birefringence function of alpha
// and beta
// it was found that equation in Jin Seog Gwag et al. does
// not reproduce their results.
// Here we use the equation from Cuminal & Brunet (1996)
// which reproduces the correct transmission curve and pretilt angle
//

function peakratio(wavenam, Ne, No)

    string wavenam
    variable Ne
    variable No

```

```

findpeak /R=(0,leftx($wavenam)) $wavenam
variable B1=(V_PeakLoc)
//Find first maxima before 0 degrees

findpeak /R=(0,rightx($wavenam)) $wavenam
variable B2=(V_PeakLoc)
//Find first maxima after 0 degrees

findpeak /N /R=(B1,rightx($wavenam)) $wavenam
variable B3=(V_PeakLoc)
//Find first minima after B1 degrees

findpeak /N /R=(B2,rightx($wavenam)) $wavenam
variable B4=(V_PeakLoc)
//Find first minima after B2 degrees

// B1=-8*Pi/180
// B2= 6.7*Pi/180
// B3= 0*Pi/180
// B4= 12.5*Pi/180

print B1
print B2
print B3
print B4

Make /N=1800 /O biref
//wave to store birefringence function. eq. (10) in Gwag et. al
(2003)
Make /N=1800 /O degrees
setscale /I x -90, 90, "degrees", biref

variable k=0
do
    variable fb1 = f( ((k/10)-90)*Pi/180 ,B1,Ne,No)
    variable fb2 = f( ((k/10)-90)*Pi/180 ,B2,Ne,No)
    variable fb3 = f( ((k/10)-90)*Pi/180 ,B3,Ne,No)
    variable fb4 = f( ((k/10)-90)*Pi/180 ,B4,Ne,No)
    // Calculate parameters for eq. 10 from Gwag et. al (2003)

// biref [k] = (fb4-fb3)/(fb2-fb1)
// evaluate this function at f=1
biref [k] = abs( (fb4-fb3)/(fb2-fb1) -1)
// evaluate at f=1 by shifting zeroing function and taking
absolute
degrees [k] = (k/10)-90

    k+=1
while (k<1800)

display biref

findpeak /R=(0,rightx(biref)) /N biref
// Find minima in absolute of function -> value closest to zero
- alpha corresponding to pretilt angle
variable a= V_Peakloc
findpeak /R=(0,leftx(biref)) /N biref
// Find minima in absolute of function -> value closest to zero
- alpha corresponding to pretilt angle
variable b= V_Peakloc
print "pretilt is either "

```

```

    print a
    print b

end

function testf()

    variable Ne=1.6101
    variable No=1.4978

    variable B1=-15*Pi/180
    variable B2= 10*Pi/180

    Make /N=1800 /O f_gwag
    //wave to store birefringence function. eq. (10) in Gwag et. al
    (2003)
    Make /N=1800 /O f_other
    setscale /I x -90, 90, "degrees", f_gwag
    setscale /I x -90, 90, "degrees", f_other

    variable k=0
    do
        f_gwag[k] = f( ((k/10)-90)*Pi/180 ,B1,Ne,No)
        f_other[k] = f2( ((k/10)-90)*Pi/180 ,B1,Ne,No)
        k+=1
    while (k<1800)

    display f_gwag f_other

end

function f(alpha, beta, Ne, No)
//based on cuminal and brunet (1996)
    variable alpha
    variable beta
    variable Ne
    variable No

    variable n = sqrt( No^2*cos(alpha)^2 + Ne^2*sin(alpha)^2 )

    variable j = (No^2-e^2)*sin(alpha)*cos(alpha)*sin(beta)/n^2
    variable k = (No*Ne/n^2)*sqrt( n^2 - sin(beta)^2 )
    variable l = sqrt( No^2 - sin(beta)^2 )

    return k
//    return j+k-1

end

function f2(alpha, beta, Ne, No) // Based on Gwag et al. (2003) gives
different answer to above

    variable alpha
    variable beta
    variable Ne
    variable No

    variable a = 1/Ne
    variable b = 1/No
    variable c = sqrt( a^2*cos(alpha)^2 + b^2*sin(alpha)^2 )

```

```
variable j = (1/c^2)*(a^2-b^2)*sin(alpha)*cos(alpha) *sin(beta)
variable k = (1/c) * sqrt( 1 - ((a^2*b^2/c) *sin(beta)^2 ))
variable l = (1/b) * sqrt( 1 - ( b^2*sin(beta)^2 ) )

return k
// return j+k-l

end
```

Appendix B – Landau De-Gennes Model

B.1 Mathematical Model

The Landau De-Gennes model [17][72][73] is a phenomenological model initially created to describe the nematic-isotropic phase transition. It has since been expanded to cover other transitions and situations. This chapter describes a mathematical and computational implementation of a Landau De-Gennes model developed by [64]. This model describes the director field in a TBC cell subject to a periodically varying potential along the x-direction on the cell substrates. The cell is modelled as a planar grid perpendicular to the substrates, where the physical parameters are evaluated at normalised coordinates ξ and ζ in the x and z axes respectively. Since the potential is periodic in x, the director field is observed for one period of the grating, assuming this is repeated throughout the material.

B.1.1 The Tensor Order Parameter Model

Here I present the main derivation of the theory [64][72] and the relationship between the parameters of the model and the physical description. It is assumed that the liquid crystal can be represented by a 3×3 symmetric traceless tensor order parameter Q which is related to the director unit vector \mathbf{n} by:

$$Q_{ij} = \sqrt{\frac{3}{2}} \hat{S} \left(n_i n_j - \frac{1}{3} \delta_{ij} \right) \iff Q = \hat{S} \overline{\mathbf{n} \otimes \mathbf{n}} \quad (\text{b.1})$$

where $\overline{\mathbf{n} \otimes \mathbf{n}}$ is the traceless symmetric tensor product of \mathbf{n} with itself and \hat{S} is a scalar order parameter that indicates the local phase of the liquid crystal. It is important to note that in the physical case; $0 \leq \hat{S} \leq 1$, with $\hat{S} = 0$ and $\hat{S} = 1$ representing the completely isotropic and ordered states respectively. In the Landau-De-Gennes model used here, \hat{S} is unbounded and is essentially a description of local order. Using such notation, we find $\hat{S}^2 = \text{Tr}(Q^2)$.

The free energy density is defined as:

$$L = \frac{1}{2}L_2 |\nabla Q|^2 + \frac{1}{2}A(T - T^*)\text{Tr}(Q^2) - \frac{\sqrt{6}}{3}B\text{Tr}(Q^3) + \frac{1}{4}C\text{Tr}^2(Q^2) - \frac{1}{2}\varepsilon_0 \mathbf{E} \cdot \varepsilon \mathbf{E}, \quad (\text{b.2})$$

The leftmost term in this expression corresponds to the elastic energy, the last term the electrostatic energy and the others the bulk energy. T^* is known as the pseudo-critical temperature and is defined as the temperature slightly below the nematic-isotropic transition temperature, T_c . It represents the point at which the isotropic phase becomes thermodynamically unstable and the LC is purely nematic. ε is the dielectric tensor as defined in [73]:

$$\varepsilon_{ij} = \varepsilon_l \delta_{ij} + \sqrt{\frac{2}{3}}\Delta\varepsilon Q_{ij}. \quad (\text{b.3})$$

where $\varepsilon_l = (\varepsilon_{\parallel} + 2\varepsilon_{\perp})/3$, $\Delta\varepsilon = \varepsilon_{\parallel} - \varepsilon_{\perp}$ is the permittivity anisotropy and ε_{\parallel} and ε_{\perp} are the permittivities parallel and perpendicular to the molecular axis. Using the traceless electric tensor:

$$\varepsilon = \overline{\mathbf{E} \otimes \mathbf{E}} \Rightarrow \varepsilon_{ij} = \sqrt{\frac{3}{2}} \left(E_i E_j - \frac{|\mathbf{E}|^2}{3} \delta_{ij} \right) \quad (\text{b.4})$$

The free energy in equation b.4 can be expressed as:

$$L = \frac{1}{2}L_2 |\nabla Q|^2 + \frac{1}{2}A(T - T^*)\text{Tr}(Q^2) - \frac{\sqrt{6}}{3}B\text{Tr}(Q^3) + \frac{1}{4}C\text{Tr}^2(Q^2) - \frac{1}{2}\varepsilon_0 \varepsilon_l \mathbf{E} \cdot \mathbf{E} - \frac{2\varepsilon_0 \Delta\varepsilon}{3} \text{Tr}(QE), \quad (\text{b.5})$$

The equation of motion describing the link between the free energy and the director field is:

$$\zeta \frac{\partial Q}{\partial t} = \frac{\delta L}{\delta Q} \quad (\text{b.6})$$

where ζ is the viscosity coefficient of the liquid crystal. Substituting equation (b.2) into equation (6), the equation of motion for the director field becomes:

$$\zeta \frac{\partial Q}{\partial t} = L_2 \nabla^2 Q - A(T - T^*)Q + \sqrt{6}BQ^2 - C\text{Tr}(Q^2)Q + \frac{2\varepsilon_0 \Delta \varepsilon}{3} E. \quad (\text{b.7})$$

To simplify the description of the model, non-dimensional parameters are introduced to equation (b.7). These describe the relationship between the parameters of the model and physical reality. Equation (b.8) shows the scalings between these parameters which are used as the basis for the computational interface.

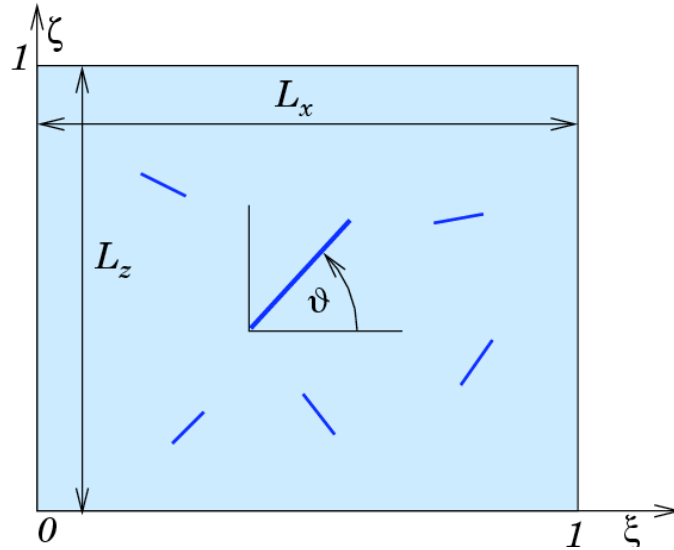


Figure B.1. - Diagram of the cell slice. The cavity is assumed to be infinitely extended along the y-axis (coming out of the page). The electrostatic field is applied between $\xi = 0$ and $\xi = 1$ generating a potential along both boundaries. The aspect ratio of the cavity β is given by the ratio L_x/L_z . The director is given by the angle θ measured from the horizontal (x-axis). [64]

$(\xi, \zeta) = (x, z)/L_z$	L_z , Period of the modulation, length of x axis
$\beta = L_x/L_z$	Aspect ratio of the cell
$S = \frac{3C}{2B} \hat{S}$	Scaled order parameter
$Q = \sqrt{\frac{3}{2}} S \mathbf{n} \otimes \mathbf{n}$	Scaled tensor order Parameter
$T_c - T^* = \frac{2B^2}{9AC}$,	T_c , Clearing point temperature
$\vartheta_Q = \frac{T - T^*}{T_c - T^*}$,	Reduced temperature
$\xi_0^2 = \frac{9C}{2B^2} \frac{L_2}{L_z^2}$,	Diffusion constant
$\tau_d = \frac{9C}{2B^2} \zeta$,	
$\tau = t/\tau_d$,	non-dimensional time,
$\varphi = \hat{\varphi}/\varphi_0$,	non-dimensional voltage, φ_0 typical voltage
$\varepsilon = \overline{\nabla\varphi \otimes \nabla\varphi}$	non-dimensional electrostatic tensor
$\chi_a = \frac{9\varepsilon_0 \Delta \varepsilon C^2}{2L_z^2 B^3} \varphi_0^2$,	Anisotropic electrostatic coupling
$\chi_l = \frac{81\varepsilon_0 \varepsilon_l C^3}{8L_z^2 B^4} \varphi_0^2$,	Isotropic electrostatic coupling

(b.8)

The equation of motion thus becomes:

$$\frac{\partial Q}{\partial \tau} = \xi_0^2 \nabla^2 Q - \vartheta_Q Q + 3\sqrt{6} Q^2 - 2\text{Tr}(Q^2) Q + \chi_a \overline{\nabla\varphi \otimes \nabla\varphi} \quad (\text{b.9})$$

where ∇^2 represents $\partial_{\xi}^2 + \beta^2 \partial_{\zeta}^2$. The non-dimensional free energy is now:

$$L = \frac{1}{2} \xi_0^2 |\nabla Q|^2 + \frac{1}{2} \vartheta_Q \text{Tr}(Q^2) - \sqrt{6} \text{Tr}(Q^3) + \frac{1}{2} \text{Tr}^2(Q^2) - \frac{1}{2} \chi_l \nabla\varphi \cdot \nabla\varphi - \chi_a \text{Tr}(QE), \quad (\text{b.10})$$

where γ_1 is Leslie's rotational viscosity [76]. The diffusion coefficient L_2 is:

$$L_2 = \frac{1}{3\hat{S}^2} K_2 \quad (\text{b.11})$$

where K_2 is the twist elastic constant of the LC. It is also important to note here that the values of the elastic ξ_0^2 and electrostatic χ_a coupling parameters are very small (of the order of 10^{-8} and 10^{-6}) and require scaling up computationally to be able to determine effects they produce. As long as the ratio between the two is kept constant, this does not affect the model.

The value of the order parameter at equilibrium (in the absence of elastic and electrostatic forces) can be calculated from equation (b.9) to be:

$$\vartheta_Q S_{eq} - 3S_{eq}^2 + 2S_{eq}^3 = 0 \Rightarrow S_{eq} = \frac{3 \pm \sqrt{9 - 8\vartheta_Q}}{4}. \quad (\text{b.12})$$

using the relations:

$$\text{Tr}(Q^2) = Q_{ij}Q_{ij} = S^2, \quad \text{Tr}(Q^3) = Q_{ij}Q_{jk}Q_{ki} = \frac{1}{\sqrt{6}} S^3. \quad (\text{b.13})$$

B.1.2 Representation on the Basis of the Traceless 3×3 Symmetric Tensors

Q is required to be a traceless symmetric tensor which is not the case in equation (b.9).

Using the technique in [72], Q is represented in terms of its components on the basis of

the traceless 3×3 symmetric tensors $T^{(i)}$, $i = 0, 1, \dots, 4$ such that:

$$\begin{aligned} T^{(0)} &= \frac{1}{\sqrt{6}} \begin{pmatrix} -1 & 0 & 0 \\ 0 & -1 & 0 \\ 0 & 0 & 2 \end{pmatrix} & T^{(1)} &= \frac{1}{\sqrt{2}} \begin{pmatrix} 1 & 0 & 0 \\ 0 & -1 & 0 \\ 0 & 0 & 0 \end{pmatrix} & T^{(2)} &= \frac{1}{\sqrt{2}} \begin{pmatrix} 0 & 1 & 0 \\ 1 & 0 & 0 \\ 0 & 0 & 0 \end{pmatrix} \\ T^{(3)} &= \frac{1}{\sqrt{2}} \begin{pmatrix} 0 & 0 & 1 \\ 0 & 0 & 0 \\ 1 & 0 & 0 \end{pmatrix} & T^{(4)} &= \frac{1}{\sqrt{2}} \begin{pmatrix} 0 & 0 & 0 \\ 0 & 0 & 1 \\ 0 & 1 & 0 \end{pmatrix} \end{aligned} \quad (\text{b.14})$$

The equations for the components a_k of the tensor Q on the element $T^{(k)}$ are:

$$\frac{\partial a_0}{\partial t} = \xi_0^2 \nabla^2 a_0 - \vartheta a_0 + 3(a_0^2 - a_1^2 - a_2^2) + \frac{3}{2}(a_3^2 + a_4^2) - 2a_0 \sum_{k=0}^4 a_k^2 + \chi_a e_0 \quad (\text{b.15})$$

$$\frac{\partial a_1}{\partial t} = \xi_0^2 \nabla^2 a_1 - \vartheta a_1 - 6a_0 a_1 + \frac{3\sqrt{3}}{2}(a_3^2 - a_4^2) - 2a_1 \sum_{k=0}^4 a_k^2 + \chi_a e_1 \quad (\text{b.16})$$

$$\frac{\partial a_2}{\partial t} = \xi_0^2 \nabla^2 a_2 - \vartheta a_2 - 3(2a_0 a_2 - \sqrt{3}a_3 a_4) - 2a_2 \sum_{k=0}^4 a_k^2 + \chi_a e_2 \quad (\text{b.17})$$

$$\frac{\partial a_3}{\partial t} = \xi_0^2 \nabla^2 a_3 - \vartheta a_3 + 3a_0 a_3 + 3\sqrt{3}(a_1 a_3 + a_2 a_4) - 2a_3 \sum_{k=0}^4 a_k^2 + \chi_a e_3 \quad (\text{b.18})$$

$$\frac{\partial a_4}{\partial t} = \xi_0^2 \nabla^2 a_4 - \vartheta a_4 + 3a_0 a_4 + 3\sqrt{3}(a_2 a_3 - a_1 a_4) - 2a_4 \sum_{k=0}^4 a_k^2 + \chi_a e_4 \quad (\text{b.19})$$

where ∇^2 the partial differential $\partial_{\xi}^2 + \beta^2 \partial_{\zeta}^2$ and e_k are the components of the tensor electric field, $e_k = \text{Tr}(\varepsilon T^{(k)})$. These five equations are integrated by the computational code to find the components of Q . The boundary conditions on the director field can be specified using the scalar order parameter S_{eq} as:

$$a_0 = \text{Tr}(T^{(0)}Q) = S_{eq} n_3^2 - \frac{S_{eq}}{2}(n_1^2 + n_2^2) \quad (\text{b.20})$$

$$a_1 = \text{Tr}(T^{(1)}Q) = \frac{\sqrt{3}}{2} S_{eq} (n_1^2 - n_2^2) \quad (\text{b.21})$$

$$a_2 = \text{Tr}(T^{(2)}Q) = \sqrt{3} S_{eq} n_1 n_2 \quad (\text{b.22})$$

$$a_3 = \text{Tr}(T^{(3)}Q) = \sqrt{3} S_{eq} n_1 n_3 \quad (\text{b.23})$$

$$a_4 = \text{Tr}(T^{(4)}Q) = \sqrt{3} S_{eq} n_2 n_3 \quad (\text{b.24})$$

where S_{eq} is given by equation (b.12).

B.1.3 The Electrostatic Field Equation

The equation for the electro-static field across the cell can be derived directly from Maxwell's equation if the displacement field \mathbf{D} is known in terms of the tensor order parameter. This is given by:

$$D_i = \varepsilon_0 \left(\varepsilon_l \delta_{ij} + \sqrt{\frac{2}{3}} \Delta \varepsilon Q_{ij} \right) E_j. \quad (\text{b.25})$$

The electro-static potential can then be expressed non-dimensionally as:

$$\varepsilon_l \nabla^2 \varphi + \sqrt{\frac{2}{3}} \Delta \varepsilon \left[\frac{\partial}{\partial \xi} \left(Q_{11} \frac{\partial \varphi}{\partial \xi} + Q_{13} \beta \frac{\partial \varphi}{\partial \zeta} \right) + \beta \frac{\partial}{\partial \zeta} \left(Q_{31} \frac{\partial \varphi}{\partial \xi} + Q_{33} \beta \frac{\partial \varphi}{\partial \zeta} \right) \right] = 0. \quad (\text{b.26})$$

B.1.4 The Scalar Limit

The computational code for calculating director field can be executed in two ways. Using the tensorial representation as demonstrated, or by using a much faster scalar approximation. In this scalar limit, it is assumed that the scalar order parameter is constant throughout the entire cell and defined by equation (b.12). In this situation, the director is represented much more simply by the angle ϑ it makes with the x-axis. There is assumed to be no y-component to the director such that it lies completely in the x-z plane as in figure b.1. The effect this has on the free energy density and the equation of motion is to remove dependence of the temperature parameter ϑ_Q and introduce the birefringence parameter:

$$\alpha_\vartheta \equiv \frac{\chi_a S / \chi_l}{1 - \chi_a S / (3\chi_l)} = \frac{\Delta \varepsilon S / \varepsilon_l}{1 - \Delta \varepsilon S / (3\varepsilon_l)}. \quad (\text{b.27})$$

The resultant non-dimensional free energy in (b.10) becomes:

$$L = \frac{1}{2} \xi_0^2 \partial_k Q_{ij} \partial_k Q_{ij} - \chi_a \text{Tr}(QE). \quad (\text{b.28})$$

Substituting the definition of E and the tensor order parameter expressed in terms of ϑ into this expression:

$$L_Q = \frac{3}{2} \xi_0^2 S^2 \partial_k \vartheta \partial_k \vartheta - \sqrt{\frac{3}{2}} \chi_a S \left\{ [\cos(\vartheta) \partial_\xi \varphi + \sin(\vartheta) \partial_\zeta \varphi]^2 - \frac{1}{3} |\nabla \varphi|^2 \right\}. \quad (\text{b.29})$$

$$\nabla^2 \vartheta - \alpha_\vartheta \gamma \left\{ \frac{1}{2} \sin(2\vartheta) [(\partial_\xi \varphi)^2 - (\partial_\zeta \varphi)^2] - \cos(2\vartheta) \partial_\xi \varphi \partial_\zeta \varphi \right\} = 0 \quad (\text{b.30})$$

where

$$\alpha_\vartheta \gamma = \frac{2\chi_a}{\sqrt{6}S\xi_0^2} \gamma = \frac{2(3\chi_l - S\chi_a)}{3\sqrt{6}S^2\xi_0^2}. \quad (\text{b.31})$$

This simplification reduces the integration time by a fifth and provides a significantly faster calculation but it must be realised that I am assuming a constant scalar order parameter. This limit cannot therefore be applied in situations where the scalar order parameter is varying such as in regions of strong bending of the director field. Thus it is only suitable for low applied fields.

B.2 MATLAB Electric Field and Potential Calculations

```
% POTENTIAL returns nx*(nz+2) matrices for the potential and electric
field components %
% usage: [phi,Exi,Ezeta] = potential (B, V, nx, nz)
% B: Aspect ratio; Beta, of the cavity
% V: row vector of nx elements describing the light-induced potential
% at the lower boundary
% nx: number of points in x-direction
% nz: number of points in z-direction
% Returns:
% phi: nx*(nz+2) matrix of 2D slice of potential across cell
% Exi: nx*(nz+2) matrix of 2D slice of Electric Field x component
across cell
% Ezeta: nx*(nz+2) matrix of 2D slice of Electric Field z component
across cell
function [phi,Exi,Ezeta] = potential (beta, V, nx, nz)
% Value of n to perform summation over. Will sum from -n to n. Low
values (n=1..5 n=4;
% Initialise matrices to store potential, Ex and Ez to speed up index
allocation

phi = zeros(nx,nz+2);
Exi = zeros(nx,nz+2);
Ezeta = zeros(nx,nz+2);
% Setup coordinate and normalised coordinate systems in x and z
directions
l = 0:nx-1;
xi = l'/nx;
j = 0:(nz+1);
% Translates zeta onto Gauss-Lobatto grid
zeta = 0.5*( 1 - cos( j*pi/(nz+1) ) );
% Compute the n=0 term
% b0 = quad(@B_0func,0,1,tol,trace,V,xi);
b = mean(V);
a = zeta*b;
% Compute the first term of the potential and of the electric field.
phi = a(ones(1,nx),:);
```

```
Ezeta = -b*ones(nx,nz+2);
% Compute the higher order terms.
for k = 1:n
b = mean(V' .* exp(-1i*2*pi*k*xi))/sinh(2*pi*k/beta);
a = b*sinh(2*pi*k*zeta/beta);
phi = phi + 2*real(exp(1i*2*pi*k*xi)*a);
Exi = Exi + 4*pi*imag(k*exp(1i*2*pi*k*xi)*a);
Ezeta = Ezeta + ...
4*pi*k/beta*real(b*exp(1i*2*pi*k*xi)*cosh(2*pi*k*zeta/beta));
end
```

References

- [1]. P. Planer, *Ann.*, **118**, (1861), 25
- [2]. W. Löbisch, *Ber*, **5**, (1872), 513
- [3]. B. Rayman, *Bull. Soc. Chim. (Paris)*, **47**, (1887), 898
- [4]. F. Reinitzer, *Monatshefte für Chemie*, **9** (1888), 421-441
- [5]. O. Lehmann, *Zeitschrift für Physikalische Chemie*, **4** (1889), 462-472
- [6]. L. Gatterman and A. Ritschke, *Berichte der Deutschen Chemischen Gesellschaft*, **23** (1890), 1738-1750
- [7]. G. Friedel, *Annales de Physique*, **18** (1922), 272-474
- [8]. F.C. Frank, *Discussions of the Faraday Society*, **25** (1958), 19-28
- [9]. C.W. Oseen, *Transactions of the Faraday Society*, **29** (1933), 883-900
- [10]. W. Maier and A. Saupe, *Zeitschrift Naturforschung*, **13a** (1958), 564-566
- [11]. P.G.De-Gennes, *Mol. Crys. Liq. Crys.*, **12** (1971), 193-214
- [12]. G.H.Brown and W.G.Shaw, *Chemical Reviews*, **57** (1957), 1049-1157
- [13]. R. Williams, *Journal of Chemical Physics*, **39** (1963) 384-388
- [14]. H. Kelker and B. Scheurle, *Angewandte Chemie – International Edition*, **8** (1969), 884-885
- [15]. M.Schadt and W. Helfrich, *Appl. Phys. Lett.*, **18** (1971), 127-128
- [16]. P.J. Collings and M.Hird, *Introduction to liquid crystals: Chemistry and Physics*, Taylor and Francis, London, 1997
- [17]. P.G. De-Gennes and J.Prost, *The Physics of Liquid Crystals (2nd Ed)*, Oxford University Press, New York, 1993
- [18]. P. Yeh, C. Gu, *Optics of liquid Crystal Displays*, John Wiley and Sons, New York, 1999
- [19]. L. Solymar, D.J. Webb, A. Grunnet-Jepsen, *The Physics and Applications of Photorefractive Materials (Oxford Series in Optical & Imaging Sciences)*, Oxford University Press, USA, 1996
- [20]. P. Gunter and J.P. Huignard, *Photorefractive Materials and Their Applications I: Basic Effects (Springer series in optical sciences)*, Springer, 2006

-
- [21]. I.C. Khoo, B.D. Guenther, M.V. Wood, P. Chen, M-Y. Shih, *Opt. Lett.*, **22** (1997), 1229
- [22]. I.C. Khoo, S. Slussarenko, B.D. Guenther, M-Y. Shih, P. Chen, W.V. Wood, *Opt. Lett.* **23** (1998), 253
- [23]. E.V. Rudenko, A.V. Sukhov, *Sov. Phys. JETP*, **105** (1994), 1621
- [24]. F. Simoni, O. Francescangeli, *J. Phys: Condens. Mat.* **11**,(1999), R439
- [25]. C. Cipparrone, A. Mazzulla, F. Simoni, *Opt. Lett.* **23**, (1998), 1505
- [26]. S. Bartkiewicz, A.Miniewicz, F.Kajzar, M.Zagorska, *Mol. Cryst. Liq. Cryst.* **322** (1998), 9
- [27]. S. Bartkiewicz, A. Miniewicz, F. Kajzar, M. Zagorska, *Appl. Opt.* **37** (1998), 6871
- [28]. S. Bartkiewicz, K. Matczyszyn, A. Miniewicz, F. Kajzar, *Opt. Comm.* **187** (2001), 257
- [29]. A. Ashkin et al., *Appl. Phys. Lett.*, **9** (1966), 72–74.
- [30]. H.J. Eichler, *Optica Acta*, **24** (1977), 631-642
- [31]. I.C. Khoo, H. Li, Y. Liang, *Opt. Lett.*, **19** (1994), 1723-1725
- [32]. E.V. Rudenko, A.V. Sukhov, *J. Exp. Theor. Phys. Lett.*, **59** (1994), 142-146
- [33]. J. Zhang, V. Ostroverkhov, K.D. Singer, V. Reshetnyak, Y. Reznikov, *Opt. Lett.* **25**, (2000), 414
- [34]. J. Mun, Ch-S. Yoon, H-W. Kim, S-A. Choi, J-D. Kim, *Appl. Phys. Lett.*, **79** (2001), 1933
- [35]. I.C. Khoo, M-Y. Shih, A. Shishido, P.H. Chen, M.V. Wood, *Opt. Mat.* **18** (2001), 85
- [36]. G.P. Wiederrecht, B.A. Yoon, M.R. Wasielewski, *Science* **270** (1995), 1794
- [37]. M. Kaczmarek, M-Y. Shih, R.S. Cudney, I.C. Khoo, *IEEE J. Quant. Electron.* **38** (2002) , 451
- [38]. F. Kajzar, S. Bartkiewicz and A. Miniewicz, *Appl. Phys. Lett*, **74** (1999), 2924
- [39]. P. Pagliusi and G. Cipparrone, *Appl. Phys. Lett.*, **80** (2002), 168–170
- [40]. P. Pagliusi and G. Cipparrone, *J. Appl. Phys.*, **92** (2002), 4863–4869
- [41]. P. Pagliusi and G. Cipparrone, *Phys. Rev. E.*, **69** (2004) ,061708
- [42]. S.S. Slussarenko, *Europhys. Lett.* **56** (2001), 672-675
- [43]. I.C. Khoo, *IEEE Journal of Quantum Electronics*, **32** (1996), 525-534
- [44]. G. Zhang, G. Montemezzani, P. Günter, *J. Appl. Phys.*, **88** (2000), 1-9
- [45]. P. Pagliusi and G. Cipparrone, *Opt. Lett.*, **28** (2003), 2369-2371

-
- [46]. P. Pagliusi and G. Cipparrone, *J. Appl. Phys.*, **93** (2003), 9116–9122.
- [47]. H. Ono and N. Kawatsuki, *Appl. Phys. Lett.*, **71** (1997), 1162
- [48]. M. Kaczmarek et al., *J. Appl. Phys.*, **96** (2004), 2616–2623.
- [49]. M. Kaczmarek, R.S. Cudney, S.A. Tatarkova, *Nonlinear Optics*, **27** (2001), 331
- [50]. M. Kaczmarek and A. Dyadyusha, *Proceedings of SPIE*, **19** (2004), 5518
- [51]. N.V. Tabiryian and C. Umeton, *JOSA B*, **15** (1998), 1912-1917,
- [52]. M. Kaczmarek, A. Dyadyusha, *Journal of Nonlinear Optical Physics & Materials*, **12**, (2003) 547
- [53]. V. Boichuk et. al, *J. Appl. Phys.*, **90** (2001), 5963-5967
- [54]. A. Dyadyusha, M. Kaczmarek, G. Gilchrist, *Mol. Cryst. Liq. Cryst.*, **446** (2006), 261-272
- [55]. A. Dyadyusha, M. Kaczmarek, G. Gilchrist, G. D'Alessandro, J. Parka, R. Dabrowski, *Proceedings of SPIE*, **5621** (2004), 133
- [56]. W.E. Moerner et al., *Chem. Phys. Lett.* **291**, (1998) 553-561
- [57]. A. Sugimara et al., *Phys. Rev. B*, **43** (1991), 8272
- [58]. T.J. Scheffer and J. Nehring, *J. Appl. Phys*, **48** (1977), 1783–1792.
- [59]. K. Han et al., *Jpn. J. Appl. Phys. Part 2* **32** (1993), 147–157.
- [60]. M. Cuminal and M. Brunet, *Liquid Crystals*, **22** (1997), 185-192
- [61]. G. Baur, V. Wittwer, D.W. Berreman, *Physics Letters*, **56A** (1976),142-144
- [62]. M. Francon, *Handbuch der physik xxiv*, Berlin.
- [63]. H. Ong, *J. Appl. Phys*, **71** (1992), 140–144.
- [64]. G.D'Alessandro, *Personal communication*, 2004.
- [65]. J.S. Gwag et al., *J. Appl. Phys*, **93** (2003), 4936–4938.
- [66]. J. Parka, R. Dabrowski, *Institute of Technical Physics*, MUT University, Warsaw, Poland
- [67]. De Filpo, *J. Appl. Phys.*, **84**, (1998), 3581-3585
- [68]. F. Yang and J.R. Sambles, *J. Opt. Soc. Am. B*, **10** (1993), 858-866
- [69]. F. Yang and J.R. Sambles, *J. Opt. Soc. Am. B*, **16** (1999), 488-197
- [70]. B.T. Hallam and J.R. Sambles, *Phys. Rev. E*, **61** (2000), 6699-6704
- [71]. O D Lavrentovich, *Pramana, Journal of Physics*, **61** (2003), 373-384
- [72]. A.Sonnet, A.Kilian, and S.Hess, *Phys. Rev. E*, **52** (1995), 718–722.
- [73]. R. Barberi et al., *Eur. Phys. J. E* **13** (2004), 61–71.
- [74]. H.Coles, *Mol. Cryst. Liq. Cryst. Lett.* **49** (1978), 67–74.

-
- [75]. A. Walczak, *Proc. International Workshop on Liquid Crystals for Photonics*, P-25 (2006), Ghent, Belgium
- [76]. G.G. H.-W. Speiss, V. Vill, D. Demus and J. Goodby, *Physical properties of liquid crystals*, Wiley-VCH, Weinheim, 1999.

List Of Publications

- [1]. A. Dyadyusha, M. Kaczmarek, **G. Gilchrist**, G. D'Alessandro, J. Parka, R. Dabrowski, *Proceedings of SPIE*, **133** (2004), 5621
- [2]. A. Dyadyusha, M. Kaczmarek, **G. Gilchrist**, G. D'Alessandro, *Proceedings of SPIE*, Optics & Photonics, 31 July - 4 August 2005, San Diego, California USA
- [3]. Andriy Dyadyusha, Malgosia Kaczmarek, **Graham Gilchrist**, *Surface screening layers and dynamics of energy transfer in photosensitive polymer-liquid crystal structures*, *Mol. Cryst. Liq. Cryst.*, **446** (2006), 261-272

List of Presentations

- [4]. **G. Gilchrist** (Presenter), M. Kaczmarek, A. Dyadyusha, G. D'Alessandro, *Spatially non-uniform director profiles in liquid crystal-polymer structures*, International liquid crystal conference, Poster presentation (July 2006)
- [5]. **G. Gilchrist** (Presenter), M. Kaczmarek, A. Dyadyusha, G. D'Alessandro, *Spatially non-uniform director profiles in liquid crystal-polymer structures*, British liquid crystal society conference, Poster presentation (May 2006)
- [6]. M. Kaczmarek, A. Dyadyusha, G. D'Alessandro, **G. Gilchrist**, *The role of photoconductivity in two-beam coupling in liquid crystal-polymer structures*, European Liquid Crystal Conference, Italy 2005
- [7]. M. Kaczmarek, A. Dyadyusha, G. D'Alessandro, P. Smith, J. Baumberg, **G. Gilchrist**, *Adaptive liquid crystal systems for switching and sensing applications*, 7th Mediterranean workshop and topical meeting "Novel Optical Materials and Applications", Italy 2005

-
- [8]. M. Kaczmarek, A. Dyadyusha, G. D'Alessandro, **G. Gilchrist**, *Surface induced and photosensitive effects in liquid crystals*, 8th International conference on frontiers of polymers and advanced materials, Mexico 2005
- [9]. M. Kaczmarek, A. Dyadyusha, **G. Gilchrist**, G. D'Alessandro, I. Sparrow, P. Smith, J. Baumberg, *Surface microstructuring for tunable and adaptive liquid crystal systems*, XVI Conference on liquid crystals, Poland 2005
- [10]. A. Dyadyusha, M. Kaczmarek, **G. Gilchrist**, *Dynamics of reorientation and two-beam coupling in photosensitive polymer-liquid crystal structures*, British liquid crystal conference 2005
- [11]. **G. Gilchrist** (Presenter), M. Kaczmarek, A. Dyadyusha, G. D'Alessandro, *Surface charge Fields and reorientation in liquid crystal-polymer structures*, Physics 05: A century after Einstein, Poster presentation (April 2005)
- [12]. M. Kaczmarek, A. Dyadyusha, **G. Gilchrist**, G. D'Alessandro, O. Buchnev, Y. Reznikov, *Liquid crystals hybrid structures with improved optical response*, International symposium on materials and devices for nonlinear optics, Ireland 2005

Surface Screening Layers and Dynamics of Energy Transfer in Photosensitive Polymer-Liquid Crystal Structures

Andriy Dyadyusha
Malgosia Kaczmarek
Graham Gilchrist

School of Physics and Astronomy, University of Southampton,
United Kingdom

The dynamics of energy transfer in photoconductive polymer liquid crystal structures can contain important information on interface effects and surface electric fields contributing to the strength of liquid crystal reorientation gratings. The characteristic, transient effects observed during switching on and off of incident light or electric field can be explained by the presence of surface screening layers. Screening layers play an important role in the reorientation of liquid crystal director in cells with different alignment layers. Strong screening of external DC field is present not only in cells with a photoconductive polymer (56 V), but in standard cells with thicker (0.3 μm) polyimide, aligning layers.

Keywords: nematic liquid crystals; photoconductive polymers; surface-charge field; two-beam coupling

INTRODUCTION

The process of asymmetric energy transfer via two-beam coupling was studied in different liquid crystal systems, but the most promising results were achieved in liquid crystals doped with dyes (or fullerenes) and in liquid crystal-photosensitive polymer structures. In particular, light amplification in hybrid, photorefractive material-liquid crystal

We would like to thank G. D'Alessandro for his contribution and help with theoretical modeling; R. W. Eason and I. C. Khoo for helpful discussions and advice regarding this work. We acknowledge the financial support of the Engineering and Physical Sciences Research Council (EPSRC) under grant number GR/R27235.

Address correspondence to Andriy Dyadyusha, School of Physics and Astronomy, University of Southampton, SO17 1BJ, United Kingdom. E-mail: andriy@phys.soton.ac.uk

systems can be used for optical addressing in light valves and spatial light modulators [1,2]. While achieving high gain is of considerable interest, the two-beam coupling process can also provide an important insight into the nature and mechanism involved in the reorientation of liquid crystal director under the influence of electric field and light.

I.C. Khoo and co-workers [3] reported very high gain in 5CB liquid crystal doped with C_{60} , which expressed in terms of exponential gain (also called gain coefficient or coupling coefficient) was of the order of 3000 cm^{-1} . Further experiments in similar systems by Zhang *et al.* showed [4] gain of 500 cm^{-1} , while those carried out by Mun and his group [5], gain of 90 cm^{-1} .

Dyes, such as Rhodamine 6G or Methyl Red, dissolved in liquid crystals, such as 5CB, were also used to study nonlinear effects and two-beam coupling. Wiederrecht *et al.* [6] reported exponential gain of the order of 600 cm^{-1} . High nonlinearity and strong electric space-charge field is evidently present in dye doped systems – as demonstrated by, for example, high diffraction efficiencies [7] or large intensity dependent refractive index changes [8].

The other type of structure that was widely used for amplification of light via two-beam coupling is a hybrid liquid crystal-polymer system. It is, typically, based on a photorefractive polymer, poly-vinylcarbazole (PVK) doped with sensitizers such as TNF or C_{60} and used as alignment layer or as an intermediate layer, between an ITO electrode and aligning material. By doping PVK with sensitizers, its photoconductivity can be increased and shifted from the UV to the visible. High exponential gain was measured by Bartkiewicz and Kajzar in such systems [9,10], namely as high as 3700 cm^{-1} . In similar systems other groups also reported gain [5] of 220 cm^{-1} and 48 cm^{-1} – measured by Ono and his group [11].

In liquid crystals, the formation of a two-beam coupling grating relies on an electric field induced reorientation grating that leads to refractive index modulation. However, as the actual mechanism of the electric field build-up inside a liquid crystal-polymer cell is not clear, it is difficult to optimise the experimental conditions. This could be the reason for some differences in the data published so far on gain and diffraction efficiency. The groups that studied two-beam coupling in liquid crystal-PVK systems, also proposed different qualitative models of the mechanism involved in the formation of the electric space charge field.

Ono and co-workers [11] suggested that the space charge field is due to the generation of charges in a PVK layer. The trapping of charges takes place in an additional, insulating PVA layer, adjacent to the PVK layer. In the model suggested, PVA was essential for the

formation of space-charge field. Mun and his group [5] explored this idea further and indicated that charge photogeneration occurs in the liquid crystal bulk. They proposed that charge trapping occurs at a PVK-liquid crystal interface, so PVA layers are, in fact, not essential. While these models of the space charge field formation were quite different, they shared a common assumption, namely they were all based on a standard model of charge generation, transport and trapping, as often used in bulk, solid-state photorefractive materials. Furthermore, in both models an externally applied DC field was assumed to cause a uniform reorientation of the liquid crystal director without illumination.

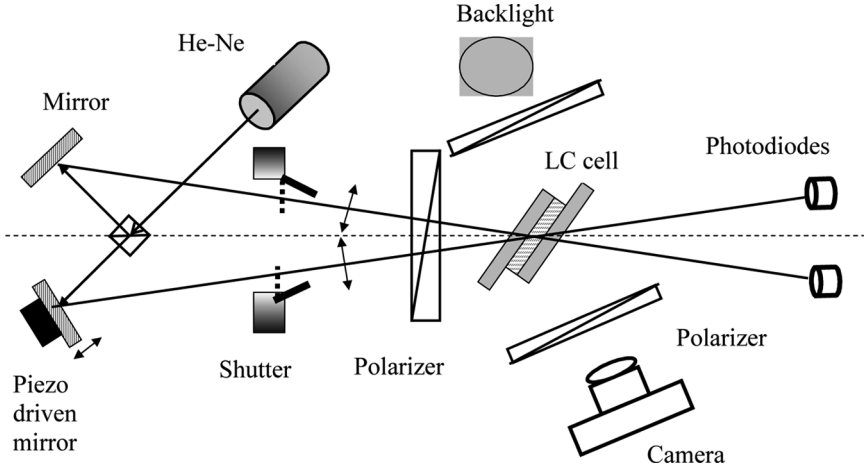
The process of liquid crystal director reorientation and two-beam coupling was also studied in liquid crystal cells with non-photoconducting polymer layers. The results of Pagliusi and co-workers [12] suggest that accumulation of charges on a liquid crystal interface is not limited to the case of photoconductive polymers.

Our own studies of liquid crystal-polymer systems [13] provided the evidence that, in fact, strong double charge layers form at the liquid crystal-photoconductive polymer interface and they are capable of screening high electric fields. In a qualitative model we proposed, the formation and discharge of a surface screening layer was key to for inducing reorientation gratings, rather than standard photorefractive processes taking place within a polymer, such as charge excitation, drift and trapping.

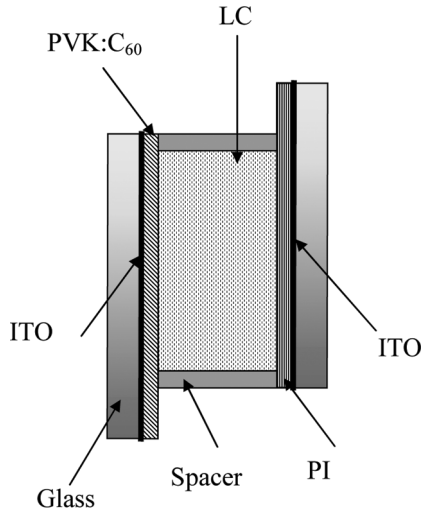
While the results of two-beam coupling gain do not provide any direct evidence for a particular mechanism involved in the formation of refractive index gratings, the difference in experimental results and qualitative explanations provided by different groups clearly indicate that more detailed studies of the role of charged dopants and surface effects are needed. Pursuing this idea, we focussed our work on two areas: first, on exploring in more detail the conditions and materials where surface charge screening is observed and secondly, on studying the dynamics of two-beam coupling process and its dependence on an applied electric field and light illumination.

EXPERIMENTAL SET-UP AND PROCEDURES

In a typical two beam coupling experiment the intensity of incident and transmitted beams, are measured. Figure 1a presents a schematic diagram of such experimental set-up. In our arrangement a liquid crystal cell was mounted on a rotation stage that could be precisely turned around the vertical axis (perpendicular to the plane containing the incident beams) at the point of intersection of the incident beams.



(a)



(b)

FIGURE 1 (a) Experimental set-up for measuring light induced reorientation and two-beam coupling gain; (b) Liquid crystal cell structure with one substrate covered with PVK:C₆₀.

Electric shutters, that blocked or unblocked the beams, as well as application of electric field, were controlled by a computer. The intensity grating, created by the interference of two, horizontally polarized,

beams (543 nm) had a spacing of either 3 or 60 μm . This experimental set-up was also used to measure the light and DC field thresholds for reorientation of liquid crystals with single beam illumination.

The structure and appearance of an illuminated spot on a sample was simultaneously monitored through second pair of polarisers and backlight and then recorded on a CCD camera. Monitoring of the illuminated area of the cell enabled us to record the dynamics and uniformity of light and electric field driven reorientation.

The liquid crystal-polymer cell structure is shown on Figure 1b. PVK doped with photosensitiser (C_{60}) was deposited as a thin and uniform layer onto ITO covered glass substrates. Both C_{60} and PVK were dissolved in chlorobenzene. Doping of PVK with C_{60} was achieved by adding a saturated concentration of C_{60} solution to the PVK solution with concentration of approximately 14.9% by weight. Polymer films were then spincoated onto clean ITO covered glass and dried at high temperature.

The substrates were unidirectionally rubbed and uniform planar alignment was achieved. Doped PVK layer was deposited only on one substrate, while the other was covered with standard polyimide (PI) as an alignment layer. All the cells were 30 μm thick and filled with pure (undoped) E7 liquid crystal mixture. A DC bias applied to the cell ITO electrodes had a negative contact applied to the PVK covered substrate.

For the study of surface charge screening, we also prepared cells with polyimide on both substrates, without any photosensitive layers. The cells had either thin, less than 0.05 μm , or thick, approximately 0.3 μm , layers of polyimide.

The experimental procedure for precise detection and measurement of two-beam coupling consisted of several steps where the incident beams were either blocked or unblocked. The value of applied DC field varied from 0 to 56 V. There are several stages of the measurement all controlled by a computer. In step one and two, the shutters were closed and then opened to let both beams through simultaneously. Then, just one beam (pump) was present, followed by a step where both beams were again illuminating a cell. Further, the shutter for the pump beam was closed and for the probe opened. Finally, both beams were let through and then both blocked. In this way, time dependence of beam intensities could be recorded and monitored and the response of the system to transient changes in incident light and applied DC field could be recorded.

For measuring the steady-state gain magnitude, the measurements were taken when steady-state values of transmitted intensities were reached and the final, returned value of intensity was taken as an

average of 600 data points. This sequence of steps could be repeated for different values of DC field, increasing from zero. The complete experimental procedure allowed us to measure gain and, at the same time, monitor the total change in beam intensities.

Using this experimental methodology two-beam coupling gain could be measured in two different ways. In the first experiment, transient beam intensities and gain was measured to observe the dynamic response of the system to fast changes of parameters, such as incident light intensity (or a DC field). In the second experiment, the steady-state values of beam intensities were recorded after relaxation of the system to a quasi-equilibrium state.

RESULTS AND DISCUSSION

Surface charge layers that form at the liquid crystal and polymer (or other aligning material) interface can strongly influence the magnitude of a DC electric field penetrating the liquid crystal bulk. In cells with PVK:C₆₀ layers, we observed that the bulk of liquid crystal could be completely screened [13] from the external electric field. In this case, strong surface charge field could completely block the external electric field, so no Freedericksz transition was observed up to 56 V (1.9 V/μm) of applied DC field. However, this threshold could be significantly reduced if the cell was illuminated by visible light. The incident beam could have low intensity, namely as low as μW/cm², to induce the transition provided its wavelength was within the visible range of spectrum, where PVK:C₆₀ is photoconductive. Figure 2 presents how the threshold voltage decreases with increasing incident light intensity up to saturation of photoconductivity. As sensitised PVK becomes highly conductive in illuminated areas, the applied electric field can reach liquid crystal bulk. The higher the incident intensity is, the more efficiently surface charge layers can be selectively annihilated and liquid crystal reoriented. Low dark conductivity of PVK – either sensitised or not – also means that patterns and gratings with resolution down to 3 μm could be written and high resolution, reorientation and refractive index patterns created in the liquid crystal. As expected, when an AC field was applied, the usual Freedericksz transition occurred with a threshold of approximately 2 V.

In standard liquid crystal cells with non-photoconducting polymer layers, the DC field threshold of reorientation was approximately ten times smaller than the one observed in our experiments. For example, cells with alignment layers made of PVA (polyvinyl alcohol) and liquid crystal E7 had the reorientation threshold [12] of 5 V.

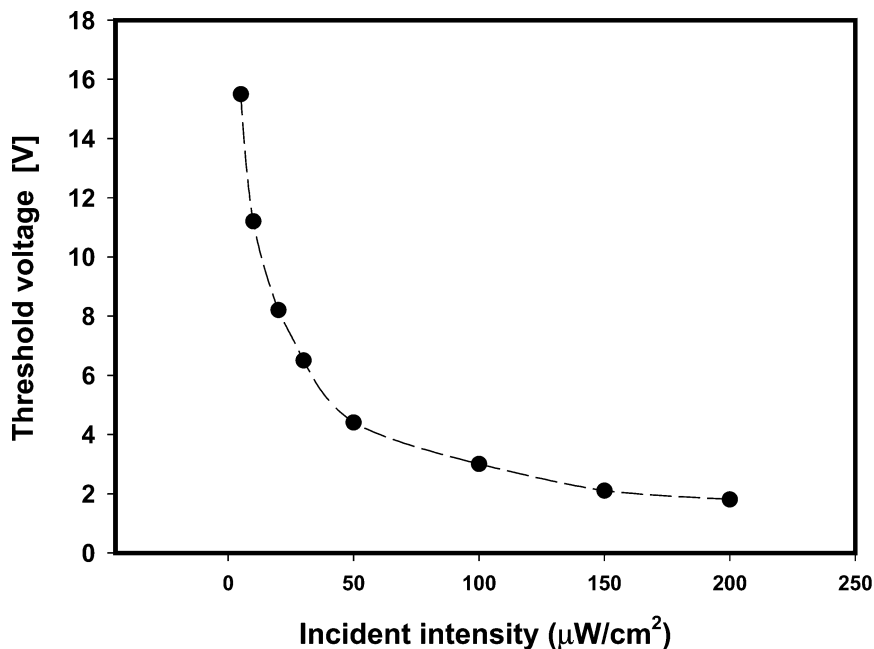


FIGURE 2 Threshold voltage of Freedericksz transition and its dependence on the incident light intensity.

While surface charge layers are particularly strong in the case of PVK, they can also develop in other types of cells. We investigated this effect in cells with polyimide aligning layers and found the evidence of strong screening. For cells with thin, less than $0.05\ \mu\text{m}$ polyimide layers the reorientation threshold was between 2 to 3 V, as expected. However, when a thicker layer of polyimide was deposited, approximately $0.3\ \mu\text{m}$, the reorientation threshold increased significantly reaching the levels of 20 V.

Further, detailed analysis of charge generation and transport between electrodes, aligning layers and liquid crystal as well as theoretical modelling is needed to optimise and to understand more fully the nature of interface effects. However, as a first step, we studied in more detail the transient response of the liquid crystal-PVK:C₆₀ system to applied light and DC field.

In particular, we compared the time evolution of both amplified and depleted beam for the two ways in which a two-beam coupling grating can be written. In the first one, both beams were unblocked and illuminated the cell at the same time (with a DC field present) and

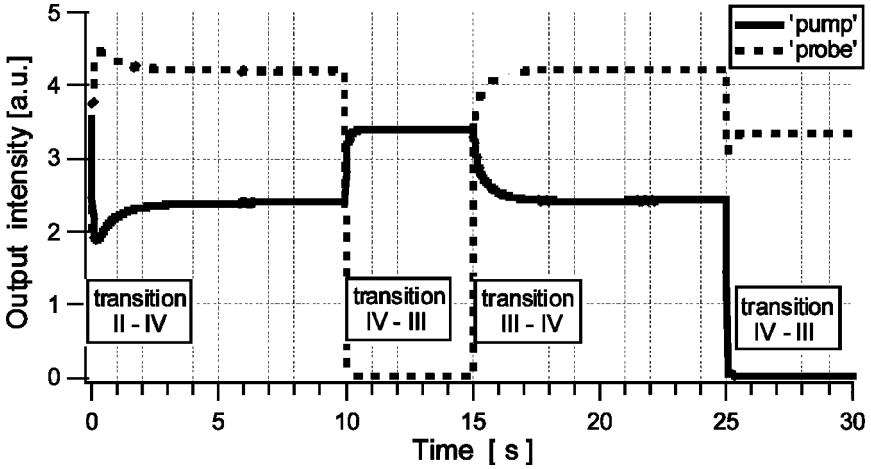


FIGURE 3 Dynamics of two-beam coupling under different illumination and applied electric field conditions.

in the second option, the two beams were unblocked in series, one after another, also with a DC field already applied to the cell. Let's call the first option "dark-to-grating" transition and the second as "bright-to-grating" transition. We systematically considered possible states of grating formation and transitions during for each option of running the two-beam coupling experiment.

We observed different dynamics of the grating build up for the two cases: in the first case, the build up is much faster with a characteristic, transient peak in amplified probe beam (and a corresponding dip in the depleted probe) followed by decay to a steady-state level. In the second case, the build up is slower, without a transient peak, as shown on Figure 3. However, the final equilibrium state and the value of gain reached in both cases was the same.

This steady-state value of gain was high, reaching approximately 500 cm^{-1} . Its magnitude was found to depend on several parameters such as the DC field – its bias, direction and value; the direction of the cell tilt with respect to the bisector between the incident beams, intensity and ratio of beam intensities, as well as the quality of the sample.

The possible equilibrium states of our system (sample) relative to ambient conditions could be identified and compared with the data on the measured intensities of beams in the two-beam coupling experiment. Those states can be labelled I to IV for clarity (as shown on Fig. 3). In the first stage (I) a sample is in a steady-state with some equilibrium distribution of the director set by the original alignment

conditions and without any externally applied field, either electrical or optical. As the sample is not illuminated, no intensities are measured. In the second stage (II) the sample remains unilluminated, but since a DC field is applied, screening charge layers develop. However, the director distribution remains as in state I. This was confirmed by investigating cell between crossed polarisers with very weak backlight and also by illuminating the cell with light of wavelength beyond the photoconductivity band of PVK:C₆₀. It is important to note that equilibrium screening charge is always supported or supplied by an external DC field and discharged via the dark conductivity of PVK. As in the previous stage, the sample is not illuminated, so beam intensities are not be measured. Further (state III), the sample is as state II but is now illuminated by one laser beam and the director reorients in illuminated areas. This state III is present only in illuminated part of the sample, unilluminated part of the sample remains in state II. Transmitted beam intensities can be measured and this state corresponds to intervals between 13–15 and 27–30 seconds on Figure 3. An alternative state (state IV) is for the sample, starting from state II, to be illuminated by two laser beams, so the director is reoriented in bright fringes. This state (state IV) corresponds to intervals 8–10 and 23–25 seconds on Figure 3. State IV is also present only in the part of the sample illuminated with intensity pattern and, with certain approximation, is a combination of states II and III (dark and bright fringes, correspondingly).

The transitions from one state to another and the behaviour of coupled beams could be explained qualitatively using the model of surface charge layers and their selective annihilation. Let us consider the sample in state I, namely without illumination. According to our model, after applying an external DC bias, surface screening charges accumulate near the PVK:C₆₀ surface and that reduces the potential applied to the liquid crystal layer to the level below the Fredericksz transition.

If the cell is now illuminated, then in bright areas, screening field is reduced or discharged completely. This causes the reorientation of the liquid crystal director by the superposition of an external DC field and the remaining screening field. After some transition period, state III is reached.

Now let's consider the two possible transitions leading to state IV. The first way is "dark-to-grating" transition, corresponding to state II to state IV transition, and the second way is "bright-to-grating" transition, equivalent to state III to IV transition.

As indicated above, there is a clear difference in evolution of amplified and depleted beams for the two cases and we propose a qualitative

explanation for this effect. For the case of state II to IV transition, the sample in state II is illuminated by the interference pattern produced by two laser beams, so the surface charge is discharged in bright fringes and the director is reoriented, following the pattern of bright and dark fringes. There are two important parameters contributing to the speed and strength of reorientation and refractive index gratings. These parameters are the relaxation time of photoconductivity of PVK:C₆₀ and the response time of liquid crystal. The peak and strong maximum in the amplified signal could be explained by the fast discharge of surface layers and subsequent sudden application of the DC field, sensed by the liquid crystal bulk. Strong, but transient gain suggests more pronounced, initial director reorientation followed by its relaxation towards the original state. The contribution from additional, transient current going through the cell at the moment of discharge could also contribute to this peak in amplification. This transition corresponds to interval 0 to 5 seconds (Fig. 3).

For the case of state III to IV transition, the illumination conditions only change from a uniform (Gaussian beam) to an interference field of two laser beams. The situation is different – the uniformly illuminated area with discharged surface screening layers is replaced by a modulated pattern of dark and bright fringes. As a result, the process of recharging in dark fringes takes place and the director reorientation follows the changes in the modulated electric field profile. In this case, the intensities of both amplified and depleted beams change smoothly with time, exponentially approaching the equilibrium, steady-state value reached in state III. This process is much slower than the first transition and there are two processes that could be responsible. First, the formation of the surface charge layers requires time to develop; a process that is limited by the conductivity of liquid crystal, substrates as well as by the presence of impurities or ions in the liquid crystal bulk. Secondly, when a uniform illuminated spot is replaced by an interference pattern, it takes time for photoconductivity to decay in the dark fringes. Limited value of photoconductivity means that surface charge will not be discharged instantly. This transition corresponds to the time interval 15–20 seconds (Fig. 3). The reverse transition from the state IV to III takes place when one of the two beams is closed and the grating decays to the uniformly reoriented state due to discharge of the screening layers in the previously dark places. This case corresponds to time intervals 10–13 and 25–27 seconds (Fig. 3).

Figure 4 presents a photograph of most relevant states of the sample (I–IV). In order to illustrate better the lack of reorientation with a DC field applied, but without illumination, a 200 μm wire was placed

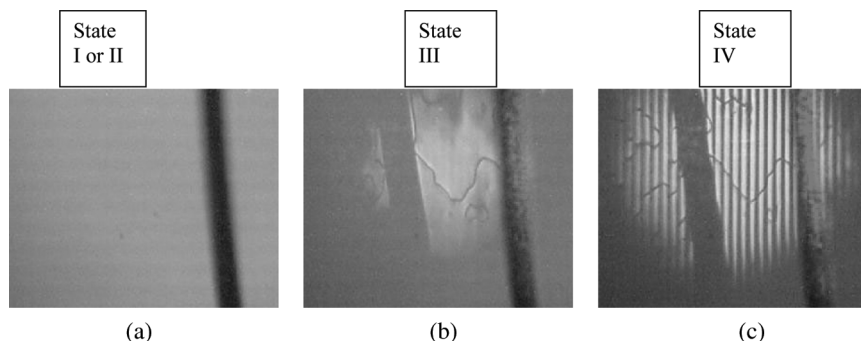


FIGURE 4 Demonstration of selective reorientation of liquid crystals in a cell with an applied DC field. A $200\ \mu\text{m}$ wire is placed in front of the cell to help to illustrate the effect. (a) without illumination no reorientation occurs; (b) illumination by a single beam-liquid crystals get reoriented except in the area where light is blocked by the wire illuminated by one beam; (c) an interference pattern is incident on the cell and high resolution, $50\ \mu\text{m}$, reorientation grating is recorded, apart from the region that is behind the wire. (See COLOR PLATE XVI)

in front of the cell (Fig. 4a). Figure 4b shows the case of uniformly reoriented area, where a single beam was incident on a cell, except in the area behind the wire. For the case of incident interference pattern (Fig. 4c) with $50\ \mu\text{m}$ spacing, high contrast reoriented grating is clearly visible.

CONCLUSIONS

In conclusion, we reported and analysed the characteristic features and dynamics of light and electric field induced two-beam coupling process in cells with alignment layers made of PVK doped with fullerene (C_{60}) as a photosensitizer. The time evolution of amplified and depleted beams for the different DC field and illumination conditions support the idea that selective discharge of strong, surface charge layers plays an important role in efficient reorientation gratings in the bulk of the liquid crystal.

There is a strong dependence of Freedericksz transition threshold on the incident light intensity. The Freedericksz transition threshold (without illumination) is very high (56 V) for cells with PVK: C_{60} . However, liquid crystal cells with non-photoconductive, but thicker polyimide layers, this threshold can reach 20 V. Surface screening layers can clearly be present in a wide variety of different cell design

and materials. They can be regarded as “command” layers and allow a flexible control of diffraction and energy transfer in liquid crystal cells.

REFERENCES

- [1] Brignon, A., Bongrand, I., Loiseaux, B., & Huignard, J.-P. (1997). *Opt. Lett.*, *24*, 1855.
- [2] Kajzar, F., Bartkiewicz, S., & Miniewicz, A. (1999). *Appl. Phys. Lett.*, *74*, 2924.
- [3] Khoo, I. C., Guenther, B. D., Wood, M. V., Chen, P., & Shih, M. Y. (1997). *Opt. Lett.*, *22*, 1229.
- [4] Zhang, J., Ostroverkhov, V., Singer, K. D., Reshetnyak, V., & Reznikov, Yu. (2000). *Opt. Lett.*, *25*, 414.
- [5] Mun, J., Yoon, Ch.-S., Kim, H.-W., Choi, S.-A., & Kim, J.-D. (2001). *Appl. Phys. Lett.*, *79*, 1933.
- [6] Wiederrecht, G. P., Yoon, B. A., & Wasielewski, M. R. (1995). *Science*, *270*, 1794.
- [7] Khoo, I. C., Slussarenko, S., Guenther, B. D., Shih, M. Y., Chen, P., & Wood, W. V. (1998). *Opt. Lett.*, *23*, 253.
- [8] Khoo, I. C., Shih, M. Y., Shishido, A., Chen, P. H., & Wood, M. V. (2001). *Opt. Mat.*, *18*, 85.
- [9] Bartkiewicz, S., Matczyszyn, K., Miniewicz, A., & Kajzar, F. (2001). *Opt. Comm.*, *187*, 257.
- [10] Kajzar, F., Bartkiewicz, S., & Miniewicz, A. (1999). *Appl. Phys. Lett.*, *74*, 2924.
- [11] Ono, H. & Kawatsuki, N. (1997). *Appl. Phys. Lett.*, *71*, 1162.
- [12] Pagliusi, P. & Cipparrone, G. (2002). *Appl. Phys. Lett.*, *80*, 168.
- [13] Kaczmarek, M., Dyadyusha, A., Slussarenko, S., & Khoo, I. C. (2004). *J. Appl. Phys.*, *96*, 2616.

Photoconductive polymer-liquid crystal systems for efficient beam control and amplification

A. Dyadyusha, M. Kaczmarek, G. Gilchrist, G. D'Alessandro*

School of Physics and Astronomy, University of Southampton, Southampton SO17 1BJ, UK

*School of Mathematics, University of Southampton, Southampton SO17 1BJ, UK

ABSTRACT

We report on reorientation and two-beam coupling process in liquid crystal cells with different aligning polymer layers. Polymers such as poly(N-vinyl carbazole), pure and doped with fullerenes as well as standard polyimide layers were considered. Electric field distribution inside a liquid crystal cell was modelled and different penetration depths into the liquid crystal bulk were calculated depending on the modulation of surface electric field. The characteristics features of reorientation process were studied via measurements of capacitance with an increasing DC field. The evidence of strong screening was found in cells with photoconducting polymers, as well as in those with thicker polyimide layers. Surface screening layers could be discharged by illuminating a cell with light to induce selective reorientation of a liquid crystal director.

Keywords: liquid crystals, photoconductive polymer, surface-charge field, two-beam coupling

1. INTRODUCTION

Adaptive and reliable control of liquid crystal alignment via surface modifications or via confined geometries can be a powerful tool in nanotechnology and organic photonics. Surface and interface effects between liquid crystals and polymers can be critical in determining the alignment and reorientation of the liquid crystal director as well as in enhancing the nonlinear effects¹. For example, in hybrid photoconductive polymer-liquid crystal structures electrical and optical functionality can be achieved via modifications of surface effects. Photoconductive properties of polymers in such hybrid systems can play a vital role in efficient, light-induced reorientation of liquid crystals and their photorefractive response. In particular, photorefractivity can be enhanced if either liquid crystals and polymers (or both materials) are doped with dyes or other sensitizers, such as for example, C₆₀. One of the most efficient photosensitive polymers proved to be poly(N-vinyl carbazole) (PVK). Sensitizers, such as C₆₀ or TNF, were typically used as dopants to move PVK sensitivity to the visible range of spectrum and increase its conductivity. PVK doped with photosensitizer trinitrofluorene (TNF) showed very high coupling coefficients² in two-beam coupling geometry.

Diffraction efficiency and two-beam coupling gain are the two, most commonly used methods to assess the strength of liquid crystal reorientation gratings. Two-beam coupling experiments in liquid crystal cells typically operate in the Raman-Nath (thin) grating regime and as a result several diffraction orders of the beams are observed. One of the experimental challenges is, therefore, to ensure the correct measurement of net gain by carefully separating effects originating from beam coupling and diffraction³. The magnitude of two-beam coupling can be both induced and controlled by light and electric field, as well as by cell and experimental geometry. Modulation of liquid crystal director orientation can lead to two-beam coupling provided it is non-local with respect to the incident light intensity patterns. For PVK-liquid crystal system, it was suggested that space-charge field generated in PVK was the main mechanism responsible for this process^{2,4,6}. However, our experiments indicate that surface electric field that develops on the liquid crystal-polymer interface can strongly drive liquid crystal reorientation.

When a DC field is applied to a PVK-liquid crystal cell, surface charges accumulate on a liquid crystal-polymer interface and they can completely screen the liquid crystal bulk from an external electric field. As a result, surface electric field can control dynamic grating writing or beam coupling.

In order to characterise in more detail the optical and electrical response of polymer-liquid crystal structures, further measurements, beyond diffraction efficiency and two-beam coupling had to be carried out. In this paper we present the results of experimental and theoretical studies of surface electric field and its effect on reorientation and two-beam coupling. In particular, we focussed on the measurements of capacitance measurements, the threshold of reorientation and on the theoretical analysis to produce maps of electric field penetration into the liquid crystal bulk.

2. PHOTOCONDUCTIVE POLYMER-LIQUID CRYSTAL SYSTEMS

2.1 Cell design and materials

The cells used in our experimental had two parallel, ITO covered, glass substrates with 30 μ m thick spacers between them. The two substrates were covered with different polymer layers. The first substrate (onto which laser beams were incident) had PVK:C₆₀ layer. This layer served as an alignment layer and, at the same time, a photoconductor responsible for the efficient photorefractive response of the whole system. C₆₀ and PVK were separately dissolved in chlorobenzene. Doping of PVK with C₆₀ was achieved by adding a saturated concentration of C₆₀ solution to the PVK solution. Calculated concentration of C₆₀ in dry PVK layer was approximately 14.9% by weight. Polymer was spincoated onto clean ITO covered glass, dried at high temperature to form a thin, 0.1 μ m, layer. It was then unidirectionally rubbed to promote uniform planar liquid crystal alignment. The second substrate was covered with standard polyimide (PI) as an alignment layer. Each cell was assembled with rubbing directions of opposite substrates being at right angles. This was essential to get a uniform, planar structure in the whole cell due to different alignment properties of PI and PVK. PI promotes an easy axis of liquid crystal alignment along a rubbing direction with a small pretilt angle between 3-5°. However, PVK promotes an easy axis orthogonal to the rubbing direction with a zero pretilt angle. Cells prepared in this way were then filled with liquid crystal E7.

PVK significantly modifies the operation and the threshold of reorientation under applied DC field. Pure, undoped PVK is an insulator in the visible, showing very low conductivity. It becomes photoconductive when illuminated by UV light⁵. Its photosensitivity⁶ can be improved further by doping with trinitrofluorene (TNF) or C₆₀. These sensitizers also shift the absorption of PVK into the visible band.

2.2 Photorefractive effect in liquid crystal-polymer structures

Liquid crystal cells with PVK:C₆₀ layers have certain characteristic response to an externally applied DC field. Due to PVK photoconductivity, electric potential on the liquid crystal-polymer interface can be modulated. The basic mechanism creating a modulated potential is based on surface screening field⁷. Surface charge field builds up from the combination of an external DC field and photoconductivity of PVK:C₆₀ layer. When an external DC is applied, a screening charge layer forms near the PVK:C₆₀ layer. Its screening field can reduce the effective electric field sensed by the liquid crystal bulk to the level below the Freedericksz transition threshold. As the reorientation of liquid crystal molecules will follow that modulation pattern, the Freedericksz transition will not be observed unless the cell is illuminated by, for example, light interference pattern. In light fringes, the surface charge layer can be discharged and in dark fringes it remains. Hence, the interference pattern can create regions of reoriented liquid crystal director next to the regions of unperturbed, original orientation of the director.

As drift or diffusion processes in PVK do not contribute significantly to the liquid crystal reorientation grating, the induced refractive index grating remains local with respect to the intensity grating. However, due to the complex structure and deformations involved in reorientation, the induced space charge field has two-dimensional dependence. While it is localised near the PVK:C₆₀ surface, it is also coupled with the director field and dependent on the number of parameters such as an external DC field, light intensity and experimental geometry. In our experiments two-beam coupling gain was only observed when a cell was tilted so the bisector between the two incident beams was not along the cell normal. Moreover, it was essential to apply DC field. Namely no energy exchange between the beams was observed without externally applied electric field. The second substrate was not photoconductive or photosensitive and there was no photoinduced modulation of potential near that surface.

Two-beam coupling effect could be observed for different alignment of liquid crystal cells provided the incident beams remained p-polarized. Two possible directions of liquid crystal director were investigated, namely with original (before application of an external electric field or illumination) director being either parallel or orthogonal to the plane of incidence that contained both incident beams. In the former case, the director was parallel to the grating vector of induced refractive index grating, in the later orthogonal to it. As a result, different deformations of the director field were involved in creating induced, reorientational refractive index grating. Figure 1 presents the two configurations where gain could be observed. No gain was observed for s-polarised beams, irrespective of liquid crystal director orientation.

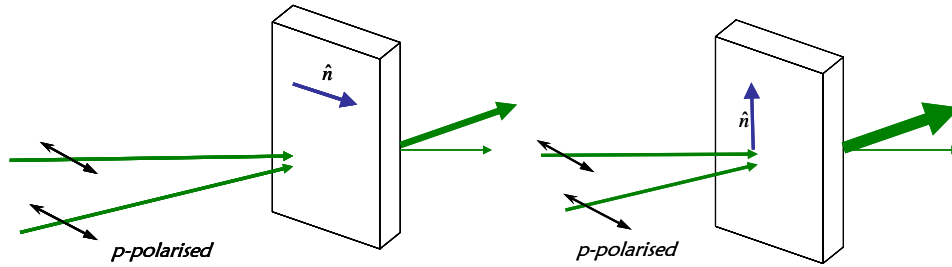


Figure 1 Experimental geometry for observing two-beam coupling gain in PVK:C60-liquid crystal cells

The qualitative description and model we developed for two-beam coupling in liquid crystal-photoconductive polymer systems and their parameters was the first step in gaining a better understanding of photorefractive and photoconductive phenomena taking place at polymer-liquid crystal interfaces. Two-beam coupling in various liquid crystal-polymer systems^{2,4,6,8,9} was usually explained via orientational gratings that form as a result of spatially modulated electric field inside a liquid crystal cell. The profile and strength of such electric field modulation was a result of an externally applied (uniform) electric field and, specific for a particular dopant or polymer, light-induced processes. We observed that in the case of PVK-liquid crystal systems, large photoconductivity and low dark conductivity of PVK played far more substantial role in two-beam coupling process than photorefractive properties of PVK.

Further modeling of electric field and director profile was needed not only to gain better understanding of surface effects in liquid crystal-polymer interfaces, but also to optimize experimental parameters, such as cell thickness or grating spacing.

3. THEORETICAL MODELLING

We have performed simulations to determine the director field profile for three different grating periods and for increasing applied electric field. One period of the electric field modulation was simulated on a two dimensional Gauss-Lobatto grid, in which the points become more closely spaced toward the surfaces. In order to consider three dimensional reorientation, a Cartesian coordinate system with three axes was used. The z-axis represented the direction along the liquid crystal layer of thickness L_z with the liquid crystal-polymer interfaces at $z = 0$ and $z = L_z$. The x and y axes were parallel to the substrate planes, with the x axis parallel to the grating vector and the y-axis perpendicular to the grating vector. The periodic structure is assumed to repeat infinitely along the x-axis with $x_0 = x_{L_x}$ where L_x is the grating period.

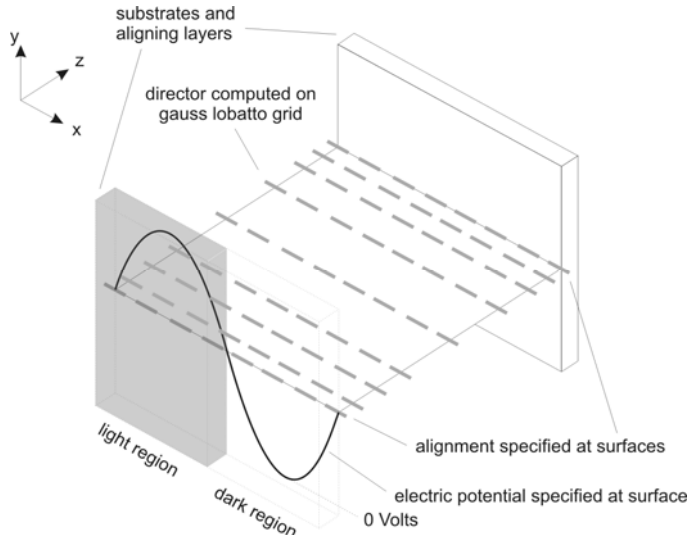


Figure 2 Schematic diagram of a cell and coordinates used in modelling

Boundary conditions were specified in the form of the rigid alignment of the director and the electric potential at both interfaces. Each is specified as a function of x . It was assumed that the electric potential at the first, input interface followed the shape of the surface charge modulation and therefore the electric field at this boundary could be assumed to have the form of a \sin^2 function. The electric potential at the second substrate was set to 0 Volts.

We then considered the alignment of a liquid crystal confined in a planar cell. The director field was represented using a 3×3 traceless symmetric tensor Q . The degree of order of the liquid crystal could be expressed as $S^2 = \text{Tr}(Q^2)$. Liquid crystal was assumed to be interacting with an electrostatic field applied across the cavity. The equilibrium configuration of Q was found by calculating the minimum of a Landau-de Gennes free energy. The director field profile was then calculated using the Q tensor representation¹⁰ which allows the director field and reorientation to take place in three dimensions. The director field is resolved by finding the minimum free energy for each point on the grid, balancing the surface anchoring forces, the intrinsic elastic forces and the electric field forces on the molecules.

The non-coupled electric field profile in the cavity was derived directly from Maxwell's equations, representing the electric displacement \mathbf{D} in terms of the tensor order parameter. This profile depended only on the ratio of modulation period to cell thickness, L_x/L_z . The resulting electric field strength through the cavity is shown in figure 2. It can clearly be seen that for grating spacing much larger than cell thickness, the electric field penetrates relatively deep into the liquid crystal bulk the cell and the dark regions experience much lower field strength. For grating spacing less than cell thickness, the electric field variation penetrates only a short distance into the cell. These numerical results support experimental evidence of declining diffraction efficiencies and two-beam coupling gain for small grating spacings.

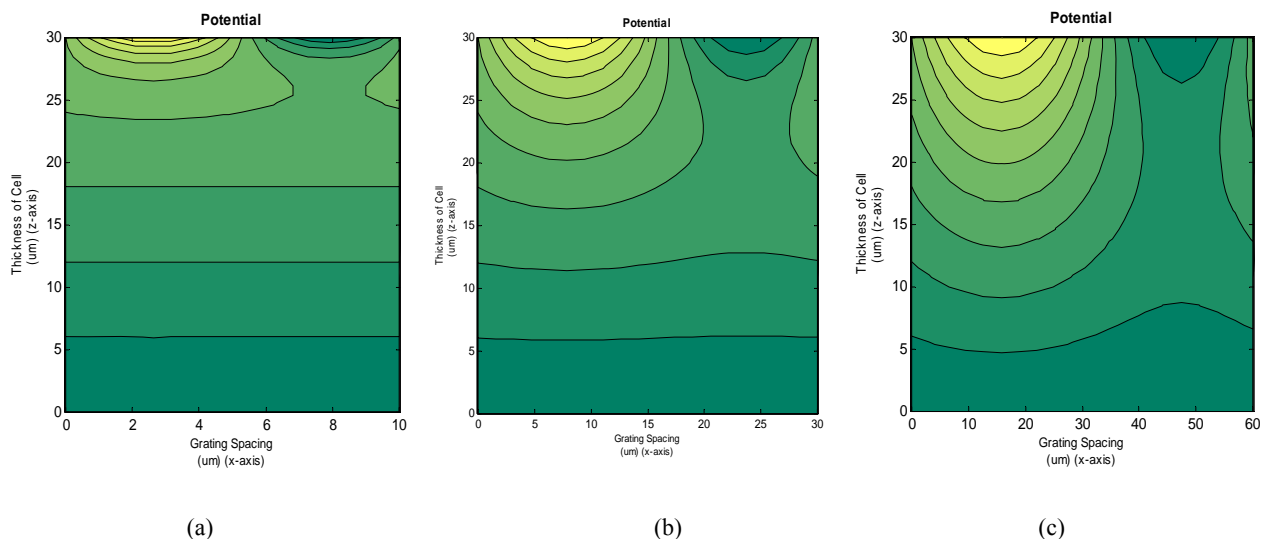


Figure 3 – Electric Field simulations as a function of grating period (a) 10 μm ; (b) 30 μm ; (c) 60 μm

For a relatively small grating spacing of 10 μm (figure 3a), only the part of liquid crystal close to the PVK covered substrate should experience modulated electric field and undergo reorientation. However, in this case elastic forces and surface anchoring can significantly reduce the effective change in alignment. For larger grating spacings of 30 or 60 μm (figure 3b and c), the electric field can reach the middle of the cell and therefore more high contrast reorientation gratings can build up.

4. EXPERIMENTAL RESULTS

In order to investigate in more detail charge transport and the presence of surface charge layers, we studied conductivity and capacitance of cells with PVK and PI layers under electric field and light illumination. AC field is universally used to achieve reorientation in liquid crystal devices and can prevent, for example, image sticking. However, it is the DC field that is required, in most cases, to observe photorefractive effect in liquid crystals and polymers. Hence, more detailed understanding of a liquid crystal response to a DC field is necessary.

In our measurements we used automatic precision bridge that is capable to measure conductivity and capacitance for different values of an external DC bias. The bridge also uses a low voltage AC field. It is typically 0.5V at 1 kHz, which is well below the usual Fredericksz transition. This small AC component was, strictly speaking, absent in the original two-beam coupling experiments, but should not significantly alter capacitance of the whole system.

Measurements were carried out under two conditions – first, without illumination and keeping the ambient light to the minimum and secondly, under uniform illumination with light. Generally, a sudden change in capacitance is expected at some value of a DC field. Due to dielectric anisotropy of liquid crystals, reorientation of liquid crystals leads to changes in capacitance. When an optical Fredericksz transition takes place, the reorientation of the liquid crystal director in the bulk from planar to homeotropic, capacitance can undergo a sudden change.

Figure 4a presents a typical example of measured capacitance in a cell with PVK:C₆₀ layer when illuminated by light. The threshold of reorientation can be observed at approximately 24 V. Figure 4b presents changes in capacitance with DC field in this type of cell without light illumination. When the cell was not illuminated, no threshold of reorientation was observed, indicating strong screening of the liquid crystal bulk from an external DC field. However, at around 55 V, capacitance started to increase, indicating the onset of reorientation. The comparison of figures 4a and 4b demonstrates how the threshold of reorientation can be reduced from approximately 55 V to 25 V by illuminating a PVK:C₆₀ and E7

liquid crystal cell with visible light. The considerable shift of Fredericksz transition (increase of cell capacitance) to lower DC field upon cell illumination can be attributed to anihilation of the surface charge layers that had prevented reorientation of liquid crystal director.

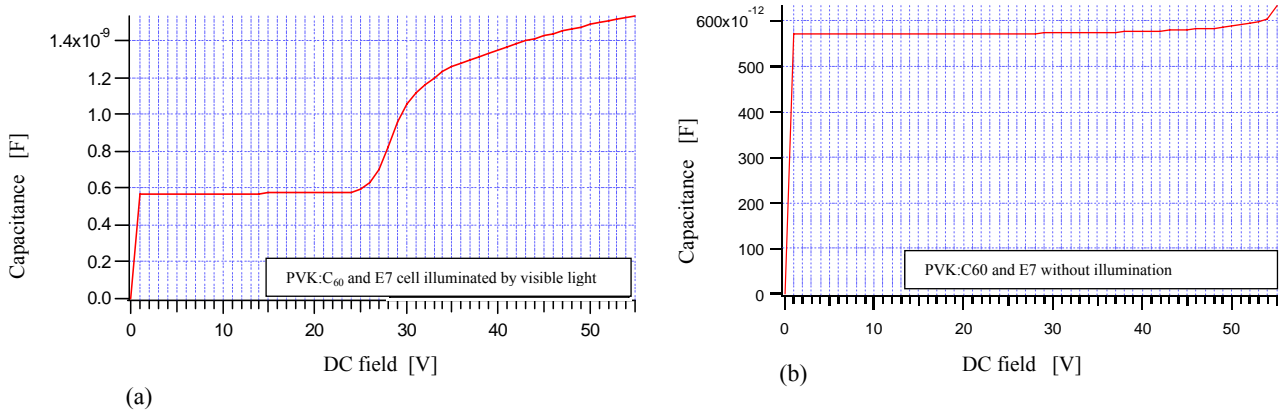


Figure 4 Change of capacitance for increasing DC field in PVK:C60 and E7 with and without illumination by visible light

The process of screening layers build up and the possibility of their selective discharging is not unique to PVK:C60 and E7 liquid crystal cells. Other pure (undoped) nematic liquid crystals tested, such as 5CB, Merck 18523 or LC1294, showed similar response. Moreover, other polymer layers were considered. For example, undoped PVK is photoconductive in the UV and as figures 5a and 5b show, the threshold of reorientation reduces on UV illumination.

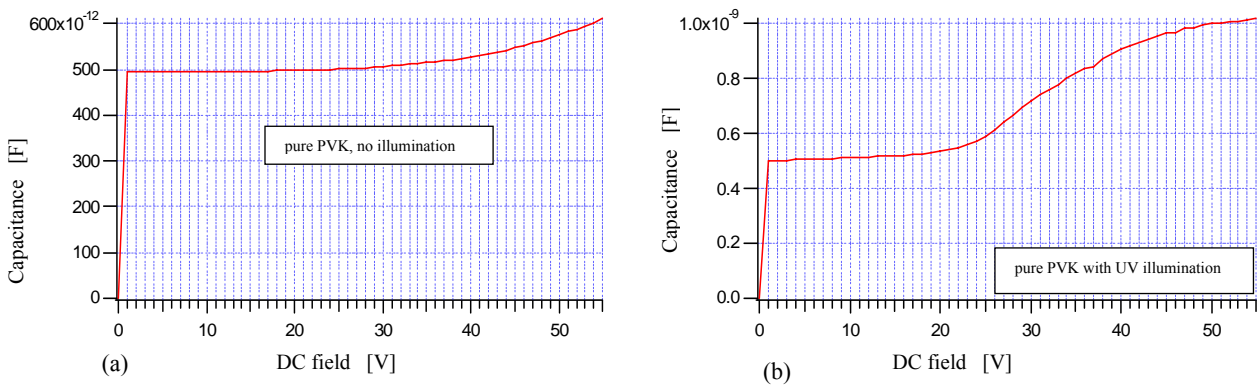


Figure 5 Cell with liquid crystal E7 and pure PVK. The dependence of capacitance on applied DC field (a) without UV illumination and (b) with UV beam incident on the cell.

The evidence for surface screening layers can also be found in other non-photoconductive polymers. We compared the dependence of capacitance on voltage in cells with standard polyimide layers. In one type of cell the polyimide layer was made slightly thicker, namely 300 nm versus standard 100 nm thickness. Figure 6 presents how different reorientation process was in the two types of cells in the absence of illuminating beam.

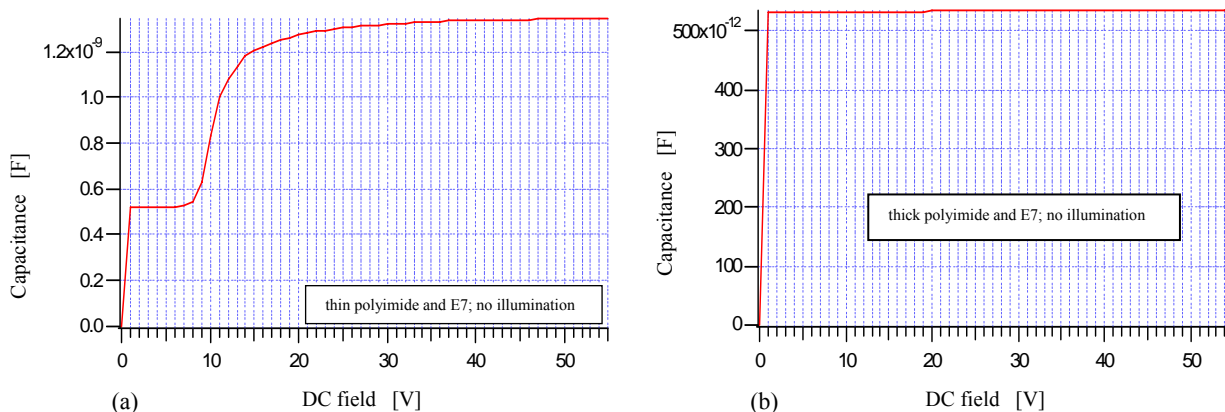


Figure 6 Cells with liquid crystal E7 and thin, 100 nm polyimide covered substrates (a) and thicker, 300 nm polyimide covered substrates (b). Capacitance is measured with increasing DC field and without illumination.

Figure 6a presents the case of a standard cell with 100 nm thick polyimide on both substrates and liquid crystal E7. As expected, even without illumination, there is a threshold of reorientation at approximately 6V, as detected by the changes in capacitance with an increasing DC field. For a cell with 300 nm thick polyimide (figure 6b), there was no evidence of reorientation even at a DC field over 55 V. Clearly the thickness of an aligning polymer can play an important role in determining the orientation of the liquid crystal bulk.

4. CONCLUSIONS

In conclusion, we showed the characteristic features and dependence of reorientation of liquid crystal cells in cells with different polymer alignment layers. Undoped PVK, PVK doped with fullerene (C_{60}) as well as polyimide layers with different thicknesses were investigated. The capacitance measured for increasing DC field confirmed the presence of screening layers, which proved to be very strong not only for the case of PVK, but also for thicker polyimide layers. Surface screening layers could be discharged by light illumination from either UV (for pure PVK) or visible (PVK:C60) range of spectrum. Electric field and director distributions inside a liquid crystal cell show different penetration of field into the liquid crystal bulk, depending on the modulation of surface conductivity and its spacing. Light induced surface effects we investigate are clearly present in different aligning layers-liquid crystal systems, including standard polymer coated substrates. Efficient build-up and discharge of surface charge screening layers, spatially modulated due to the photoconductivity of polymers, could be particularly useful for applications in light amplification with two-beam coupling process or in spatial modulators.

5. ACKNOWLEDGMENTS

We would like to thank R. W. Eason and I.C. Khoo for helpful discussions and advice regarding this work. We acknowledge the financial support of the Engineering and Physical Sciences Research Council (EPSRC) under grant number GR/R27235.

5. REFERENCES

-
- ¹ I.C.Khoo, B.D.Guenther, M.V.Wood, P.Chen, Min-Yi Shih, *Opt. Lett.* **22**, 1229, 1997.
 - ² S. Bartkiewicz, K. Matczyszyn, A. Miniewicz, F. Kajzar, *Opt. Comm.* **187**, 257, 2001.
 - ³ G. P. Wiederrecht, B. A. Yoon, M. R. Wasilewski, *Science* **270**, 1794, 1995.
 - ⁴ H. Ono, T. Kawamura, N. M. Frias, K. Kitamura, N. Kawatsuki, H. Norisada, *Appl. Phys. Lett.* **75**, 3632, 1999.
 - ⁵ W.E. Moerner, et al. *Annu. Rev. Mater. Sci.* **27**, 585-623, 1997.
 - ⁶ D.P. West , M.D. Rahn , C. Im , H. Bassler, *Chem. Phys. Lett.* **326**, 407, 2000.
 - ⁷ M. Kaczmarek, A. Dyadyusha, S. Slussarenko, I. C. Khoo, *J. Appl. Phys.* **96**, 2616 (2004).
 - ⁸ J. Zhang, K. D. Singer, *Appl. Phys. Lett.* **72**, 2948 (1998)
 - ⁹ P. Pagliusi, G. Cipparrone, *J. Appl. Phys.* **93**, 9116 (2003)
 - ¹⁰ A.Sonnet, A.Kilian, and S.Hess, *Phys. Rev. E*, **52** 718 (1995).

Surface charge screening and boundary conditions for high two-beam coupling gain in pure liquid crystals

A. Dyadyusha, M. Kaczmarek, G. Gilchrist, G. D'Alessandro*, J. Parka#, R. Dabrowski#

School of Physics and Astronomy, University of Southampton, Southampton SO17 1BJ, UK

*School of Mathematics, University of Southampton, Southampton SO17 1BJ, UK

#Institute of Technical Physics, MUT University, Warsaw, Poland

ABSTRACT

We report on asymmetric two-beam coupling and the ways of controlling it in liquid crystals cells with photoconducting polymer layers. The cells had one of the substrates covered with a photoconductive polymer layer, namely PVK, photosensitised with C_{60} to respond to visible light. Efficient gain was measured in 30 μm thick cells with two incident beams having the same intensity. We present a model of two-beam coupling gain based on the build-up and discharge of surface charge screening layers, spatially modulated due to the photoconductivity of doped PVK. The simulation of electric field distribution inside a liquid crystal cell for different two-beam coupling grating spacing showed different penetration of field into the liquid crystal bulk. The characteristics of dynamics, magnitude of two-beam coupling and the efficiency of diffraction were determined for different values of applied DC field, cell configuration and liquid crystals. We found that the direction of energy flow was determined just by the cell tilt and not by the DC field bias.

Keywords: liquid crystals, photoconductive polymer, surface-charge field, two-beam coupling

1. INTRODUCTION

Liquid crystal-polymer interface and surface effects can play a significant effect on the optical characteristics of a whole liquid crystal cell. Diffraction efficiency and two-beam coupling gain are the two values often used to characterise optical and photorefractive properties of a material. Photorefractivity in liquid crystals' can be particularly pronounced when they were doped with dyes or with, for example, C_{60} ¹. Another method for observing photorefractive effect relied on combining² liquid crystals with photoconductive layers³. In particular, *poly(N-vinyl carbazole)* (PVK) polymer, doped with photosensitiser trinitrofluorene (TNF) proved very effective for measuring high coupling coefficients⁴. PVK is a well-known photorefractive polymer. Sensitizers, such as C_{60} or TNF, were used as a dopant of PVK in order to increase its sensitivity to the visible range of spectrum. Other options of adding dopants included systems with liquid crystal E7 doped with C_{60} and PVK left undoped⁵.

Two-beam coupling experiments in liquid crystal cells typically operate in the Raman-Nath (thin) grating regime and as a result several diffraction orders of the beams can be present. One of the experimental challenges is, therefore, to ensure the correct measurement of gain by carefully separating effects originating from beam coupling and diffraction⁶. Monitoring of both pump and probe beam intensities with and without the other beam present is essential⁷ to estimate the value of net exchange of energy between two beams, as well as losses and scattering.

Two-beam coupling can be both induced and controlled by light and electric field, as well as by cell and experimental geometry. Modulation of liquid crystal director orientation is responsible for two-beam coupling and in order to see an asymmetric energy exchange, the modulation of reorientation has to be non-local versus the incident light intensity patterns. It was suggested that space-charge field generated in PVK was the main mechanism responsible for this

process^{3,5,8}. However, liquid crystal reorientation can also be strongly driven by surface effects and fields that develop on liquid crystal-polymer interface, such as electric field, electric charge modulation or anchoring.

In this paper we present results two-beam coupling gain and of its dependence on applied DC field, its polarity and the experimental geometry. Moreover, the influence of liquid crystal director alignment as well as light intensity were also studied in detail to establish the role of PVK and surface charge screening in creating a high contrast reorientation grating in liquid crystals.

2. EXPERIMENTAL ARRANGEMENT AND MATERIALS

2.1 Liquid crystal-photoconductive polymer cells

Cells prepared for this experiment had a conventional design with two parallel, ITO covered, glass substrates with 30 μ m thick gap between them filled with liquid crystal. The two substrates of each cell had different polymer layers. The first substrate (onto which laser beams were incident) was covered with PVK:C₆₀ layer. This layer played a double role. It is an alignment layer and, at the same time, a photoconductor responsible for efficient photorefractive properties of the whole system. C₆₀ and PVK were separately dissolved in chlorobenzene. Doping of PVK with C₆₀ was achieved by adding a saturated concentration of C₆₀ solution to the PVK solution. Calculated concentration of C₆₀ in dry PVK layer was approximately 14.9% by weight. Polymer was spincoated onto clean ITO covered glass, dried at high temperature to form a thin, 0.1 μ m, layer. It was then unidirectionally rubbed to promote uniform planar liquid crystal alignment.

The second substrate was covered with standard polyimide (PI) as an alignment layer. A cell was assembled with rubbing directions of opposite substrates being at right angles. This was essential to get a uniform, planar structure in the whole cell due to different alignment properties of PI and PVK. PI promotes an easy axis of liquid crystal alignment along a rubbing direction with small pretilt angle. However, PVK promotes an easy axis orthogonal to the rubbing direction with a zero pretilt angle. Cells prepared in this way could then fill with different liquid crystals. We used liquid crystal E7 because of its temperature stability, as well as significant optical anisotropy ($\Delta n=0.22$). Moreover, novel liquid crystals with large optical anisotropy ($\Delta n=0.45$) were also used.

As expected, PVK significantly modified the operation and threshold for reorientation of the cells. Pure, undoped PVK is an insulator in the visible with very low conductivity. However, it becomes photoconductive when illuminated by UV light⁹. PVK is a charge-transporting polymer with good hole conductivity and high concentration of active charge transport sites (carbazole groups)¹⁰. Its photosensitivity¹¹ can be improved further by doping with sensitizers. Doping with trinitrofluorene (TNF) or C₆₀ shifts the absorption of PVK into the visible band via the formation of a charge transfer states.

2.2 Experimental set-up

A schematic diagram of the experimental configuration for measuring two-beam coupling gain is presented on figure 1. A cell, mounted on a rotation stage, could be precisely turned around the vertical axis (perpendicular to the plane containing the incident beams) at the point of intersection of the incident beams. In this way the transmitted intensity dependence on the angle of incidence, which we call a cell tilt, could be measured. The cell was set up so its photosensitive substrate (with PVK:C₆₀) was the one onto which light was incident first ("input substrate").

Data acquisition software was used to control the set-up and carry out accurate and easily repeatable measurements. For example, it was essential for studies of two-beam coupling dynamics to have a precise control of electric shutters, that blocked or unblocked the beams, as well as of application of electric field and cell rotation. Two-beam coupling gain dependence on several experimental parameters, such as DC field magnitude or the angle of cell tilt, was measured.

The two incident beams ($\lambda=543$ nm) were p-polarized, in the plane of incidence. Their intensities were approximately the same and equal 400 μ W/cm², in order to keep their incident intensity ratio $m=1$. The interference pattern incident on

a liquid crystal cell had a fringe spacing of 15 μm . The intensities of transmitted beams and of first order diffracted beams were measured on photodiodes and data stored on a computer.

In our earlier work¹² we established the optimum conditions for cell rotation, the so called cell tilt, which is the angle between the normal to the cell surface and the bisector of the angle between incident beams, to observe high gain. The optimum value of the cell tilt was found to be approximately equal to 30° . Hence, for the experiments presented in this paper we kept the cell tilt constant and equal to 30° . It is worth noting that this angle is equal to the angle between grating vector of the intensity grating (produced by interference between two beams) and the photoinduced refractive index grating vector, which is parallel to the surface of cell substrates.

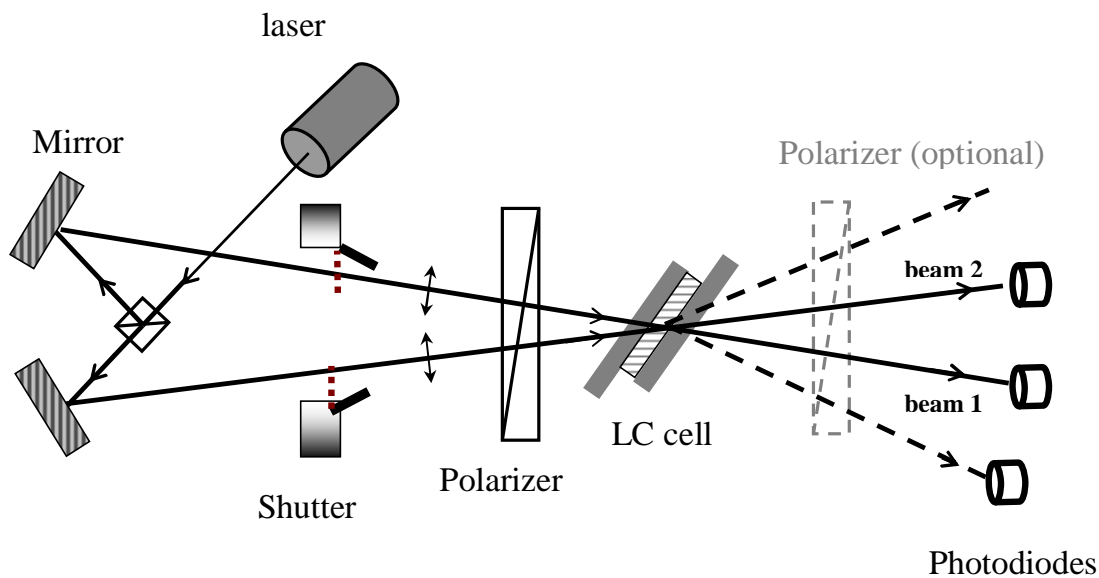


Figure 1 Experimental set-up for measuring two-beam coupling

The data acquisition software was programmed to detect and measure of two-beam coupling in several steps in which incident beams were either blocked or unblocked⁷ and the intensity of transmitted beams were measured. In step one the shutters were opened to let both beams through. In the second step, just beam 1 was present, followed by a step where both beams were again present. In the next stage, the shutter for beam 1 was closed and for beam 2 opened. Finally, both beams were let through and then both blocked. The described sequence of steps was repeated for different values of voltage of DC field, increasing from zero to 30 V. For each value of DC field, data from this experimental routine were plotted, as graph on figure 5. Values for intensities of beams could then be extracted from such graphs and plotted as a function of DC field (figures 2 to 4.) The complete experimental procedure allowed us to measure gain and, at the same time, monitor the total change in beam intensities. In this way we were able to correctly identify and distinguish the real gain, as well as loss, from scattering and diffraction. For example, gain could, nominally be very high, but at the same time, the total losses of the system could approach 100%.

3. RESULTS AND DISCUSSION

Liquid crystal cells with PVK:C₆₀ layers have certain characteristic features of response when an external DC field is applied. The reorientation of liquid crystal molecules is the result of photo-modulated potential on the liquid crystal-polymer interface. The details of the mechanism responsible for this modulated potential were described in our earlier

work¹². Surface charge field builds up from the combination of an external DC field and photoconductivity of PVK:C₆₀ layer. An external DC is essential for the formation of screening charge layer near the PVK:C₆₀ covered substrate, which in turn, reduces the field across liquid crystal bulk to the level below Freedericksz transition threshold. As a result, Freedericksz transition is not observed unless the cell is illuminated by, for example, light interference pattern. In light fringes, the surface charge layer is discharged and in dark fringes it remains. Hence, the interference pattern can create regions where liquid crystal molecules are reoriented next to regions of unperturbed, original orientation of liquid crystals. It is worth to underline that according to our model, the induced refractive index grating is local relative to intensity grating. However, due to the complex structure and deformations involved in reorientation, the induced space charge field has two-dimensional dependence. While it is localised near the PVK:C₆₀ substrate surface, it is also coupled with the director field and dependent on the number of parameters such as an external DC field and light intensity. Two-beam coupling gain was only observed when DC field was applied. Finally, we assumed that the second substrate was not photoconductive or photosensitive and there was no photoinduced modulation of potential near that surface.

3.1 Two-beam coupling and DC field polarity

In the first part of experimental work, the dependence of two-beam coupling gain on the DC field polarity was investigated. When photorefractive two-beam coupling gain was studied in, for example, dye doped liquid crystals or in fact in photorefractive solid state crystal, it was demonstrated that changing the DC field polarity caused the reversal of energy flow (gain). This type of dependence could be explained via standard photorefractive theory that relies on the generation of space charge field via photoionization of charges, their drift and diffusion followed by trapping in non-illuminated areas.

However, in cells with PVK:C₆₀ the gain reversal effect with changing DC polarity was not observed. Figure 2 and Figure 3 present the results on transmitted light intensities for positive and negative bias, respectively, applied to the input substrate. The cell was arranged that its director was in the same plane as the polarization of the two incident beams. On figures 2 and 3, there are four curves. Beam 2₁ and Beam 1₂ demonstrate the presence and magnitude of two-beam coupling effect. Beam 2₁ curve show the dependence of amplified probe on the applied DC field, while Beam 1₂ indicates the depleted pump. Beam 2₁ could be regarded as a probe beam and beam 1₂ as a pump beam. For comparison, beam 2 intensity without beam 1 present (Beam 2 curve) and beam 1 intensity without beam 2 present (Beam 1 curve) were also plotted as a function of DC field.

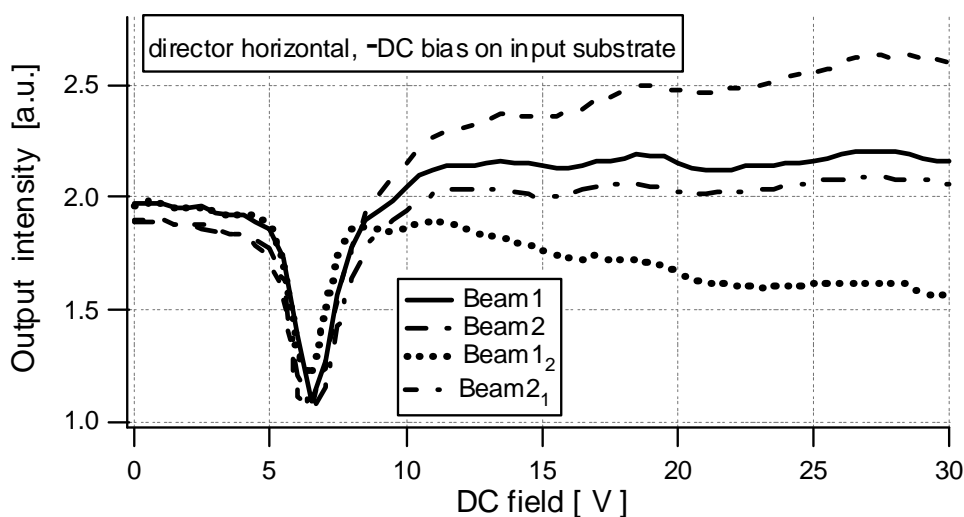


Figure 2 Two-beam coupling with negative bias on the input substrate as a function of applied DC field with horizontal director.

Keeping the director horizontal, the bias on the input substrate was changed from negative to positive and two-beam coupling dependence on the magnitude of applied DC field was measured.

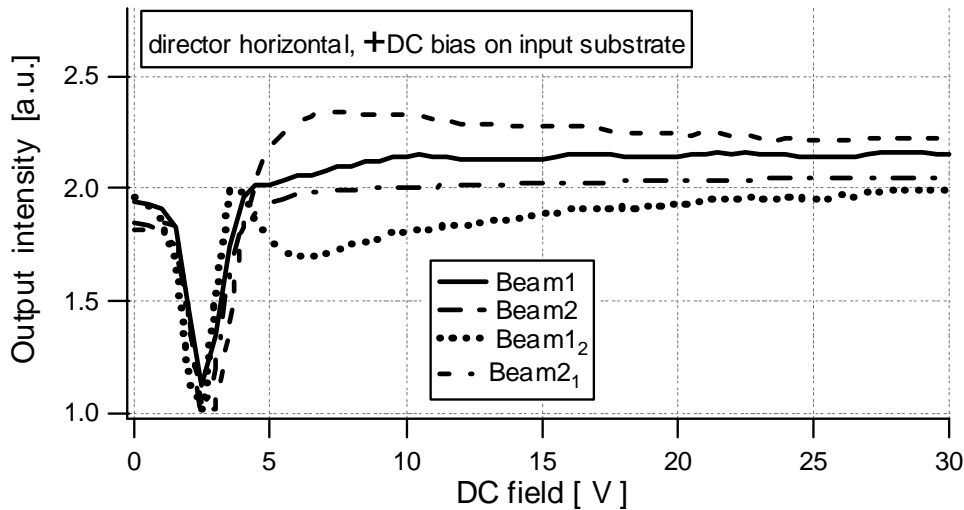


Figure 3 Two-beam coupling with positive bias on the input substrate as a function of applied DC field and horizontal director.

As figures 2 and 3 demonstrate that there was no gain reversal with changing DC field polarity. However, there were some difference in amplified probe beam (and depleted pump) intensity dependence for the two cases of applied DC field. First of all, higher amplification was observed for the negative bias case. Secondly, the optimum voltage for high gain was different. For negative polarity, the highest gain was measured for voltages above 25 V, while for the positive polarity the optimum voltage was between 5 -10 V.

The lack of gain reversal and the different features of two-beam coupling in two cases of DC polarity are consistent with our model of screening layers formation and their selective discharge. Screening charge layers can have different properties depending on the type of carriers that accumulate at the liquid crystal-polymer interface as a result of negative (or positive) bias of DC field. For example, with PVK having high hole mobility, but poor electron conduction, it can be expected that for negative bias the process of discharging and charges recombination is more efficient than for a positive bias. However, irrespective of DC field polarity, screening layers build up and can be discharged. Electric field and, correspondingly, refractive index is modulated near PVK:C₆₀ substrate for either of the polarities, hence the direction of energy flow remains the same.

3.2 Cell rotation and its effect on gain and scattering

Two-beam coupling effect could be observed for different alignment of liquid crystal cells provided the incident beams remained p-polarized. Two possible directions of liquid crystal director were investigated, namely with original (before application of an external electric field or illumination) director being either parallel or orthogonal to the plane of incidence that contained both incident beams. In the former case, the director was parallel to the grating vector of induced refractive index grating, in the later orthogonal to it. As a result, different deformations of the director field were involved in creating induced, reorientational refractive index grating.

Figures 2 presented two-beam coupling results as a function of DC field (negative bias) for the director parallel to the plane of incidence. Figure 4 presents the similar dependence, but for a vertical director.

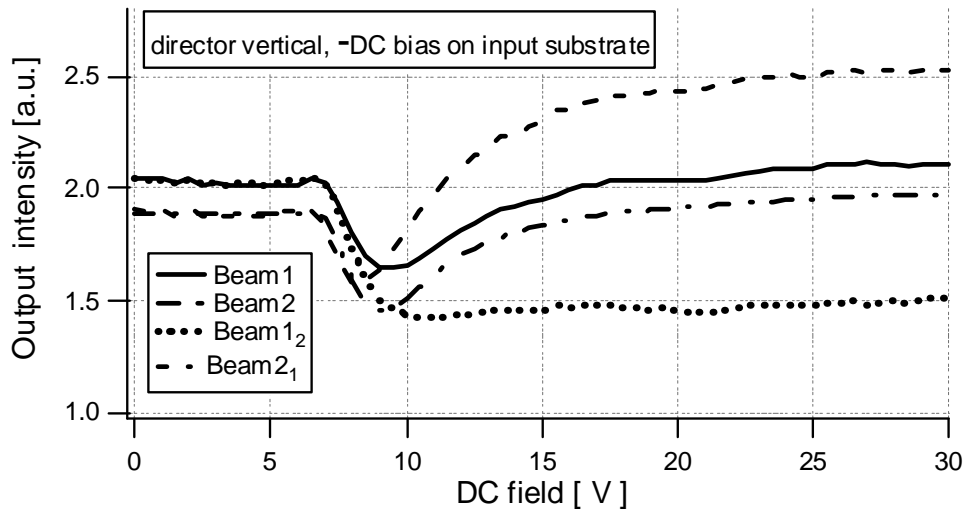


Figure 4 Two-beam coupling with negative bias on the input substrate as a function of applied DC field for the director orthogonal to the plane of incidence.

As in the case of horizontal director, with vertical director, changing the DC bias to positive on the input substrate did not change the direction of energy transfer.

While the maximum value of gain was approximately the same for both cases of the director's position, the gain dynamics, the amount of scattering and the evolution of pump and probe beam with increased voltage were different for the two positions of the cell. Since the two initial directions of the director were orthogonal to each other, the corresponding thresholds for reorientation were different as was the elastic energy, related to the reorientation of liquid crystal director, and its coupling with electric field potential.

3.3 Dynamics of two-beam coupling

The evolution of amplified and depleted beams was also monitored as the beams reached steady-state. Figure 5 presents a typical example of each beam's intensity as the other beam was turned on and off.

The time evolution of energy transfer was measured by recording the intensities of both beams transmitted, pump and probe beams, through the sample. In the first stage, both beams were opened, and after their intensities reached equilibrium, the first beam was blocked with a shutter and then opened again. The same procedure was applied to the other beam. Such monitoring of grating formation and decay was carried out for increasing DC field, in 0.5 V steps. The case presented in figure 5 shows an example of measurement carried out for the DC field of 20V.

The details of the dynamics of beam amplification and depletion could be investigated in detail. When both beams are switched on, the initial intensity of the amplified beam increased rapidly and then decayed to a steady-state level. Clearly, some competition from other effects such as scattering or diffraction contributes to the decrease of the initial gain.

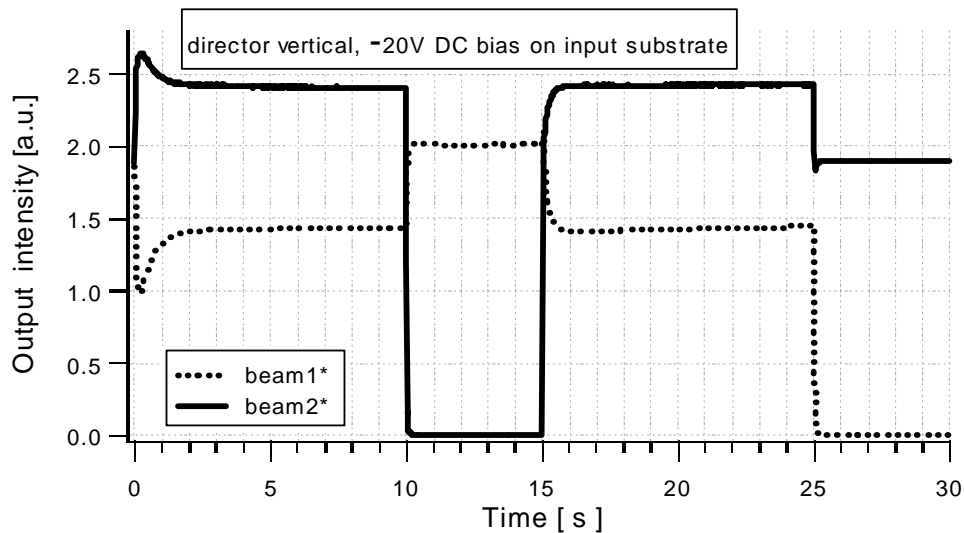


Figure 5 Dynamics of two-beam coupling process with both or one beam incident on a cell

3.4 Photorefractive effect in liquid crystal-polymer structures

The qualitative description and model we developed for two-beam coupling in liquid crystal-photoconductive polymer systems and their parameters is the first step in gaining a better understanding of photorefractive and photoconductive phenomena taking place at polymer-liquid crystal interfaces. Two-beam coupling in various liquid crystal-polymer systems^{5,13,14} was usually explained via orientational gratings that form as a result of spatially modulated electric field inside a liquid crystal cell. The profile and strength of such electric field modulation was a result of an externally applied (uniform) electric field and, specific for a particular dopant or polymer, light-induced processes. We observed that in the case of PVK-liquid crystal systems, large photoconductivity and low dark conductivity of PVK played far more substantial role in two-beam coupling process than photorefractive properties of PVK.

Further modeling of electric field and director profile is needed not only to gain better understanding of surface effects in liquid crystal-polymer interfaces, but also to optimize experimental parameters, such as cell thickness or grating spacing.

4. CONCLUSIONS

In conclusion, we showed the characteristic features and dynamics of two-beam coupling process in liquid crystal cells with alignment layers made of PVK doped with fullerene (C_{60}) as a photosensitizer. Two different liquid crystal director orientations were investigated. In a cell oriented so its director was vertical to the plane of incidence, two-beam coupling gain was higher and less loss was observed than in a cell with a director in the plane of incidence. The dynamics of amplified and depleted beams was monitored and measured in several steps in order to deduce precisely the value of gain and scattering. High transient gain was observed when both beams were switched on, followed by the decay of amplified beam to a steady-state level. The polarity of DC field changed the dependence of amplified beam on voltage, but did not cause gain reversal irrespective of the orientation of the liquid crystal director. Negative bias on the input interface yielded higher gain, but this optimum gain required relatively high voltage (30 V).

5. ACKNOWLEDGMENTS

We would like to thank R. W. Eason and I.C. Khoo for helpful discussions and advice regarding this work. We acknowledge the financial support of the Engineering and Physical Sciences Research Council (EPSRC) under grant number GR/R27235.

5. REFERENCES

-
- ¹ I.C.Khoo, B.D.Guenther, M.V.Wood, P.Chen, Min-Yi Shih, *Opt. Lett.* **22**, 1229, 1997.
 - ² G. P. Wiederrecht, *Annu. Rev. Mater. Res.* **31**, 139, 2001.
 - ³ S.Bartkiewicz, A.Miniewicz, F.Kajzar, M.Zagorska, *Mol. Cryst. Liq. Cryst.* **322**, 9, 1998.
 - ⁴ S. Bartkiewicz, K. Matczyszyn, A. Miniewicz, F. Kajzar, *Opt. Comm.* **187**, 257, 2001.
 - ⁵ J. Mun, Ch-S. Yoon, H-W. Kim, S-A. Choi, J-D. Kim, *Appl. Phys. Lett.* **79**, 1933, 2001.
 - ⁶ G. P. Wiederrecht, B. A. Yoon, M. R. Wasilewski, *Science* **270**, 1794, 1995.
 - ⁷ J. E. Hall, D. A. Higgins, *Rev. Scient. Meth.* **73**, 2103, 2002.
 - ⁸ H. Ono, T. Kawamura, N. M. Frias, K. Kitamura, N. Kawatsuki, H. Norisada, *Appl. Phys. Lett.* **75**, 3632, 1999.
 - ⁹ W.E. Moerner, et al. *Annu. Rev. Mater. Sci.* **27**, 585-623, 1997.
 - ¹⁰ W.E. Moerner et al., *Chem. Phys. Lett.* **291**, 553-561, 1998.
 - ¹¹ D.P. West, M.D. Rahn, C. Im, H. Bassler, *Chem. Phys. Lett.* **326**, 407, 2000.
 - ¹² M. Kaczmarek, A. Dyadyusha, S. Slussarenko, I. C. Khoo, *J. Appl. Phys.* **96**, 2616 (2004).
 - ¹³ J. Zhang, K. D. Singer, *Appl. Phys. Lett.* **72**, 2948 (1998)
 - ¹⁴ P. Pagliusi, G. Cipparrone, *J. Appl. Phys.* **93**, 9116 (2003)